Measurement of the lifetimes of excited states in neutron-rich Ce isotopes

Messung der Lebensdauern von angeregten Zuständen in neutronenreichen Cerisotopen

Vom Fachbereich Physik der Technischen Universität Darmstadt zur Erlangung des Grades eines Doktors der Naturwissenschaften (Dr. rer. nat.) genehmigte Dissertation von Guillermo Fernández Martínez, M. Sc. aus Logroño (Spanien)

Tag der Einreichung: 10. April 2018, Tag der Prüfung: 7. Mai 2018

2018 — Darmstadt — D 17

1. Gutachten: Prof. Dr. Thorsten Kröll
2. Gutachten: Prof. Dr. Joachim Enders

TECHNISCHE UNIVERSITÄT DARMSTADT

Fachbereich Physik
Institut für Kernphysik
AG Kröll

Bundesministerium für Bildung und Forschung

HIC for FAIR
Helmholtz International Center

GSI

Argonne NATIONAL LABORATORY

Measurement of the lifetimes of excited states in neutron-rich Ce isotopes
Messung der Lebensdauern von angeregten Zuständen in neutronenreichen Cerisotopen

Genehmigte Dissertation von Guillermo Fernández Martínez, M. Sc. aus Logroño (Spanien)

1. Gutachten: Prof. Dr. Thorsten Kröll
2. Gutachten: Prof. Dr. Joachim Enders

Tag der Einreichung: 10. April 2018
Tag der Prüfung: 7. Mai 2018

2018 — Darmstadt — D 17

Bitte zitieren Sie dieses Dokument als:
URN: urn:nbn:de:tuda-tuprints-78184
URL: http://tuprints.ulb.tu-darmstadt.de/7818

Dieses Dokument wird bereitgestellt von tuprints,
E-Publishing-Service der TU Darmstadt
http://tuprints.ulb.tu-darmstadt.de
tuprints@ulb.tu-darmstadt.de

Die Veröffentlichung steht unter folgender Creative Commons Lizenz:
Namensnennung – Keine kommerzielle Nutzung – Keine Bearbeitung 4.0 International
http://creativecommons.org/licenses/by-nc-nd/4.0

Erklärung zur Dissertation

Hiermit versichere ich, die vorliegende Dissertation ohne Hilfe Dritter nur mit den angegebenen Quellen und Hilfsmitteln angefertigt zu haben. Alle Stellen, die aus Quellen entnommen wurden, sind als solche kenntlich gemacht. Diese Arbeit hat in gleicher oder ähnlicher Form noch keiner Prüfungsbehörde vorgelegen.

Darmstadt, den 10. April 2018

(Guillermo Fernández Martínez)

Zusammenfassung

Die neutronenreichen Cerisotope liegen auf der Nuklidkarte einige Neutronen und Protonen oberhalb des doppelt magischen ^{132}Sn, in einer Region, in welcher eine Vielfalt an Deformationsphänomenen auftritt. Unter diesen stechen die Entwicklung der Quadrupolkollektivität beim Entfernen vom Schalenabschluss und die Oktupoldeformation in der Nähe von $Z = 56$ und $N = 88$ heraus.

Das Ziel dieser Arbeit ist daher die Untersuchung der strukturellen Entwicklung von neutronenreichen Cerisotopen mittels der Bestimmung der reduzierten Übergangswahrscheinlichkeiten ihrer niedrig liegenden angeregten Zuständen. Diese Werte wurden aus der direkten Messung der Lebensdauern der Zustände bestimmt.

Die experimentelle Kampagne wurde am Argonne National Laboratory durchgeführt, wo eine große Anzahl verschiedener Kerne bei der spontanen Spaltung von ^{252}Cf produziert wurde. Um die Selektion der Cerisotope sicherzustellen, wurde eine Hemisphäre des Gammasphere Arrays, welche aus 51 hochauflösenden HPGe Detektoren besteht, verwendet. Zusätzlich erlaubte es die Nutzung der 25 ultraschnellen $LaBr_3$(Ce) Detektoren der NuSTAR-FATIMA Kollaboration die Lebensdauer der angeregten Zustände der ausgewählten Isotope mittels der Generalised Centroid Difference Method zu bestimmen. Die Verwendung eines so großen kombinierten Detektorsystems bestehend aus HPGe und $LaBr_3$(Ce) in einem Fast-Timing Experiment ist beispielslos.

Es wurden mehrere Lebensdauern von niedrigen liegenden angeregten Zuständen der gerade-gerade $^{146-150}$Ce Isotope bestimmt, vier von diesen zum ersten Mal. Der beobachtete Trend der reduzierten Übergangswahrscheinlichkeiten entlang der Isotopenkette zusammen mit der Systematik der Anregungsenergien bestätigt die verstärkte Kollektivität hin zu prolaten Formen. Diese experimentellen Ergebnisse wurden mit neuen theoretischen Rechnungen, welche auf Symmetry Conserving Configuration Mixing und Schalenmodellansätzen beruhen, verglichen. Beide theoretischen Vorhersagen scheinen die experimentellen Resultate gut zu reproduzieren.

Abstract

Neutron-rich cerium isotopes are located in the region of the nuclear chart some neutrons and protons above the doubly-magic ^{132}Sn, where a variety of shape phenomena are expected. Among them, the evolution of the quadrupole collectivity going away from the shell closures, or the octupole deformation in the vicinity of $Z = 56$ and $N = 88$ stand out.

The goal of the present work is, hence, the study of the structural evolution of neutron-rich cerium isotopes, through the knowledge of the reduced transition strengths between their low-lying excited states. These values have been derived from the direct measurement of the lifetimes of excited states.

The fast-timing experimental campaign was carried out at the Argonne National Laboratory, where a large variety of nuclei was produced in the spontaneous fission of ^{252}Cf. In order to ensure the selection of the cerium isotopes of interest, one hemisphere of the Gammasphere array, consisting of 51 high-resolution HPGe detectors, was used. Additionally, 25 ultra-fast $LaBr_3$(Ce) detectors from the NuSTAR-FATIMA collaboration allowed to measure the lifetimes of the excited states of these selected isotopes by means of the Generalised Centroid Difference Method. The use of such a large combined array of HPGe and $LaBr_3$(Ce) detectors is unprecedented in a fast-timing experiment.

Several lifetimes of low-lying excited states in the even-even $^{146-150}$Ce isotopes have been obtained, four of them for the first time. The observed trend of the reduced transition strengths along the isotopic chain, together with the systematics of the excitation energies confirm the increasing collectivity towards more prolate shapes. These experimental results have been compared to new theoretical calculations obtained within the Symmetry Conserving Configuration Mixing and Shell Model approaches. Both theoretical predictions seem to properly reproduce the experimental results.

Contents

1 Introduction

The ultimate goal of nuclear physics is the understanding of the constituents of nuclei, as many-body quantum systems, and of the fundamental interactions between these constituents. In spite of the variety of nuclear models that currently exist, none of them is able to explain the behaviour and properties of all nuclei from first principles [Fra17]. In this context, the role of spectroscopy is crucial, since it provides experimental information on nuclear properties that do not depend on the choice of a particular nuclear model. These properties are called *observables*. For instance, the measurement (or *observation*) of the radiation energy in order to determine excitation energies has led the development of nuclear – and atomic – structure physics nearly since its origin. Other observable, of great relevance for this work, is the lifetime of excited states, whose direct measurement allows to obtain a model-independent value for the matrix element of the transition between nuclear levels.

Several methods exist to perform direct measurements of lifetimes of excited states of nuclei. Some of them are based on the Doppler effect and allow to access lifetimes in the range from few femtoseconds to tens of nanoseconds [NSS79]. The technique used in this work is, however, the electronic fast timing, that provides access to a more limited range of lifetimes, but introduces less systematical errors. It relies on the accurate determination of the γ-ray detection time difference and it is thus subject to the combination of good timing and energy resolution and high efficiency of the detectors. Historically, plastic or BaF_2 scintillators (with very good timing resolution but very poor energy resolution) or germanium detectors (with very good energy resolution but very poor timing resolution) have been used. This restricted the applicability of the method to either very clean experiments in which the energy resolution was not crucial, or to experiments that aimed for the measurement of long lifetimes. However, the parallel development, in the last few years, of sophisticated electronic fast-timing methods [MGM89; Rég11] and the invention of novel γ-ray detectors with good timing resolution, good efficiency and good energy resolution [Loe+01] made the fast-timing spectroscopy of a large amount of nuclei, in the range from few nanoseconds down to tens of picoseconds, possible. Neutron-rich cerium isotopes are among these nuclei.

^{146}Ce, ^{148}Ce and ^{150}Ce, with $Z = 58$ protons and $N = 88$, 90 and 92 neutrons, respectively, are located in a region of the nuclear chart far away from the doubly-magic ^{132}Sn, as it can be seen in figure 1.1. This favours the appearance of a variety

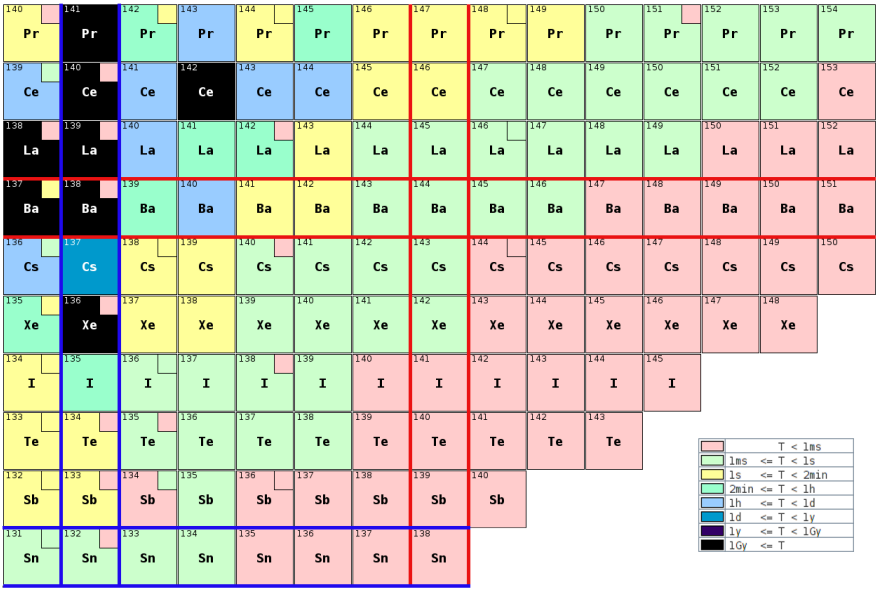

Figure 1.1.: Close view of the nuclear chart, north-east of the doubly-magic ^{132}Sn. Shell closures are marked with blue lines, whereas red lines mark the nuclei with $Z = 56$ or $N = 88$, expected to show strong octupole correlations. Plot made with JANIS4 software [Jan]

of shape phenomena [Lic+17], among which the existence of octupole deformations, that may occur both as vibrations and as permanent deformation [BN96], stands out. Strong octupole correlations appear when the intruder orbitals interact with the normal-parity states with orbital angular momentum that differs by three units [NT92]. This condition is fulfilled by nuclei with proton and neutron numbers near $Z = 34$, 56 and 88 or $N = 34$, 56, 88 and 134. Particularly relevant for the purpose of this work is the vicinity of $Z = 56$ and $N = 88$, where neutron-rich cerium isotopes can be found. Surprisingly, in spite of their fundamental interest, little experimental data exist on their excited states.

The aim of this work is to shed light on the structural evolution of neutron-rich cerium isotopes through the direct measurement of the lifetime of their excited states, and the subsequent derivation of the reduced transition probabilities between them.

Some approaches in nuclear theory, relevant for the interpretation of the results obtained in this work will be explained in chapter 2, as well as the fundamentals of γ decay, crucial in the derivation of reduced transition probabilities from measured lifetimes. In chapter 3, the electronic timing technique will be presented, together with some of the most common methods derived from it, used to extract lifetimes of excited states of nuclei. Special emphasis will be made on the explanation of the Mirror Symmetric Centroid Difference method. The following chapter is devoted to the presentation of the detectors, and the justification of their use in this experiment. Precisely, details on the experiment and data acquisition will be given in chapter 5. This will lead to the explanation of the analysis in chapter 6 and the presentation of results, comparison with new calculations from theory and conclusions in chapter 7.

2 Theoretical background

2.1 Nuclear structure models

2.1.1 Shell model

One of the first theoretical models to describe the structure of nuclei was the shell model (or independent particle model). Its development was motivated by the observation of effects in nuclear physics with a clear analogy to effects in atomic physics that had been successfully explained in terms of atomic orbitals. One of these effects is, for instance, the existence of certain nuclei for which the nucleon separation energy is particularly large, equivalent to the case of the noble gases in atomic physics. The privileged numbers that corresponded to fully-occupied nuclear shells were referred to as *magic* numbers and measured to be 2, 8, 20, 28, 50, 82, 126 and 184.

Shell model is based on the assumption that a nucleon can move independently within an average spherically-symmetric potential generated by the remaining nucleons. Therefore, this potential must fulfil the following conditions:

(i) $\left(\frac{\partial V(r)}{\partial r}\right)|_{r=0} = 0$, since a nucleon close to the center of the nucleus feels no net force from the other nucleons.

(ii) $\left(\frac{\partial V(r)}{\partial r}\right)|_{r<R_0} > 0$, because it is an attractive potential inside the volume of the nucleus (of radius R_0).

Two potentials widely used in quantum mechanics which fulfil these conditions are the infinite well and the harmonic oscillator. However, a more realistic potential would need to include the condition that accounts for the fact that the nuclear forces range is finite, $V(r) \approx 0$, for $r > R_0$. An analytic ansatz whose solutions are between those of the harmonic oscillator and the infinite well, and also fulfils the aforementioned requirements, is the Woods-Saxon potential [WS54]:

$$V_{WS}(r) = -\frac{V_0}{1 + e^{\frac{r-R_0}{a}}}$$

with $R_0 = r_0 A^{1/3}$, $V_0 \approx 50\,\text{MeV}$, $a \approx 0.5\,\text{fm}$ and $r_0 \approx 1.2\,\text{fm}$ [RS80].

Solving the eigenvalue problem

$$\left\{-\frac{\hbar^2}{2m}\Delta + V(\boldsymbol{r})\right\}\phi_i(\boldsymbol{r}) = \epsilon_i \phi_i(\boldsymbol{r}) \tag{2.1}$$

yields the wave functions and energies of each of the single-particle states, ϕ_i. If the Pauli principle is taken into account to fill the energy levels, these states can be characterised by the main quantum number $n = 1, 2, 3...$, the orbital angular momentum $l = 0, 1, ..., n-1$ and the spin $s = 1/2$. The shell structure arises at this point, but it is only capable to reproduce the 2, 8 and 20 magic numbers. It is only after the introduction of two additional terms, the spin-orbit term, proportional to $\boldsymbol{l}\cdot\boldsymbol{s}$, as well as a term proportional to $\boldsymbol{l}^2$ (to account for the overestimation of the energy of the levels with large l), when the full set of observed magic numbers is reproduced [GM49; HJS49]. The total potential is, therefore,

$$V(r) = V_{WS}(r) + C\boldsymbol{l}^2 - D\boldsymbol{l}\cdot\boldsymbol{s} \tag{2.2}$$

Figure 2.1 shows the distribution of levels derived from the solution of 2.1 using the potential in equation 2.2. Each of the levels is tagged with n, the orbital angular momentum l, and the total angular momentum $|l-s| \leq j \leq l+s$. On the right-hand side, in brackets, the total number ofparticles that there are in each of the levels $(2j+1)$ is specified. Additionally, the accumulated number of particles is written in square brackets. The largest energy gaps between levels correspond to gaps between shells.

In general, a full microscopic theory of the nucleus must account for the whole set of nucleons, and must be given by the solution of the many-body Schrödinger equation [RS80]:

$$H\Psi = \left\{\sum_{i=1}^{A}\frac{-\hbar^2}{2m}\Delta_i + \sum_{i<j}^{A} v(\boldsymbol{r}_i, \boldsymbol{r}_j)\right\}\Psi(1,...,A) = E\Psi(1,...,A) \tag{2.3}$$

The many-body hamiltonian in equation 2.3 can be interpreted as the sum of two contributions: on one hand, the interaction with the central potential of the A single particles, given by the sum of their kinetic and potential energies. On the other hand, the residual interaction v, that accounts for the interaction between single particles, which can be neglected within this simple nuclear shell model framework [RS80]. Thus, equation 2.3 can be written as:

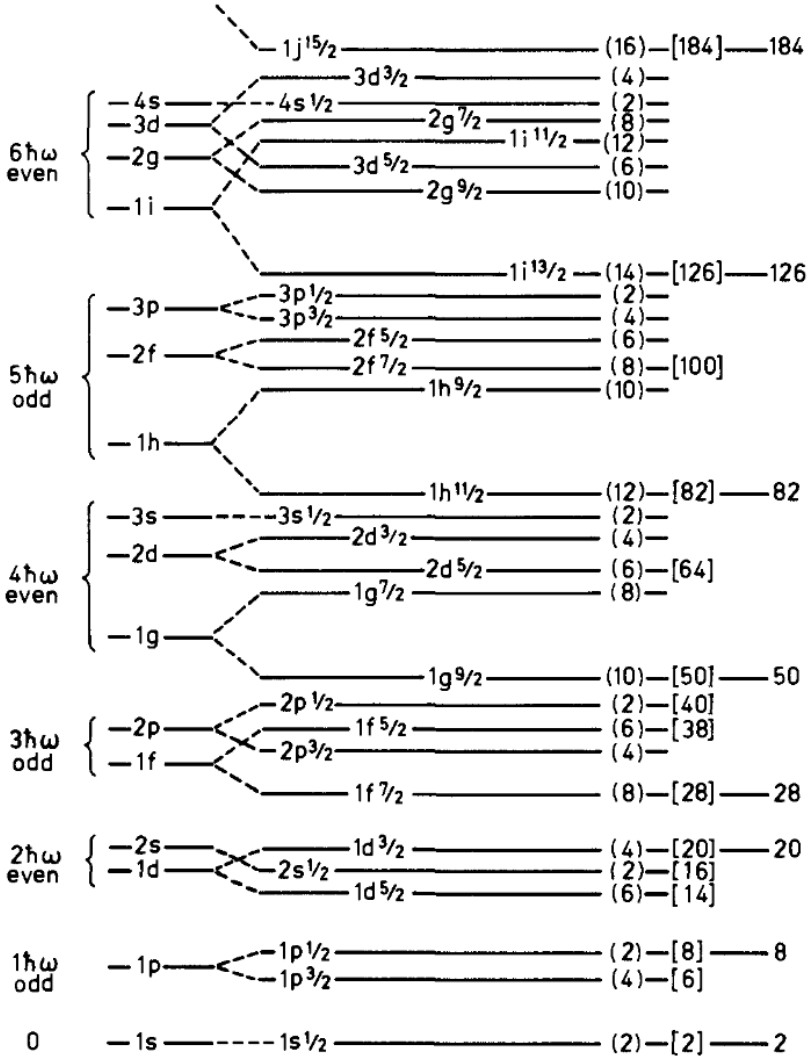

Figure 2.1.: Distribution of energy levels derived from the potential in equation 2.2, that gives rise to the appearance of the magic numbers. Figure taken from [RS80]. Reproduced with permission of Springer in the format Thesis/Dissertation via Copyright Clearance Center.

$$\sum_{i=1}^{A}\left\{-\frac{\hbar^2}{2m}\Delta_i + V(\boldsymbol{r}_i)\right\}\Psi = E\Psi \tag{2.4}$$

whose solutions are eigenfunctions of the single-particle hamiltonian in equation 2.1. More sophisticated shell-model calculations must include the residual interaction in the total hamiltonian that has been neglected here in order to obtain many-body states.

Shell model describes very successfully properties of nuclei in the vicinity of closed shells. However, when the number of nucleons is sufficiently large, nuclear deformations become relevant and the nuclear structure can not be properly described in terms of spherical shell model. In order to overcome this problem, two solutions have been proposed. The first one consists of the description of the nucleons as particles within a deformed central potential, the Nilsson model [Nil55]. The second one is the collective model, explained in section 2.1.2.

2.1.2 Collective model

The collective model has its origin in the liquid drop model, which was the first model to be proposed to explain certain properties of nuclei [RS80]. Although the description is highly phenomenological and must be interpreted with extreme caution, it is able to predict the value of the binding energy per nucleon relatively well. The shape of the surface of the nucleus is described by the parametrisation 2.5.

$$R(\theta,\phi) = R_0\left(1 + \alpha_{00} + \sum_{\lambda=1}^{\infty}\sum_{\mu=-\lambda}^{\lambda}\alpha^*_{\lambda\mu}Y_{\lambda\mu}(\theta,\phi)\right) \tag{2.5}$$

where R_0 is the radius of the spherical nucleus, $Y_{\lambda\mu}(\theta\phi)$ are the spherical harmonics and $\alpha_{\lambda\mu}$, the surface coordinates. $\lambda = 0$ corresponds to the so-called breathing mode and can be discarded in the energy range relevant for this work. $\lambda = 1$ contributes to the static dipole term, physically irrelevant as it is the motion of the center of mass, and to the dynamic dipole term, that accounts for the giant dipole resonance. $\lambda = 2$ is of great relevance for this work and corresponds to the quadrupolar deformation of the nucleus. In principle, there are five independent parameters; however, since $\alpha_{21} = \alpha_{2-1} = 0$ and $\alpha_{22} = \alpha_{2-2}$, the number of independent variables reduces to just two, α_{20} and α_{22}. Usually, the quadrupolar deformation is modelled with the coordinates β and γ, given by the transformation 2.6.

$$\begin{aligned}\alpha_{20} &= \beta\cos\gamma \\ \alpha_{22} &= \frac{1}{\sqrt{2}}\beta\sin\gamma\end{aligned} \tag{2.6}$$

The first kind of excitation that can be considered are the *oscillations about a spherical shape*. The quantised form of the collective hamiltonian for these oscillations can be written as

$$\hat{H}_{coll} = \sum_{\lambda\mu}\hbar\omega_\lambda\left(b^\dagger_{\lambda\mu}b_{\lambda\mu} + \frac{1}{2}\right) \tag{2.7}$$

where $b^\dagger_{\lambda\mu}$ is the operator that creates a phonon of multipolarity λ. Solving the Schrödinger equation with the hamiltonian 2.7 yields equidistant energy levels separated by $\hbar\omega_\lambda$. Depending on the multipolarity of the phonons, different spin states are allowed for the excited levels. For instance, for quadrupole phonons the one-phonon state is a 2^+, whereas in the two-photon state 0^+, 2^+ and 4^+ spins are allowed. For octupolar phonons, the first excited state is a 3^- and in the second excited state, spins 0^+, 2^+, 4^+ and 6^+ are allowed.

Next, nuclei that reach stable equilibrium for non-spherical shapes are considered. This an effect that has its origin in quantum mechanics, thus beyond the prediction capability of the liquid drop model. These nuclei with deformed ground states can exhibit *collective rotations*, i.e., they are not invariant under rotations. For the sake of simplicity, the deformation can be assumed to be axially symmetric (which is the most relevant case in this work). In that case, the hamiltonian is given by equation 2.8

$$\hat{H}_{rot} = \frac{\hat{\boldsymbol{I}}^2 - \hat{I}_3^2}{2\mathscr{I}} \tag{2.8}$$

where $\mathscr{I}$ is the moment of inertia of the rigid nucleus and the operator $\hat{I}_3$ is the projection of the total angular momentum $\hat{\boldsymbol{I}}$ onto the body symmetry axis.

Solving the Schrödinger equation with this hamiltonian yields the energies in 2.9.

$$E_{rot} = \frac{\hbar^2}{2\mathscr{I}}\left(J(J+1) - K^2\right) \tag{2.9}$$

where $J(J+1)$ is the eigenvalue of the $\hat{\boldsymbol{I}}^2$ operator and K is the eigenvalue of the $\hat{I}_3$ operator. If the rotation occurs around an axis perpendicular to the nucleus symmetry axis, then $K = 0$, and the ratio between the two first excited states has a value of $R_{42} = 3.33$, characteristic of rotational nuclei.

2.1.3 Mean-field calculations

These are phenomenological calculations that obtain the mean field in which nucleons move as independent particles. They are based on the use of effective nuclear interactions designed to describe data of finite nuclei, like the Skyrme or the Gogny interactions, and make use of the variational method to find the solution of the many-body problem.

This problem can be addressed with the Hartree-Fock (HF) method, in which the many-body wave function of a system of A nucleons is approximated by a *trial* many-body wave function, $|\Phi\rangle$, that is the Slater determinant of a set of A single-particle states derived from the shell-model hamiltonian. The (non-relativistic) interaction hamiltonian is given by equation 2.10.

$$\hat{H} = \sum_{ab} t_{ab} c_a^\dagger c_b + \frac{1}{4} \sum_{abcd} \bar{v}_{abcd} c_a^\dagger c_b^\dagger c_d c_c \tag{2.10}$$

where $c_a^\dagger$ are the creation operators, such that $c_a^\dagger |-\rangle \equiv |a\rangle$ ($|a\rangle$ being a single-particle state), $\bar{v}_{abcd}$ are the anti-symmetrised two-body matrix elements of the interaction that depends on the density matrix ρ, and t_{ab} are the one-body single-particle matrix elements of the kinetic energy. The minimisation of the Hartree-Fock energy, $E^{HF} = \langle\Phi|\hat{H}|\Phi\rangle$, in terms of the density matrix, yields an eigenstate problem for the one-body wave functions. In coordinate space,

$$(T + \bar{V})\phi_a = \epsilon_a \phi_a \tag{2.11}$$

where $\bar{V}$ is the self-consistent Hartree-Fock potential. The Hartree-Fock energy is thus given by an expression that includes the one-body energies and a term that depends on the anti-symmetrised two-body interaction,

$$E^{HF} = \sum_{a=1}^{A} \epsilon_a - \frac{1}{2} \sum_{ab=1}^{A} \bar{v}_{abab} \tag{2.12}$$

This results are, though, derived from an approach that only takes into account the contribution of long-range interactions between nucleons. In order to account for the short-range interaction terms too, pairing correlations must be included in the description. Thus, Hartree-Fock-Bogoliubov theory must be used. It is based on Hartree-Fock theory, as it relies on the variational method to find an approximate solution to the many-body problem defined by the hamiltonian 2.10. However, unlike Hartree-Fock theory, the trial many-body wave function is defined

as a generalised product-like $|\Phi\rangle = \prod_q \beta_q |-\rangle$, where $\beta_k^\dagger = \sum_l U_{lk} c_l^\dagger + V_{lk} c_l$ is the quasiparticle operator. The atomic nucleus can thus be described as set of free quasiparticles that move in the mean-field created by the rest of them. In this case, the Hartree-Fock-Bogoliubov energy is defined as $E^{HFB} = \langle\Phi|\hat{H}|\Phi\rangle$, and its potential energy term includes contributions from both the density matrix (as in the Hartree-Fock theory) and the pairing tensor. The variational method must be applied in order to extract the parameters U and V that minimise E^{HFB}. This process must be performed carefully, since the HFB transformation mixes creation and annihilation single-particle operators. This causes the particle number symmetry to be broken by the HFB wave function, so its restoration is necessary. The Hartree-Fock-Bogoliubov energy can be therefore expressed in terms of the one-body density matrix and one-body pairing tensor.

The mean-field descriptions of the nucleus explained above, in terms of one-body density matrix and pairing tensor, are relatively simple and are not able to predict important spectroscopic information, such as collective motion. Therefore, the mean-field picture is used nowadays as a starting point for more complex nuclear descriptions, generally called *beyond-mean-field* approximations. The so-called Generator Coordinate Method (GCM) is one of them. It is a general method based on the concept of configuration mixing, in which the wave function that describes the system is constructed as a combination of non-orthonormal many-body wave functions $|\Phi(\boldsymbol{q})\rangle$ that depend parametrically on the collective variables $\boldsymbol{q}$, called generating coordinates. This approach allows to predict effects such as axial and triaxial quadrupole deformations or octupole deformations.

2.2 γ decay

In this section, the interaction of quantum mechanical systems with electromagnetic fields will be discussed, in order to derive the relation between the lifetime of an excited state of a nucleus and the properties of the emitted electromagnetic radiation.

The transition probability Γ between the initial state $|J_i M_i\rangle$ and the final state $|J_f M_f\rangle$ in a nucleus is given by the Fermi's Golden Rule. Under the only assumption that the existence of the nucleus is characterised by the current $\boldsymbol{J}$ and charge density ρ produced by its nucleons, and that the wave length of the photon is much higher than the nucleus size, the electric and magnetic multipole operators can be written [Wal04] as in equation 2.13.

$$\begin{aligned}\hat{\mathscr{M}}^{el}_{lm} &= \int x^l Y_{lm}(\Omega_x)\hat{\boldsymbol{\rho}}(\boldsymbol{x})d^3x \\ \hat{\mathscr{M}}^{mag}_{lm} &= \int \left[\hat{\boldsymbol{\mu}}(\boldsymbol{x}) + \frac{1}{l+1}\boldsymbol{r}\times\hat{\boldsymbol{J}}(\boldsymbol{x})\right]\cdot\nabla x^l Y_{lm} d^3x\end{aligned} \tag{2.13}$$

where Y_{lm} are the spherical harmonics. The transition probability from a state $|i\rangle$ to a state $|f\rangle$ can be expressed, in terms of these multipole operators, as:

$$\Gamma(\sigma J; i\to f) = \frac{8\pi}{\hbar}k\frac{1}{2J_i+1}\frac{k^{2J}}{[(2J+1)!!]^2}\frac{J+1}{J}\left|\langle J_f||\hat{\mathscr{M}}^{\sigma}_{J}(k)||J_i\rangle\right|^2 \tag{2.14}$$

where k is the momentum of the emitted photon, and $\hat{\mathscr{M}}^{\sigma}_{J}$ are the multipole operator of character $\sigma = E$ or M and multipolarity J. Note that the dependency on M vanishes thanks to the application of the Wigner-Eckart theorem.

The definition of the *reduced transition probability* arises naturally as [Ber07]:

$$B(\sigma J; i\to f) = \frac{1}{2J_i+1}\left|\langle J_f||\hat{\mathscr{M}}_{J}(k)||J_i\rangle\right|^2$$

Hence,

$$\Gamma(\sigma J; i\to f) = \frac{8\pi}{\hbar}\frac{k^{2J+1}}{[(2J+1)!!]^2}\frac{J+1}{J}B(\sigma J; i\to f)$$

Taking into account that the partial mean lifetime τ_γ is the inverse of the transition rate $\Gamma(\sigma J; i\to f)$, the expression 2.15 for the lifetime is obtained [1],

$$\tau_\gamma^{-1} = \frac{8\pi}{\hbar}\frac{J+1}{J[(2J+1)!!]^2}\left(\frac{E_\gamma}{\hbar c}\right)^{2J+1}B(\sigma J; i\to f) \tag{2.15}$$

The most common reduced transition probabilities values are compiled in table 2.1, where τ is expressed in s and E_γ, in MeV.

[1] In this context $(2l+1)!! = (2l+1)\cdot(2l-1)\cdot(2l-3)\cdot\ldots$

σJ	$\mathbf{B(\sigma J)}$
E1	$6.288 \times 10^{-16} E_\gamma^{-3} \tau_\gamma^{-1}$ e^{2}fm^2
E2	$8.161 \times 10^{-10} E_\gamma^{-5} \tau_\gamma^{-1}$ e^{2}fm^4
E3	$1.752 \times 10^{-3} E_\gamma^{-7} \tau_\gamma^{-1}$ e^{2}fm^6
M1	$5.687 \times 10^{-14} E_\gamma^{-3} \tau_\gamma^{-1}$ μ_N^2
M2	$7.381 \times 10^{-8} E_\gamma^{-5} \tau_\gamma^{-1}$ μ_N^2fm^2

Table 2.1.: $B(\sigma J)$ values for common transitions

The expression in equation 2.15 is obtained under the assumption that the transition occurs only due to photon emission. However, transitions may also occur due to internal conversion of electrons. In order to take this effect into account, a factor α, or internal conversion coefficient, is introduced. The partial lifetime becomes, then:

$$\tau_\gamma = \tau(1 + \alpha)$$

The precise determination of the reduced transition probabilities through the direct measurement of lifetimes is of great importance in spectroscopy, as the $B(\sigma J)$ are very sensitive to the detailed wave functions [Paz17]. A relevant case for this work is the enhancement of the $B(E2)$ values due to the quadrupole collective admixtures.

3 On the measurement of short lifetimes

Excited states of nuclei show a fixed probability of decaying in a time dt to lower states given by λdt, where λ is the inverse of the mean lifetime, $\lambda = 1/\tau$ [Ber07]. The variation in the number of excited states during a time interval dt can be expressed as

$$dN(t) = -\lambda N(t) dt \tag{3.1}$$

The rate at which these states deexcite is defined as $\dot{N}(t) = -dN(t)/dt$. Integrating the equation 3.1 and using the previous definition, the function that relates the deexcitation rate of an excited state and its mean lifetime is obtained:

$$\dot{N}(t) = \frac{n}{\tau} e^{-\frac{t}{\tau}} \tag{3.2}$$

where n is a normalisation factor.

The determination of the mean lifetime of an excited state of a nucleus therefore consists on the mathematical characterisation of the exponential function in equation 3.2. The lifetime τ can be experimentally extracted from the distribution of the difference between the time of population and the time of depopulation of the state, also called *timing*. In the particular case of nuclear mean lifetimes, these times can be identified by the detection of a wide variety of particles, like γ, β, and heavy charged particles, or a combination of them [MGM89; MM89; BC56]. In this work, the detection of the γ rays that populate and depopulate the state is used. Therefore, the minimum required setup for the determination of the lifetime of a nuclear excited state consists of two detectors, each detecting the energies, E_f and E_d, of the transitions characteristic of the state and their occurrence times, t_f and t_d, respectively. Hence, the goal of a timing experiment is the collection of the time difference

$$\Delta T = t_d - t_f \tag{3.3}$$

for a statistically relevant number of events.

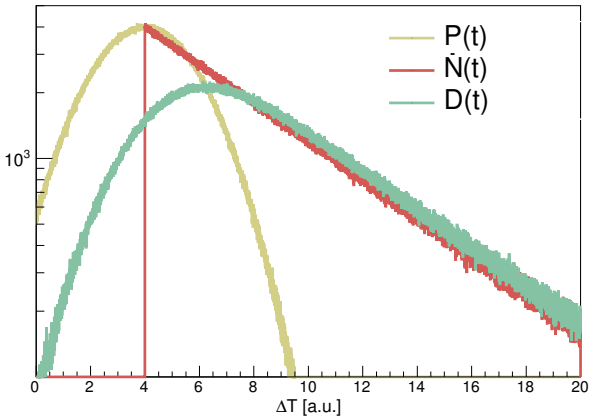

Figure 3.1.: Ideal time difference distributions, without background

The distribution described by equation 3.2 is not accessible experimentally. The usage of an experimental setup affects the pure exponential behaviour of $\dot{N}(t)$, that becomes convoluted with the *prompt response*, $P(t)$, a distribution describing the intrinsic timing resolution of the detectors [BMP51] [BHK55]. For fast timing setups, the prompt response is a gaussian distribution [BHK55] whose Full Width at Half Maximum is a measure of the intrinsic timing resolution.

$$D(t) = P(t) * \dot{N}(t) = \frac{n}{\tau} \cdot \int_{-\infty}^{t} P(x) e^{-\frac{t-x}{\tau}} dx \tag{3.4}$$

Figure 3.1 shows an example of the three aforementioned timing distributions, simulated for $n = 10^7$ events. For a better visualisation, an arbitrary timing offset of $\Delta T_o = 4$ a.u. has been used. In red, the exponential decay distribution is depicted. It is an example of the purely exponential behaviour of the deexcitation process, according to equation 3.2. In yellow, the prompt response distribution of the pair of detectors is shown. In green, the experimentally accessible timing distribution is drawn. It is the convolution of the two previous distributions, according to equation 3.4. $D(t)$ is usually referred to as *delayed distribution*.

There are two perspectives from which the problem of measuring ΔT can be addressed: by means of purely digital methods that take advantage of the novel electronics, on one hand; on the other hand, the most widely used, by means of

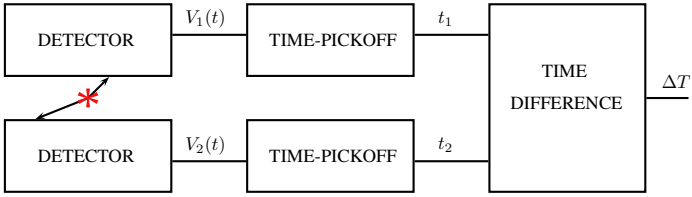

Figure 3.2.: Schematic fast timing setup: a radioactive source emitting rays γ_1 and γ_2 is placed between the detectors. Signals $V_1(t)$ and $V_2(t)$ from the detectors are sent to time pickoff modules, that send logic signals at $t = t_1$ and $t = t_2$ to the last module, where $\Delta T = t_2 - t_1$ is obtained.

traditional, analog electronics. This work was performed with the latter one, and so will be explained here.

Figure 3.2 shows a very basic setup used to perform fast timing measurements. Its purpose is the measurement of the time difference between two time-correlated (coincident) γ rays originated in the radioactive source placed between them. A detailed description of these detectors will be given in chapter 4. This kind of setup accommodates as many time-pickoff modules as radiation detectors. Each of them provides a logic signal at the moment a γ-ray is detected. These logic signals originating from time-correlated γ-rays are sent to the subsequent module, for their values to be subtracted, and obtain ΔT. The next section is devoted to the explanation of the most common time-pickoff methods.

3.1 Time-pickoff methods

The simplest method is called leading-edge triggering: the logic time signal is generated at the moment the analog pulse crosses a certain threshold, common for the whole setup. This method, however, is inherently subject to problems of walk [Leo87], which consists of the loss of timing resolution due to variations in the amplitude or rise-time of the detectors signals. The walk effect due to variations in the amplitude can be clearly observed in figure 3.3, where simultaneous signals of different energy yield a measured time difference of $\Delta T \neq 0$.

The existence of an optimum triggering fraction for leading-edge timing stimulated the design of a circuit that would trigger at the optimum triggering fraction, regardless of the input pulse height [Pau85]. This is the so-called constant fraction trigger, and was the one used in this work. In constant fraction triggering, the logic signal is generated at the moment the analog pulse crosses a threshold set to a con-

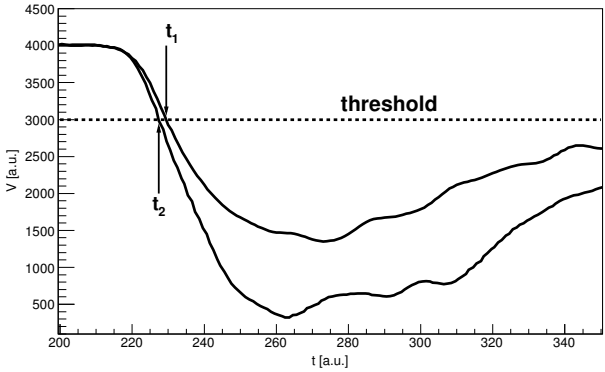

Figure 3.3.: Time-walk effect due to amplitude variations with leading-edge timing: Two simultaneous signals of different energy cross the threshold at different times, producing $\Delta T = t_1 - t_2 \neq 0$.

stant fraction of the pulse amplitude, *A*. Figure 3.4 shows the essentially walk-free timing between two simultaneous signals of different energy.

The technique by which constant fraction triggering is achieved consists of the following steps: first the input signal V_{in} is split in two signals: one of them is delayed by t_d, whereas a constant fraction $k \in [0, 1]$ of the other one is inverted; next, these two signals are added up to form $V'(t)$ (equation 3.5).

$$V'(t) = V_{in}(t - t_d) - k \cdot V_{in} \tag{3.5}$$

Finally, the time t_{zc} such that $V'(t_{zc}) = 0$, or time of zero-crossing, is at the constant fraction k of the original signal amplitude [Leo87].

The choice of the parameters k and t_d determines the shape of the bipolar signal $V'(t)$ and its timing properties [Pau85]. In particular, two cases can be considered: the true-constant-fraction (TCF) timing and the amplitude-and-rise-time-compensated (ARC) timing. A summary of the parameters constraints and the most relevant differences these constraints cause, is shown in table 3.1 [Pau85; Rég+10].

The first row is dedicated to the relationships between the signal intrinsic properties, such as t_r or $V_{in}(t)$, and the constant-fraction parameters that define each of the methods, such as k, t_d. The second row shows the zero-crossing time derived for each method. As expected, there is an explicit dependency with rise-time only in the case of TCF.

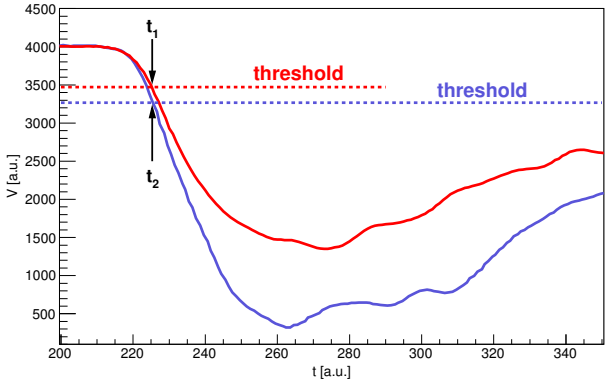

Figure 3.4.: Constant fraction timing: Two simultaneous signals of different energy cross their respective thresholds at very close times, producing $\Delta T = t_1 - t_2 \approx 0$. Thresholds are set to 20% of the amplitude.

Mode	TCF	ARC
Criteria	• $t_d > t_r(1-k)$ • t_d such that t_{zc} occurs during the time that $V_{in}(t)$ is at its peak	$t_d < t_r(1-k)$
$\boldsymbol{t_{zc}}$	$t_d + kt_r$	$\frac{t_d}{1-k}$
$\left.\frac{dV'(t)}{dt}\right\|_{t=t_{zc}}$	A/t_r	$A(1-f)/t_r$
$\boldsymbol{t_{walk}}$	$\sqrt{\frac{2q}{A/t_r}}$	$\sqrt{\frac{2q}{A(1-k)/t_r}}$

Table 3.1.: Main properties of true-constant-fraction and amplitude-and-rise-time-compensated timing.

However, small walk effects still remain for both modes, due to the dependency of the $V'(t)$ slope at the zero-crossing time on the signal amplitude and rise-time. $\left.\frac{dV'(t)}{dt}\right|_{t=t_{zc}}$ is analytically written in the third row of table 3.1, and its value is a direct consequence of the rate charge from the detector gets accumulated. Assuming the charge sensitivity q for the zero-crossing comparator (that is, the minimum measurable amount of charge) to be constant, different charge collection rates necessarily imply differences in the zero-crossing times. This time variance, t_{walk}, shows a dependency on amplitude and rise-time both for TCF and ARC timing (table 3.1). Furthermore, assuming a linear dependency of amplitude and energy, t_{walk} can be described both for TCD and ARC timing by equation 3.6.

$$t_{walk}(E) = \frac{a}{\sqrt{E+b}} + c \tag{3.6}$$

where q, A, t_r and k dependencies have been merged into the free adjusting parameters a, b and c, that can be fitted to experimental data [Rég+10].

3.2 Methods to determine τ

When the lifetime τ of interest is longer than the timing resolution of the setup, the exponential behaviour of the delayed distribution $D(t)$ is evident (figure 3.1), and the most straightforward method to obtain τ is by a linear fit of the semilogarithmic plot of the delayed distribution $D(t)$; this method is called the *Slope Method*. A more precise result can be achieved with the *Convolution Method* if the fit of $D(t)$ is performed with the convolution of the exponential decay and the prompt response, instead (equation 3.4) [Rég+10].

However, in the frequent case of the lifetime τ being comparable or shorter than the timing resolution of the setup, the slope and convolution methods are no longer applicable. In the following sections, the *Centroid Shift*, the *Mirror Symmetric Centroid Difference* and the *Generalised Centroid Difference* methods will be explained.

3.2.1 Centroid Shift Method

The centroid shift method is based on the following statements:

(i) The delayed distribution, $D(t)$, is shifted with respect to the prompt distribution, $P(t)$, by τ [Bay50].

Considering equation 3.4 and the fact that the first moments of two distributions are additive under convolution [Jay03], the following relationship between the exponential decay, the prompt and the delayed distributions can be stated:

$$M^{(1)}[D(t)] = M^{(1)}[P(t)] + M^{(1)}[\dot{N}(t)] \tag{3.7}$$

where $M^{(n)}[f(x)]$ is the n-th moment of the distribution $f(x)$.

The values of the moments are:

$$\begin{aligned} M^{(1)}[D(t)] &= C^D \\ M^{(1)}[P(t)] &= C^P \\ M^{(1)}[\dot{N}(t)] &= \tau \end{aligned} \tag{3.8}$$

where C^D and C^P stand for the centroid of the delayed and the prompt distributions, respectively. As Z. Bay showed already in 1950:

$$C^D = C^P + \tau \Longrightarrow \tau = C^D - C^P \tag{3.9}$$

Figure 3.5 shows the distributions related to the determination of the lifetimes, $\tau_1 > \tau_2 > \tau_3$, of states that are populated through a transition of energy E_f (that provides time t_1) and depopulated through a transition of energy E_d (that provides time t_2), with no background contribution. The prompt response distribution remains unchanged, since the response of the fast timing setup does not depend on the lifetime being measured. Each of the exponential decays represents a different lifetime. This behaviour is, consequently, inherited by the delayed distributions, drawn in green. The determination of the centroids position for the prompt and delayed distributions in each case allows for the determination of the lifetime, through equation 3.9.

Note that $\tau_1 > FWHM_{setup}$, which allows for the application of any of the methods explained in the previous section; however, $\tau_3 < FWHM_{setup}$, which makes the applicability of the slope or convolution methods impossible. $\tau_2 \approx FWHM_{setup}$ is as an example of an intermediate case.

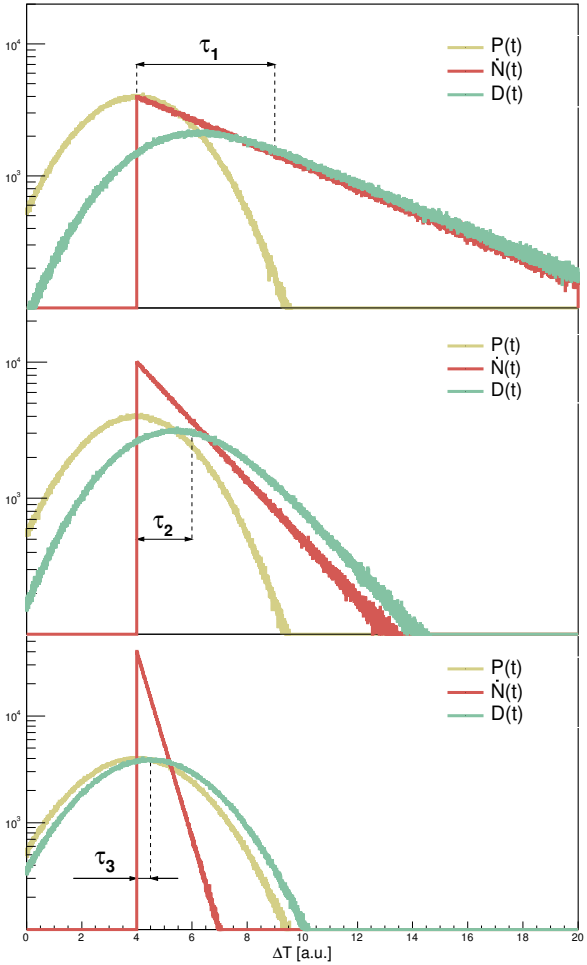

Figure 3.5.: Delayed timing distribution dependency with lifetime: The difference between the centroids of $D(t)$ and $P(t)$, which is the basis of the centroid shift method, is illustrated.

(ii) Time-walk is energy dependent (equation 3.6).

Equation 3.6 implies that the value of ΔT measured by a standard fast timing setup cannot be longer described by equation 3.3, which must be corrected with an energy-dependent term:

$$\begin{aligned} \Delta T(E_f, E_d) &= t_2 - t_1 + t_{2_{walk}}(E_d) - t_{1_{walk}}(E_f) \\ &= t_2 - t_1 + \Delta T_{walk}(E_f, E_d) \end{aligned} \tag{3.10}$$

The precise determination of ΔT is, therefore, subject to the precise knowledge of $\Delta T_{walk}(E_f, E_d)$, or *time-walk characteristics* of the setup.

Figure 3.6 shows the delayed distributions in three different cases for which the transitions are prompt ($\tau_1 = \tau_2 = \tau_3 = 0$), unlike the case depicted in figure 3.5. Hence the delayed distributions coincide with the prompt response ones. However, the energies of the γ-ray transitions that populate the state (and provide the time t_1) are different ($E_1 < E_2 < E_3$), and so are the $t_{1_{walk}}$ values, for each case. The energy E_d of the γ-ray that depopulates the state (and provides the time t_2) is kept constant, for the sake of simplicity (so is $t_{2_{walk}}$).

The dependency of the prompt centroid on energy is called *prompt curve*. It is usually determined with standard radioactive sources with very well known transitions and lifetimes, by gating one detector constantly on a directly depopulating ($E_{ref} = E_d$, as in the example given in figure 3.6) or populating ($E_{ref} = E_f$) transition of interest. The other detector selects coincident transitions of different energies for their centroids to be measured. The prompt centroid is therefore obtained by the direct application of equation 3.9.

The combination of (i) and (ii) makes the determination of any lifetime simple from a mathematical point of view (equation 3.11 and figure 3.7),

$$\tau = C^D(E_f) - C^P(E_f) \tag{3.11}$$

but still subject to the precise knowledge of the centroid of the delayed distribution, and the reference energy prompt curve. In general, the energies of the transitions that populate or depopulate the state of interest are different from E_{ref}. Hence both time signals are not time-walk free, which makes the lifetime determination complex and eventually even impossible [Rég+10].

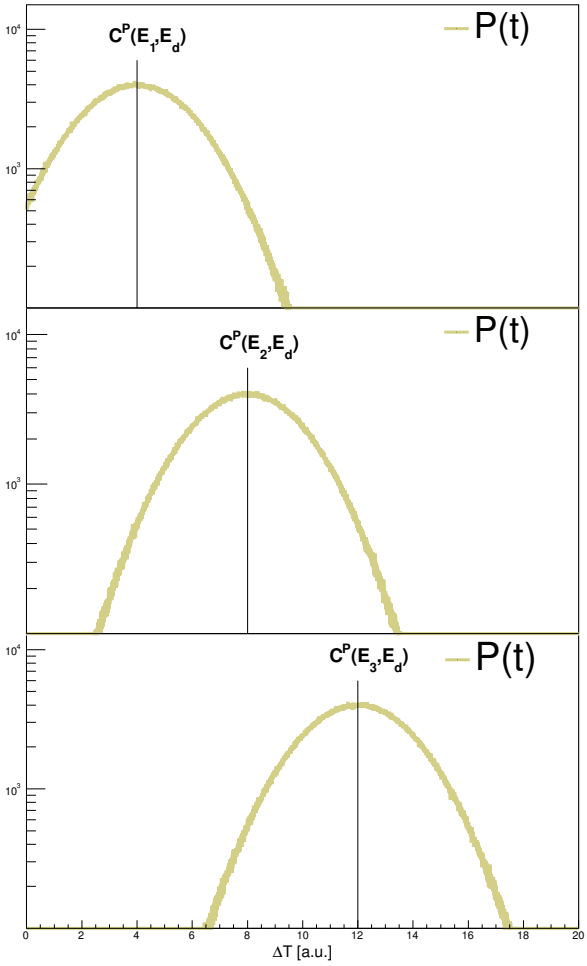

Figure 3.6.: Prompt distribution dependency with energy: E_d has been used as reference, thus $t_{2_{walk}}$ is the same in the three cases.

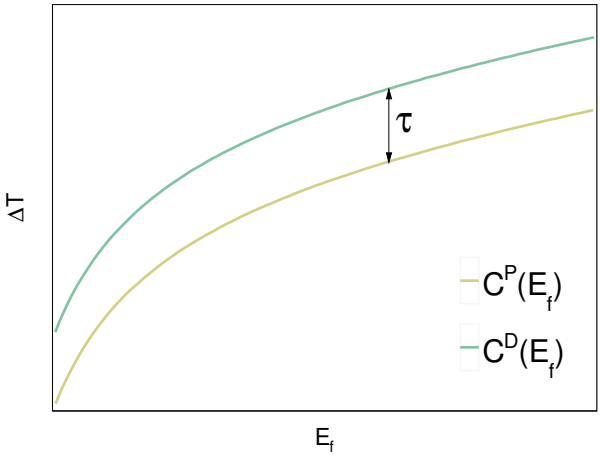

Figure 3.7.: Delayed and prompt distributions centroid dependency on energy. The delayed distribution centroid is shifted by τ with respect to the prompt centroid.

3.2.2 Mirror Symmetric and Generalised Centroid Difference Methods

To overcome this problem, J.-M. Régis developed the *Mirror Symmetric Centroid Difference Method* [Rég+10; Rég11]. It is based on the same two statements as the Centroid Shift Method, but it takes advantage of the fact that either γ-ray populating or depopulating the state of interest may produce the time signal t_1 or t_2. Two timing distributions are therefore generated from the value of ΔT in equation 3.10. When the transition that depopulates the state provides t_2, usually referred to as t_{stop}, and the one that populates it provides t_1 (t_{start}), the timing distribution is called *delayed* distribution. On the contrary, when the transition that depopulates the state provides t_{start} and the one that populates it provides t_{stop}, the timing distribution is called *antidelayed* distribution [1]:

[1] The convention that designates the two branches of a fast timing setup as *start* and *stop* proceeds from the terminology used in the Time-to-Amplitude Converter modules. Their output consists of logic signals whose amplitude is proportional to the time difference between the two input signals, $\Delta T = t_2 - t_1 \equiv t_{stop} - t_{start}$.

$$\begin{aligned}\Delta T_{del} &= t_d - t_f + t_{walk}(E_d) - t_{walk}(E_f)\\ \Delta T_{antidel} &= t_f - t_d + t_{walk}(E_f) - t_{walk}(E_d)\end{aligned} \tag{3.12}$$

These two distributions also fulfil equations 3.7 and 3.8. Taking into account that $M^{(1)}[\dot{N}(t)_{del}] = -M^{(1)}[\dot{N}(t)_{antidel}] = \tau$, equation 3.9 becomes:

$$\begin{aligned}C^D_{del}(E_f, E_d) &= C^P_{del}(E_f, E_d) + \tau\\ C^D_{antidel}(E_f, E_d) &= C^P_{antidel}(E_f, E_d) - \tau\end{aligned} \tag{3.13}$$

Subtracting the two equations in the set 3.13 yields:

$$C^D_{del}(E_f, E_d) - C^D_{antidel}(E_f, E_d) = C^P_{del}(E_f, E_d) - C^P_{antidel}(E_f, E_d) + 2\tau \tag{3.14}$$

The definition of two new variables arises naturally from equation 3.14:

$$\Delta C(E_f, E_d) = C^D_{del}(E_f, E_d) - C^D_{antidel}(E_f, E_d) \tag{3.15}$$

$$\Delta C^P(E_f, E_d) = C^P_{del}(E_f, E_d) - C^P_{antidel}(E_f, E_d) \tag{3.16}$$

And equation 3.14 becomes:

$$\Delta C(E_f, E_d) = \Delta C^P(E_f, E_d) + 2\tau \tag{3.17}$$

The extraction of the lifetime is therefore subject to the precise measurement of $\Delta C(E_f, E_d)$ and the precise knowledge of the prompt response centroid difference for that specific energy combination. Figure 3.8 shows a graphical example of the relations between the relevant distributions in the determination of a lifetime.

In general $\Delta C^P(E_f, E_d)$ which is not achievable experimentally can be expressed as a function of two energy values, E_1 and E_2:

$$\begin{aligned}\Delta C^P(E_1, E_2) &= C^P_{del}(E_1, E_2) - C^P_{antidel}(E_1, E_2)\\ &= t_{walk}(E_2) - t_{walk}(E_1) - t_{walk}(E_1) + t_{walk}(E_2)\\ &= 2\left[t_{walk}(E_2) - t_{walk}(E_1)\right]\end{aligned} \tag{3.18}$$

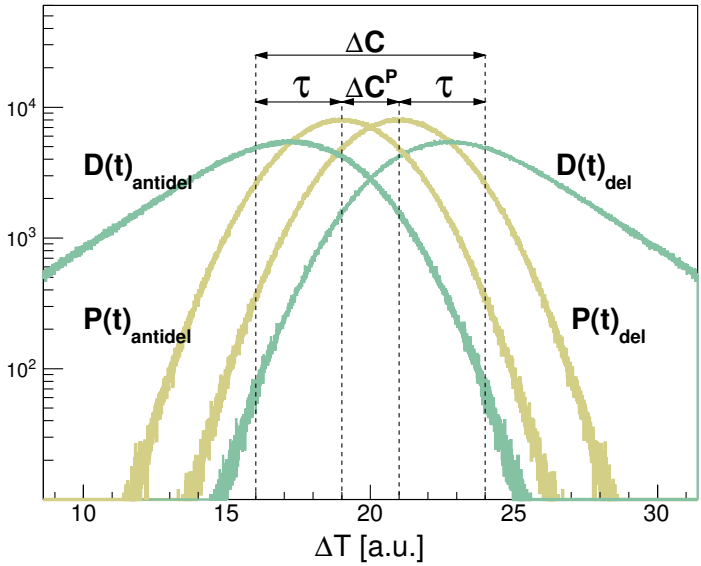

Figure 3.8.: Delayed and prompt distribution in the mirror symmetric centroid difference method: These distributions are obtained for a certain combination of energies E_f and E_d. Each of the distributions $D(t)$ are shifted by τ with respect to their corresponding prompt distributions.

which only depends on the shape of $t_{walk}(E)$, hence on the behaviour of the experimental setup. For the calibration procedure, it is useful to establish an energy value, E_0, as origin of time-walk. For convenience $\Delta C^P(E_1, E_2)$ must be modified to depend on the variables E_0 and $\Delta E = E - E_0$. Then,

$$\Delta C^P(E_1, E_2) \mapsto \Delta C^P(E_0, \Delta E) = 2\,[t_{walk}(E_0) - t_{walk}(E_0 + \Delta E)] \tag{3.19}$$

$\Delta C^P(E_0, \Delta E)$ dependency on E_0 vanishes, though, as the value E_0 is constant. Equation 3.19 becomes:

$$\Delta C_0^P(\Delta E) = 2[\underbrace{t_{walk}(E_0)}_{T_0} - t_{walk}(E_0 + \Delta E)] \tag{3.20}$$

where $\Delta C_0^P(\Delta E)$ refers to the prompt centroid difference for a specific time-walk-reference energy E_0. Analytically, $\Delta C_0^P(\Delta E)$ consists on a vertical and a horizontal translation of $T_0 = t_{walk}(E_0)$ and $-E_0$, respectively, of the inverted $t_{walk}(E)$. For the particular case of a cascade that involves two transitions, γ_f and γ_d of energies E_f and E_d respectively,

$$\begin{cases} \Delta C_0^P(\Delta E_f) = 2[T_0 - t_{walk}(E_0 + E_f - E_0)] = 2[T_0 - t_{walk}(E_f)] \\ \Delta C_0^P(\Delta E_d) = 2[T_0 - t_{walk}(E_0 + E_d - E_0)] = 2[T_0 - t_{walk}(E_d)] \end{cases} \tag{3.21}$$

where $\Delta E_f = E_f - E_0$ and $\Delta E_d = E_d - E_0$. If both equations in system 3.21 are subtracted, the dependency on T_0 vanishes:

$$\Delta C_0^P(\Delta E_f) - \Delta C_0^P(\Delta E_d) = 2[t_{walk}(E_d) - t_{walk}(E_f)]$$

that coincides with the value of $\Delta C^P(E_f, E_d)$ in equation 3.18.

$$\underbrace{\Delta C_0^P(\Delta E_f)}_{PRD(E_f)} - \underbrace{\Delta C_0^P(\Delta E_d)}_{PRD(E_d)} = \Delta C^P(E_f, E_d) \tag{3.22}$$

Equation 3.22 is commonly applied to perform the calibration of $\Delta C^P(E_f, E_d)$ through the usage of standard radioactive sources that provide prompt transitions used as time-walk references. It is very usual to refer to $\Delta C_0^P(\Delta E)$ as $PRD(E)$, or *Prompt Response Difference*.

The value of the lifetime can be finally expressed as:

$$\tau = \frac{1}{2}\left[\Delta C - [PRD(E_f) - PRD(E_d)]\right] \tag{3.23}$$

In a more recent publication, J.-M. Régis and collaborators [Rég+13] presented the *Generalised Centroid Difference Method*, where the feasibility of lifetime measurements using an array equipped with N equally-shaped $LaBr_3(Ce)$ scintillator detectors was demonstrated. Equation 3.24 represents the generalised centroid difference:

$$\tau = \frac{1}{2}\left[\overline{\Delta C} - [\overline{PRD}(E_f) - \overline{PRD}(E_d)]\right] \tag{3.24}$$

where $\overline{\Delta C}$ is the mean of the centroid difference and $\overline{PRD}$, the mean of the prompt response difference, for the whole array, independently of the pair of detectors combination.

4 FATIMA and Gammasphere

4.1 FATIMA

4.1.1 $LaBr_3$(Ce) scintillators

Cerium-doped lanthanum bromide is an inorganic, scintillating crystal invented in the beginning of the century [Loe+01]. It became one of the most promising novel scintillators for potential application in γ-ray detection, surpassing other very similar candidates also under investigation, like cerium-doped $LaCl_3$, $LuBr_3$ or $LuCl_3$ [GN+99].

Scintillators can be generally described as waveshifters: they convert the wavelength of energetic particles (α, β, γ) into a large number of photons with longer wavelength (or smaller energy) through the process called scintillation. In the case of inorganic scintillators, the scintillation mechanism can be described in four main phases [Lec+06]:

(i) *Energy conversion*. This phase starts with the production of primary electronic excitations by the interaction of ionising particles with the material. In a characteristic time of between 10^{-16} and 10^{-14} seconds after the initial energy release, a large number of secondary electronic excitations are produced through processes such as inelastic electron-electron scattering, that cause the creation of electrons in the conduction band and holes in core and valence bands. In general, this process continues until all electrons in the conduction band have an energy smaller than $2E_g$, that is the electron-electron inelastic scattering threshold, and all holes occupy the valence band. In the particular case of cerium-doped compounds, like $LaBr_3$(Ce), the process extends until all electrons in the conduction band have an energy smaller than $E_g + E_{Ce^{3+}}$, where $E_{Ce^{3+}} < E_g$ is the excitation energy of the Ce^{3+} ions.

(ii) *Thermalisation*. The second stage is the thermalisation of electronic excitations with production of phonons, leading to low kinetic energy electrons in the bottom of the conduction band and holes in the top of the valence band. This takes place between 10^{-14} and 10^{-12} s after the production of the primary excitations.

(iii) *Transfer to luminescent centers*. The third stage, that extends until 10^{-8} s, is characterised by the localisation of the excitations through their interaction with stable defects and impurities in the material. In Ce^{3+} doped crystals, there are two main processes that lead to the creation of excited luminescent centers [BD07]. Both of them are driven by the position of the $4f$ level of cerium [Lec+06], slightly above the $LaBr_3$ lattice valence band, in the forbidden energy band gap. This condition enhances the probability of capturing a hole leading to the following processes:

- *Prompt capture*, i.e., faster than 1 ns, *of a free hole and a free electron* from the ionisation track by luminescent centers Ce^{3+} leading to $4f \rightarrow 5d$ excitation.

$$Ce^{3+} + h^+ \rightarrow Ce^{4+}$$
$$Ce^{4+} + e^- \rightarrow Ce^{3+^*}$$

- *Thermally activated energy transfer from self-trapped excitons to Ce*. Initially, a hole is trapped by two bromine anions Br^- to form a self-trapped hole center, V_k, that subsequently traps an electron to form a self-trapped exciton.

$$2\ Br^- + h^+ \rightarrow V_k$$

$$V_k + e^- \rightarrow \text{STE}$$

$$Ce^{3+} + \text{STE} \rightarrow Ce^{3+^*}$$

The second process is highly temperature dependent, and its occurrence at room temperature can be neglected [BD07].

(iv) *Light emission*. The last phase happens from times $t > 10^{-10}$ s. It is the relaxation of the luminescent centers Ce^{3+^*} via the transition $5d \rightarrow 4f$:

$$Ce^{3+^*} \rightarrow Ce^{3+} + h\nu$$

and the emission of photons of energy $h\nu$.

The $4f$ configuration of the Ce^{3+} ion actually consists of two spin-orbit components [Lec+06] that cause the $5d \rightarrow 4f[^2F_{5/2}, ^2F_{7/2}]$ emission to be split in two bands centered at 355 nm and 385 nm [Ale+14]. Photons emitted by the luminescent centers are traditionally referred to as *optical photons*, even if their energy lays out of the visible spectrum.

These processes confer $LaBr_3$(Ce) crystals properties very convenient for fast-timing and spectroscopy compared to other scintillators, as it can be seen in table 4.1.

Scintillator	Light yield [ph./keV]	τ [ns]	ρ [g/cm^3]
$LaBr_3$(Ce)	63	16	5.08
$LaCl_3$(Ce)	49	28	3.85
NaI(Tl)	38	250	3.67
BaF_2	1.8	0.7	4.88
BGO	9	300	7.13

Table 4.1.: Main properties of common inorganic scintillation materials [Bria]

On one hand, the light yield is directly related to the energy resolution of the scintillator; the higher the amount of optical photons is, the better the energy resolution becomes. On the other hand, the decay time, τ, is related to the timing performance of the detector, achieving better timing resolution for faster decay times. The density of the material is also a magnitude relevant for γ-ray spectroscopy, since it is directly related to the probability of interaction of the radiation with the detector material and, subsequently, to the detection efficiency. Among all scintillators presented in table 4.1, $LaBr_3$(Ce) is the one that offers the best trade between light yield, decay time and density. Considering its relatively recent discovery, it is obvious that BGO is the preferred detector for applications that do not require good energy nor timing resolution, but only high detection efficiency, like in the Compton-suppression shields; that BaF_2 has been the preferred detector to perform fast-timing measurements (it still is when energy resolution is not a limiting factor); or that NaI(Tl) has been the most natural solution for the performance of γ-ray spectroscopy with inorganic scintillators.

4.1.2 Photomultiplier tubes

The next step in the detection chain is the conversion of the optical photons emitted by the scintillator into charge. This is done by the usage of photomultiplier tubes

(PMT). A photomultiplier tube is a vacuum tube consisting of an input window, a photocathode, focusing electrodes, an electron multiplier and an anode usually sealed into an evacuated glass tube [Ham].

The processes that occur in the PMT are:

(i) The incoming optical photons pass through the input window.

(ii) They are absorbed in the photocathode, which emits electrons (also called *photoelectrons*) via the photoelectric effect.

(iii) The photoelectrons are accelerated by an electric field produced by the focusing electrode, that also focuses the electron beam onto the first dynode.

(iv) Every photoelectron hit on the first dynode causes the creation of a large number of secondary electrons, that are accelerated towards the next dynode. This multiplication process is repeated at every dynode.

(v) The secondary electrons emitted from the last dynode are collected by the anode, from where they are extracted.

Several photomultiplier tube properties affect the rate at which charge is generated, multiplied, and eventually extracted for its delivery to the subsequent electronic modules. Features like the photocathode material, number or layout inside the tube of the dynodes must be carefully chosen to optimise the fast timing setup performance.

4.1.3 FATIMA detectors

The FATIMA (**FA**st **TIM**ing **A**rray) will be the apparatus devoted to the detection of γ-rays for the measurement of excited levels lifetimes in the sub-nanosecond regime in the DESPEC (**DE**cay **SPEC**troscopy) experiment of the NUSTAR (**NU**clear **ST**ructure, **A**strophysics and **R**eactions) Collaboration, one of the four physics pillars of the upcoming FAIR (**F**acility for **A**ntiproton and **I**on **R**esearch) [Fra+15], which is being built in Darmstadt, Germany. However, prior to the construction of FAIR, the name FATIMA refers to the array of a variable amount of detectors that are tested in various experimental campaigns to study their joint performance.

The main physics requirements for the FATIMA detectors are a good timing resolution over an extended energy range, sufficient detection efficiency and reasonable energy resolution. Their fulfilment is achieved by the coupling of the $LaBr_3$:5%Ce scintillators manufactured by Saint-Gobain under the commercial

name BrilLanCe380 [Sai] to the Hamamatsu photomultiplier tubes R9779 [Pmt] to form the FATIMA detector. Originally, these photomultiplier tubes feature a single output to extract the electric charge collected in the anode [Pmt]; in newer versions, their bases have been modified in order to enable the extraction of the electric charge from the last dynode, as well. This change is motivated by the convenience of having energy and time measured independently from those two output signals, not affecting the performance of neither the energy nor the timing resolution [Bel+16] [Fra+15]. Figure 4.1 shows the emission spectrum of the scintillators [Dro+08] and the quantum efficiency of the R9779 photomultiplier photocathode [Pmt], made out of bialkali. The very good overlap between both distributions ensures the optimum conversion of optical photons emitted by the crystal into photoelectrons, resulting in a very good energy resolution $R(@662\text{keV}) = 3\%$ [Fra+15]. In addition, a good timing performance of the detector is ensured by the combination of fast decay time of the $LaBr_3(Ce)$ scintillators, of $\tau_d = 16$ ns [Bria], and good timing characteristics of the photomultiplier tube, that shows a transit time spread of $TTS = 250$ ps [Pmt].

Among the drawbacks that $LaBr_3(Ce)$ scintillators exhibit, their high hygroscopy and their intrinsic radioactivity stand out. The first one entails the usage of vacuum-tight encapsulation for the crystal, to prevent its contact with moisture in the air that would damage the crystal and worsen its performance; the second one originates from the decay of ^{138}La and ^{227}Ac, and results in the detection of γ-rays and β^- particles following the decay of ^{138}La, and γ-rays and α particles from the decay chain of ^{227}Ac. The natural abundance of ^{138}La is less than 0.1% and its half-life is $T_{1/2} \approx 10^{11}$ years, making its activity very weak, yet unavoidable. Ac is present in $LaBr_3(Ce)$ crystals as a contaminant, since it is chemically homologous to La [Qua+13]. Among its isotopes, only ^{227}Ac has a half-life sufficiently long ($T_{1/2} \approx$ 22 years) for its decay products to be measurable. A more detailed description of the presence of contaminants in scintillator crystals can be found in appendix A.

Figure 4.2 shows a FATIMA detector. The $LaBr_3(Ce)$ scintillator is placed on the right side. It is a cylindrical crystal with a diameter of 1.5 inches and a length of 2 inches. To minimise the detection of γ-rays scattered by the neighbouring detectors, a tubular lead shield is placed around it. On the left side, the photomultiplier assembly H10570, that includes the Hamamatsu R9779 photomultiplier is placed.

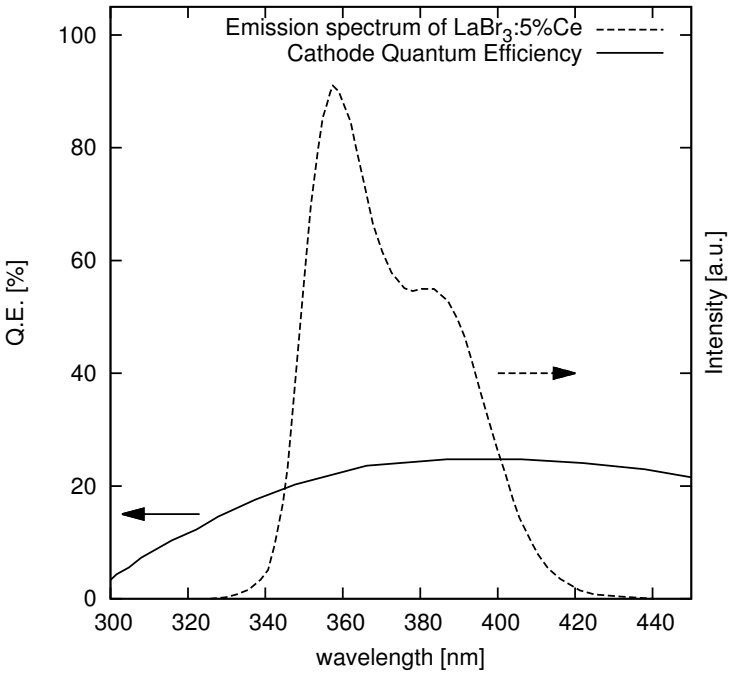

Figure 4.1.: Overlap of the emission spectrum of $LaBr_3$(Ce) [Dro+08] and the spectral response of the photocathode of the Hamamatsu R9779 PMT [Pmt]. Note that the emission spectrum of $LaBr_3$(Ce) shows two bands distributed around 355 nm and 385 nm.

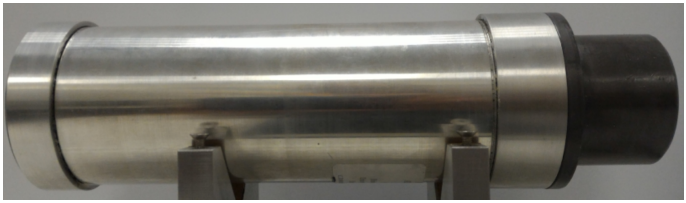

Figure 4.2.: A FATIMA detector [Gam].

4.2 Gammasphere

4.2.1 High-purity germanium detectors

Germanium detectors are semiconductor diodes having a p-i-n structure in which the intrinsic region is sensitive to ionising radiation [Can16]. The qualifying term *high-purity* is reserved for materials for which the impurity concentration corresponds to levels that are less than 1 part in 10^{12} [Kno89]. When the incoming particles deposit their energy, a large amount of electrons and holes are promoted to the conduction and valence band, respectively, and swept to the p and n electrodes by the electric field across the intrinsic region.

The amount of charge collected therefore depends on the energy deposited by the incoming ionising radiation and on the energy necessary to create an electron-hole pair. The smallness of its value in the case of HPGe detectors causes the production of a large amount of charge carriers per unit of deposited energy, that results in very good energy resolution. Large coaxial detectors will produce FWHM values of 800-1200 eV at 122 keV, rising to 1.7-2.3 keV at 1333 keV [Kno89]. However, thermal generation of charge carriers must be kept as low as possible, in order to preserve that energy resolution. This is achieved by mounting the detector in a vacuum chamber which is attached or inserted into a liquid nitrogen ($T = 77\,\mathrm{K}$) Dewar.

4.2.2 The Gammasphere array

The Gammasphere is the high-purity germanium detector array of the ATLAS (**A**rgonne **T**andem **L**inac **A**ccelerator **S**etup) facility in the Argonne National Laboratory (Illinois, USA). It consists of 110 Compton-suppressed large volume germanium detectors that can achieve low background measurements for high fold coincidence experiments [Lee90], and reach a maximum photopeak efficiency of $\varepsilon \approx 19\%$ at $E_\gamma \approx 300$ keV [Gse].

Figure 4.3 shows a section of the Gammasphere. The HPGe detector, mounted inside a cryostat, and the bismuth germanate ($Bi_4Ge_3O_{12}$, usually referred to as BGO) escape-suppression shield form a coaxial arrangement. The HPGe detector has a diameter of 71 mm and a length of 80 mm. The BGO escape-suppression shield has a hexagonal outer shape and is made of six optically separated segments. A cylindrical BGO back catcher (suppressor plug) is mounted behind the HPGe detector. The BGO detectors are sufficiently thick to provide adequate Compton suppression. The BGO escape-suppressor is shielded against direct radiation from

Figure 4.3.: Gammasphere detectors. Figure taken from [Gsf].

the γ-ray source by means of a heavy metal collimator, *hevimet*, which consists of an alloy with a large γ-ray absorption coefficient. In this way a false suppression of full energy events in case of high-multiplicity γ-rays cascades is minimised. The whole array is mounted in a hemispherical supporting frame [PG97].

4.3 FATIMA&Gammasphere combined array at ANL

The combined use of $LaBr_3$(Ce) detectors with additional detectors (in particular, HPGe detector arrays) has been already done in several occasions to perform fast timing measurements. One can mention the ones carried out with the ROSPHERE at IFIN-HH [Mas+13], with EXILL at ILL [Ili+16] [Rég+14], with EURICA at RIKEN [Bro+15a] [Bro+15b] or with IDS at ISOLDE [Lic+17].

For the experiment analysed in this work, a hemisphere of the Gammasphere including 51 HPGe detectors is used in combination with a set of 25 FATIMA detectors in an arrangement that covers the 4π solid angle. Both arrays are placed such that the γ-ray source occupies the focal point of the two semispheres.

Figure 4.4 shows the positions of the $LaBr_3$(Ce) detectors in the array. The photomultiplier tubes are drawn in red, while the lead shield that surrounds the $LaBr_3$(Ce) crystals is drawn in light blue. Figure 4.5 illustrates the combined arrangement of both the FATIMA and the Gammasphere array.

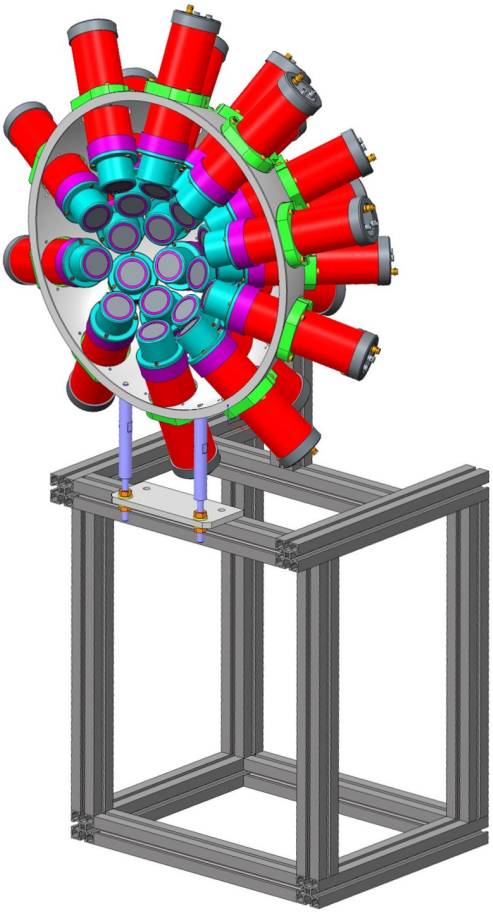

Figure 4.4.: View of the FATIMA arrangement as used in the experiment. The photomultipliers are drawn in red and the lead shields of the $LaBr_3$(Ce) detectors, in bright blue [Lal].

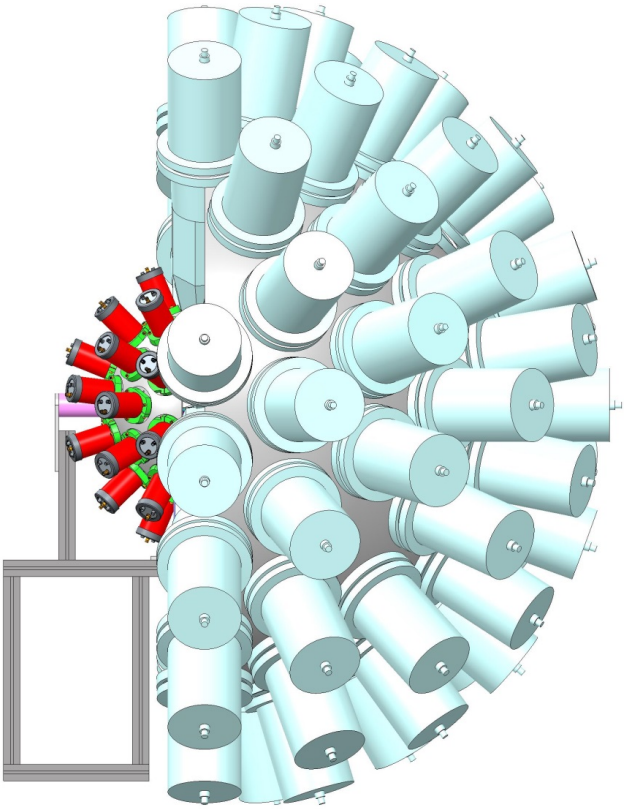

Figure 4.5.: Profile of the two arrays around the source. On the left side, the FATIMA. On the right side, the hemisphere of Gammasphere [Lal].

5 Experiment

This experiment is part of the set of experimental campaigns intended to test the feasibility and flexibility of the FATIMA in combination with complementary detector arrays [Fra+15]. It took place at the Argonne National Laboratory (Illinois, USA) at the turn of the year 2015/2016. Details about the source, the data acquisition system, the data sorting and the detectors calibration are given in this chapter.

5.1 ^{252}Cf spontaneous fission source

Spontaneous fission is the process that results in the splitting of a very heavy nucleus into two (or more) lighter fragments, without any external influence [Li08]. All heavy nuclei are subject to a strong repulsive force of electrostatic origin; however, this force is compensated and eventually inhibited by the attractive nuclear force for almost all of them. Spontaneous fission is therefore not a significant process but only for some transuranic isotopes of very large mass number [Kno89].

The most widely used example is ^{252}Cf, with a half-life of $T_{1/2} = 2.65$ years. However, it does not always undergo spontaneous fission. The probability for α emission is much higher than that for spontaneous fission, because the Coulomb barrier an α particle must overcome to split from a ^{248}Cm nucleus is much smaller than the Coulomb barrier a heavier fragment must overcome to split from the other fragment. In a ^{252}Cf sample, less than 3.2% of the total decays undergo spontaneous fission [Kno89] [Nnd], while the remaining ones undergo α decay, to form ^{248}Cm, that has a very long half-life of $T_{1/2} = 3.5 \times 10^5$ years.

After a spontaneous fission happens, some neutrons are evaporated from the two fragments, until their emission becomes energetically impossible. Then, the only favourable way for the so-called *secondary fragments* to release their energy is through the emission of γ rays.

In every fission, the two secondary fragments created are subject to the fulfilment of the following equations: $Z_1 + Z_2 = Z_{Cf} = 98$ and $A_1 + A_2 + n = A_{Cf} = 252$, where n is the number of neutrons evaporated in the event prior to the prompt γ-ray cascade. Charge Z and mass A are not shared evenly among the two fragments, leading to the appearance of a lighter mass maximum and a heavier mass maximum in the secondary fragments distribution. Figure 5.1 shows the secondary fragments

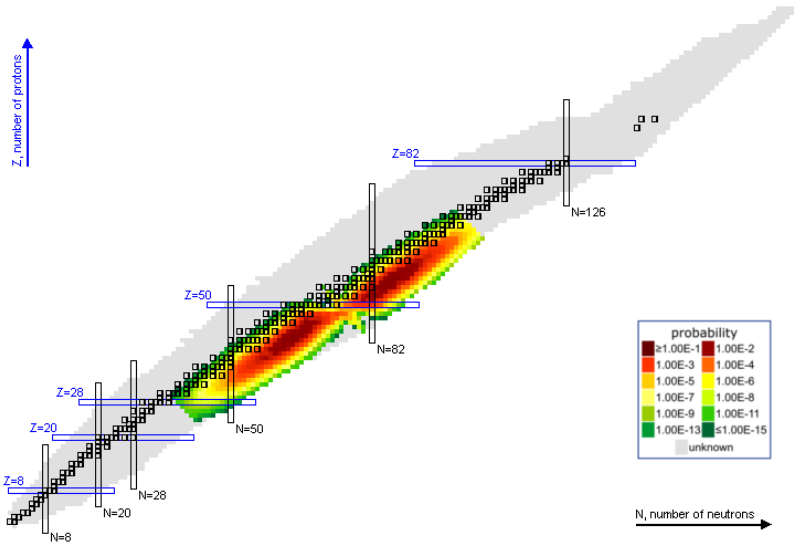

Figure 5.1.: Yield of the secondary fragments of ^{252}Cf spontaneous fission [Nnd].

distribution of ^{252}Cf spontaneous fission in the nuclear chart [Nnd]. The colors used code the fission yield, normalised to unity. The two maxima in the secondary fragments distributions are evident.The usage of a ^{252}Cf spontaneous fission source enabled the access to a set of secondary fragments which are slightly heavier than the ones accessible via neutron-induced ^{235}U fission. In this way, experimental campaigns carried out in ILL [Rég+14] [Ili+16] and this one can be thought to be complementary.

The ^{252}Cf content of the sample used in the experiment was determined by the manufacturer, by material balance calculations to be 183 ng (98.1 μCi) on December 16th, 2011. It was prepared from a purified batch of ^{252}Cf by electrodeposition from an ammonium acetate solution on a platinum disk, and placed inside a custom fabricated plastic source holder that was confirmed to be free of transferable contamination. It is very important, considering the purpose of this work, to point out that the fission fragments were stopped before the γ-radiation emission, thus eliminating Doppler broadening of γ-ray peaks. The source was placed in the focal point of one of the hemispheres of the Gammasphere on December 18th, 2015, where it stayed until January 17th, 2016.

5.2 Data acquisition

The aim of the present work is the measurement of lifetimes of excited states of nuclei with the FATIMA&Gammasphere combined array. However, in addition to these fast timing studies, data for pure spectroscopic analysis were collected in parallel. In order to meet the demand of both purposes, two independent data acquisition systems were used.

5.2.1 Spectroscopic measurements

On one hand, an independent data stream was acquired with the new digital data acquisition system the experiments at the ATLAS beamline have re-instrumented their detectors with [And15]. Each of the **D**igital **G**amma**s**phere (DGS) digitisers, that have a sampling frequency of 100 MSample/s, can internally trigger at the arrival of the signals and calculate their energy [1]. Then, detector's signals, values such as energy, timestamp, and detector number are continuously written to file.

5.2.2 Fast timing measurements

One the other hand, another independent data acquisition system was used for fast timing measurements (figure 5.2).

Trigger

In contrast to the Digital Gammasphere self-triggered readout, the coincidence-structured data acquisition of the fast timing branch of the setup requires the arrival of an external trigger signal that benchmarks the occurrence of a coincidence and allows for the detectors readout. A coincidence, as defined for this particular setup, is subject to the fulfilment of the following requirements:

(i) At least two Gammasphere detectors trigger;

(ii) At least two FATIMA detectors trigger;

(iii) The time difference between the FATIMA detectors signals is smaller than $\Delta\, t \,=\, 200$ ns;

[1] At this stage of the detection, energy calibration has not been performed yet. All references to energy values prior to section 5.3 must be understood as non-calibrated values.

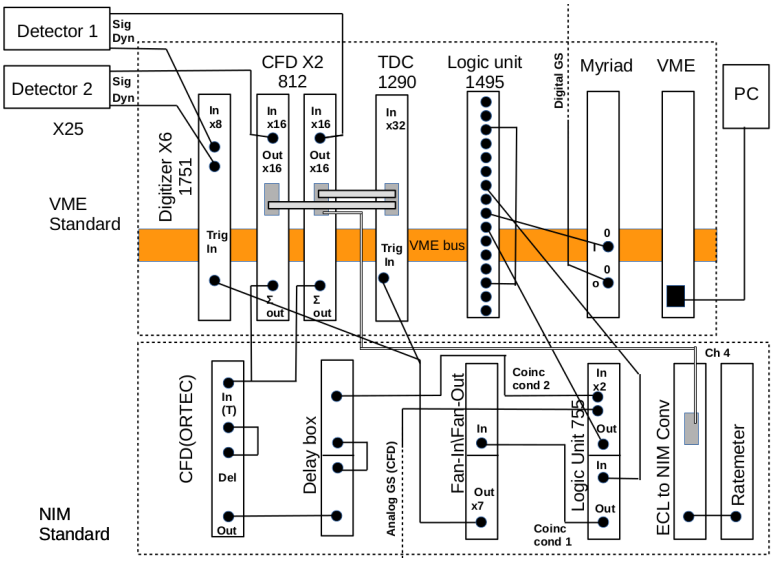

Figure 5.2.: Schematic of the fast timing data acquisition [Gam].

(iv) The time difference between the FATIMA detectors signals and the Gammasphere detectors signals is smaller than $\Delta\, t \;=\; 500$ ns.

The fulfilment of these conditions results in the creation of a trigger signal that is spread to all relevant modules to begin the detector readout. As it can be seen on the top left corner of figure 5.2, two sample FATIMA detectors are depicted. Their anode signals (*Sig* in the figure) feed the 2 constant fraction discriminators V812. One of the features of the V812 modules is that they can provide an output signal *sum_out* equal to the analog sum of the single logic outputs. The proper choice of the single output widths ensures their overlap within the desired time interval. For signal widths of 100 ns, the *sum_out* signal width becomes $\Delta t < 200$ ns and requirement (iii) is fulfilled. The *sum_out* output signal is sent to an additional constant fraction discriminator (bottom, left corner of the figure), whose threshold is such that triggers only for signals generated from more than one FATIMA detector, which ensures the fulfilment of requirement (ii).

The output of the constant fraction discriminator is next sent to the Logic Unit 755, where its coincidence with a 2-fold event from the analog Gammasphere readout (requirement (i)) is manually set to $\Delta T = 500$ ns (requirement (iv)).

The output signal of the Logic Unit 755 fulfils on its own the desired requirements to ensure coincidences between two FATIMA detectors and two Gammasphere detectors. However, it is necessary to check whether the data acquisition system is reading out the previous event, and therefore unable to accept new trigger signals. This is done by sending the output signal of the Logic Unit 755 to the module V1495, that controls the acquisition. In case the system is not busy, the module V1495 sends a common trigger signal back to the Logic Unit 755, that forwards it to the Fan-In/Fan-Out module for its distribution to all relevant modules.

Energy, time, and timestamp pick-off

The precise knowledge of the energy of the detected events, the time difference between them, and the timestamp characteristic of their coincidences is achieved in the electronic modules briefly explained next:

(i) The V1751 is a flash ADC waveform digitiser that houses 8 independent channels. Its sampling frequency is $f_s = 1$ GSample/s [V17b]. In this experiment it is used to acquire signals from the dynodes (*Dyn* in figure 5.2) of the 25 photomultipliers. The arrival of a trigger signal from the module V1495 within a length-adjustable time gate, enables the acquisition of the dynode pulses, and the subsequent extraction of the energy.

(ii) The V1290 is a Multi-Hit/Multi-Event Time to Digital Conversion module that houses 32 independent channels, with a time resolution of 25 ps [V12]. In this experiment, it is used to provide the time difference between the input signals sent by the module V812 within a certain time window, and the common trigger, provided by the module V1495.

(iii) The MyRIAD (Multipurpose gamma Ray Interface to Auxiliary Detectors) module provides an interface to allow external detector systems that work in concert with Digital Gammasphere, such as the FATIMA, to receive and write the timestamp information from Digital Gammasphere and use that for synchronisation [And14].

Fast timing data acquisition control

The V1495 is a programmable logic unit [V14] that controls the data acquisition of the fast timing branch of the experimental setup, as shown in figure 5.3. Upon the

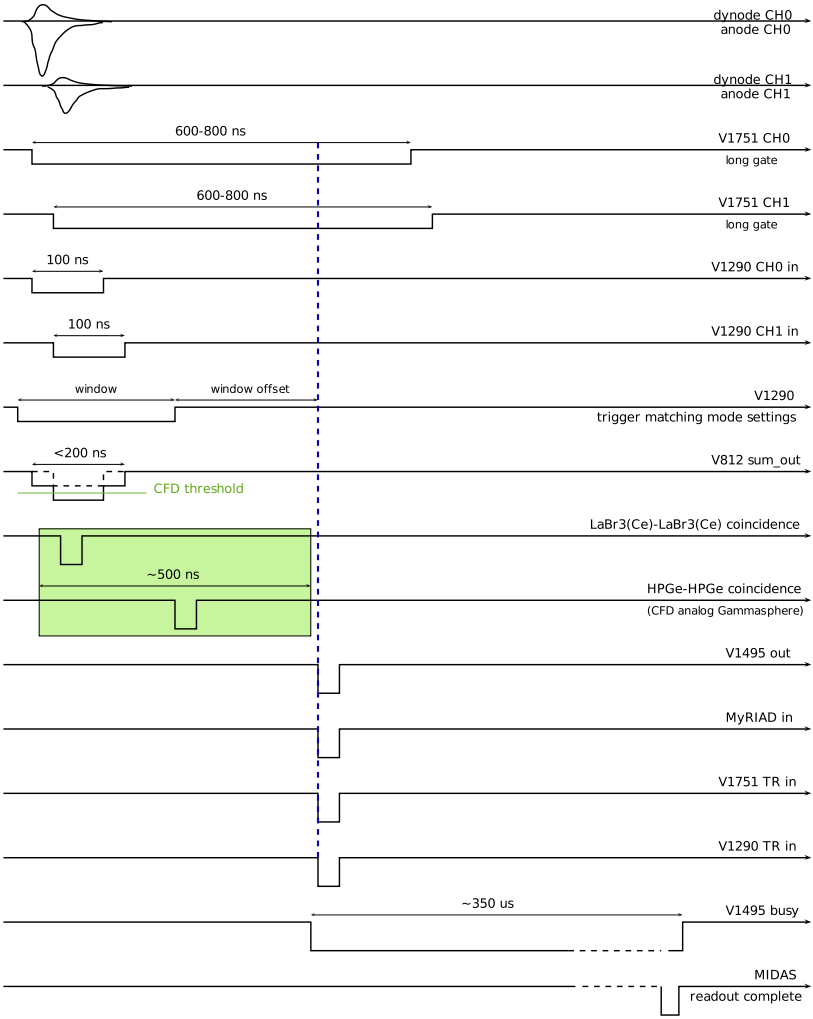

Figure 5.3.: Example of trigger generation and readout. Two coincident signals produced in detectors 0 and 1 are read out.

arrival of a trigger signal from the Logic Unit 755, the state of the module is set to *busy*. If another trigger arrives, it is completely ignored. After the busy status is set, the module creates a trigger output signal that marks the event, and is distributed to the V1751 digitisers and the time-to-digital converter V1290, on one hand, and to the MyRIAD module, on the other hand, as it has been explained above.

After the trigger is produced, the module waits for an adjustable time. This is done to ensure that all data recorded in the modules due to the trigger sent have actually arrived in the output buffer. After this, the V1495 module sets an internal bit to *readout ready*. The data acquisition program in the PC, i.e. the MIDAS data acquisition, continuously checks this register. If it finds it in the readout ready state, it starts the readout procedure. It reads the V1495 module, that provides an event number that is incremented with each accepted trigger, the V1290, the V1751, and the MyRIAD data.

The readout is a very slow process, that introduces a minimum deadtime of, approximately, $t_{dead} = 300\mu s$. The time difference between consecutive FATIMA event timestamps is drawn in figure 5.4. That distribution shows three local maxima, which originate from the different number of V1751 digitisers ready to be read out. As it increases, the average deadtime reaches average values of up to 350 μs, 400 μs, and 500 μs.

When the readout procedure is completed, the data acquisition PC sets the *readout complete* bit on the V1495, which causes a reset procedure on the V1495. Then, the readout complete bit is reset to zero and the module is set to *not busy*. Therefore, the acquisition is ready to accept the next trigger [Rud].

5.2.3 Event sorting

The two independent data acquisition systems explained above produced two independent sets of files. The event sorting consists on the grouping into coincidences of the individual events written in those files for their subsequent analysis.

For spectroscopic studies, only information from the Gammasphere is taken into account. A Gammasphere event is interpreted as a γ ray detection in a single Gammasphere detector; parameters like its energy, its timestamp, its identification number and a flag that informs whether a HPGe detector or a shielding BGO detector fired, are stored in the event.

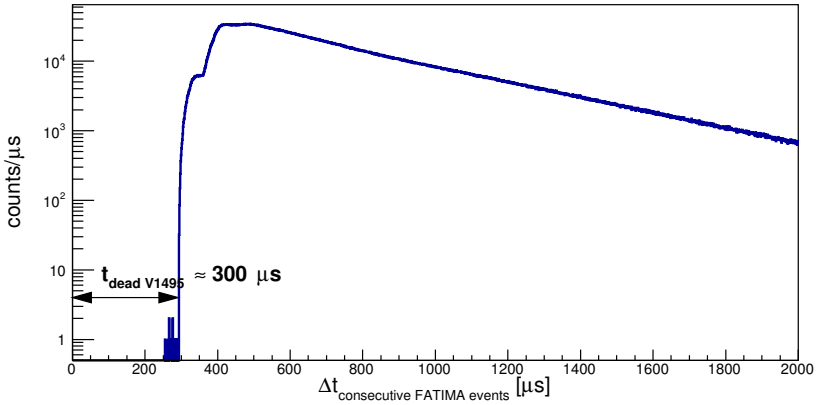

Figure 5.4.: Illustration of the deadtime due to data readout.

Gammasphere detector event
timestamp
energy
ID
HPGe/BGO

This information is used to group all the events whose timestamp difference is smaller than $\Delta T = 10\mu s$ and are generated by HPGe detectors, into coincidences. Next, their energies are calibrated. The set of energy-calibrated, coincident events are finally written into the file called CUBE, that can be used for spectroscopy analysis, with the software package Radware [Rad].

On the contrary, in order to perform fast timing studies, information from both sets of files must be merged into coincidences between the FATIMA and the Gammasphere. There are two kinds of parameters that are stored in the FATIMA files and characterise an event: the ones that are common to the FATIMA coincidence, and the individual attributes of the detectors that fired. Parameters as timestamp (provided by the MyRIAD), event number (provided by the V1495 module) and detector multiplicity are common; detector energy and timestamp (provided by the V1751 digitizers), time difference with respect to the common trigger (provided by the TDC V1290), and detector number are specific for every FATIMA detector.

The following table shows a list of the parameters stored in the Digital Gammasphere files (on the left) and the FATIMA files (on the right) that must be used to build the coincidences:

Gammasphere detector event	**FATIMA event**		
timestamp	timestamp		
energy	event number		
ID	multiplicity (N)		
HPGe/BGO	energy_1	...	energy_N
	timestamp_1	...	timestamp_N
	time_1	...	time_N
	ID_1	...	ID_N

As it can be deduced from previous table, the construction of coincidences is only possible through the comparison of the Gammasphere detectors timestamps and the FATIMA event timestamp, which are synchronised. In order to determine the time intervals in which the coincidences happen, two questions have to be considered. Firstly, the time interval for coincidences between FATIMA and the Gammasphere detectors must be found. Secondly, the coincidence peak among Gammasphere detectors that belong in the same FATIMA event must be found, as well, to minimise background contributions. In order to do so, two distributions have been drawn in figures 5.5a and 5.5b.

From them, the two conditions that the timestamps ts of both arrays must fulfil to be assumed to be in coincidence are extracted [Rud] [Bot]:

(i) $ts_{FATIMA} - ts_{HPGe} \in [-4730ns, -4120ns]$

(ii) $ts_{HPGe_i} - ts_{HPGe_j} \in [-200ns, 0ns]$, $\forall i, j$ in coincidence with one FATIMA timestamp $\ni ts_i > ts_j$.

These limits are shown with dashed lines in figure 5.5. The fulfilment of these conditions is illustrated in figure 5.6.

MyRIAD timestamp corruption

The MyRIAD provides the FATIMA data acquisition system with timestamps which are synchronised with the Digital Gammasphere master clock. Unfortunately, during the experiment there were technical problems, most probably due to the MyRIAD setup, that caused the corruption of the timestamps and therefore the loss of synchronisation between the arrays for a very large number of events.

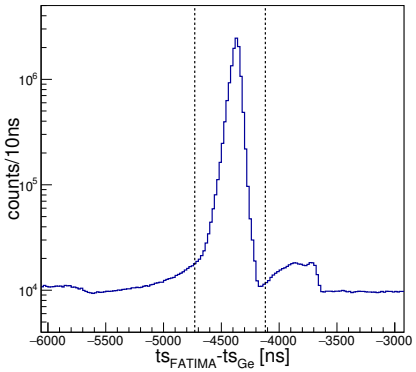

(a) Coincidence peak between FATIMA and the Gammasphere detectors.

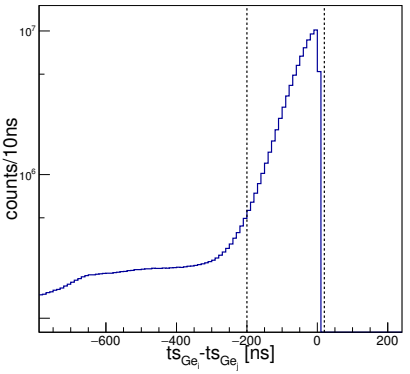

(b) Coincidence peak between pairs of Gammasphere detectors.

Figure 5.5.: Coincidence peaks. See text for details

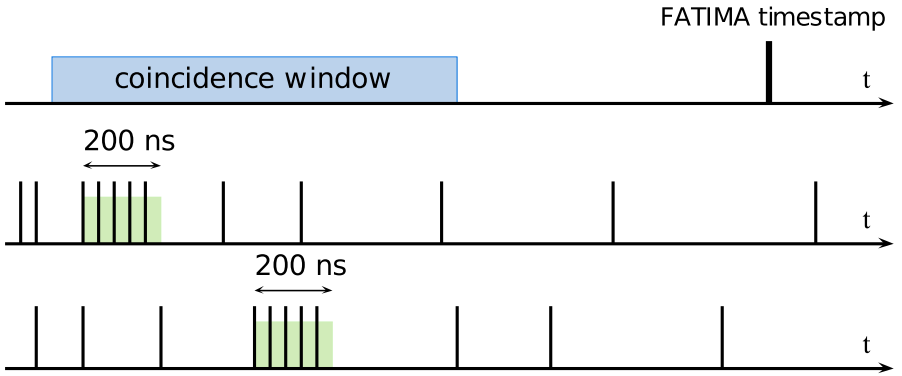

Figure 5.6.: FATIMA and Gammasphere detectors timestamps. Two different possible Gammasphere detectors timestamps are shown for the same FATIMA event. On the green shadow, the Gammasphere events in coincidence with the FATIMA.

However, a partial recovery of the timestamps was possible thanks to the fact that the trigger rate was very stable for both the FATIMA and the Gammasphere, and the existence, for most files, of intervals where the clock values were synchronised for short amounts of time. This allowed to use the timestamps from one of the V1751 digitisers to extrapolate the correct MyRIAD timestamp values [Rud] [Zhu].

5.3 Detector calibration

This section is devoted to the calibration of the array detectors. The Gammasphere array is used to measure the energy of the transitions detected. Therefore, only the energy calibration is needed. However, the FATIMA calibration is more complex, since its detectors must provide reliable values for energy and for timing.

5.3.1 Gammasphere

The Gammasphere calibration measurements were performed after the completion of the experiment, with standard radioactive sources.

In order to overcome the inevitable pole-zero errors that appear in the Gammasphere data set due to the high event rate [Leo87] observed during the whole experiment, a pole-zero calibration is needed. It aims for the characterisation of each of the germanium detectors intrinsic decay time, in order to achieve the baseline and, eventually, signal restoration [And15].

After the signals have been properly recovered, the energy calibration is possible. The correction consists of a first-order polynomial, $\mathscr{P}_1(E)$, that characterises every detector response by its gain and its offset.

Efficiency

A very important property of the detectors is their efficiency, ε, defined as the fraction of particles that enter the volume of the detector that are actually detected. The total efficiency is usually split into two terms: the geometric efficiency and the intrinsic efficiency. The first one accounts for the solid angle covered by the detector from the radiation source; the second one depends on the properties of the detector material and accounts for the probability of interaction between radiation and matter. Figure 5.7 shows the efficiency curve for one hemisphere of the Gammasphere when using the *hevimet* collimators, adapted from reference [Gse]. In order to have an analytical expression, the function 5.1 has been fitted to the curve, yielding the parameters summarised in table 5.1.

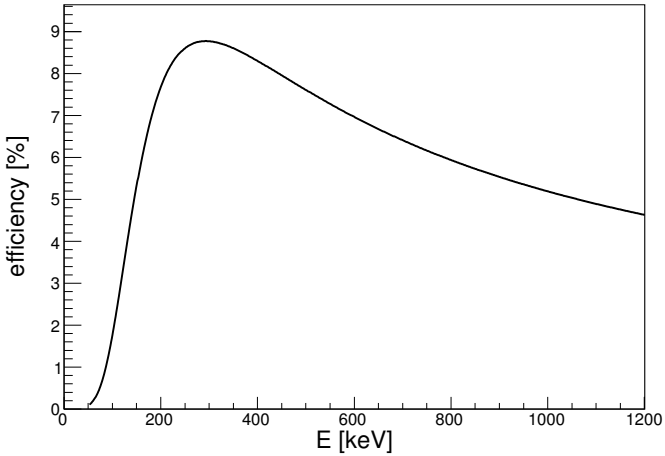

Figure 5.7.: Gammasphere efficiency curve. Adapted from [Gse].

P_1	1.6496(2)
P_2	-0.6026(6)
P_3	-0.096(2)
P_4	-0.010(2)
P_5	-0.1125(6)

Table 5.1.: Gammasphere efficiency curve parameters

$$\varepsilon(E) = e^{P_1+P_2\cdot ln(E)+P_3\cdot[ln(E)]^2+P_4\cdot[ln(E)]^3+P_5\cdot[ln(E)]^4} \tag{5.1}$$

5.3.2 FATIMA

The case of the FATIMA detectors is more complex than the one explained for the Gammasphere array. In addition to the necessity of energy and timing calibrations, the FATIMA is a detector array external to the ATLAS facility; thus no standardised calibration procedure could be followed.

Gain drift correction

Prior to the energy calibration of the $LaBr_3$(Ce) detectors, their gain must be checked for any possible drift over time. This effect has been reported in other experiments involving scintillator crystals coupled to photomultiplier tubes [Ili+16], [Nil10] and it is a consequence of the dependency of the detector signal amplitude on temperature. Besides the obvious possibility of an external change of temperature, internal changes may be caused by, for example, variations in the count rate of the detectors. In the case of this experiment, it is thought that the origin of the gain drift is in the damage endured by the last dynode of the photomultiplier tubes due to the heavy electron bombardment [Gam] [Ham].

Let figure 5.8 serve as an illustration of the gain drift over time and its correction. Uncalibrated energy is represented in the vertical axis, that spans a region equivalent to, approximately, 400 keV $\leq E \leq$ 600 keV. Time is represented in the horizontal axis, being each of the bins a run of the experiment. Since the duration of each run is not constant, the number of counts per bin has been normalised for a better visualisation.

In order to perform the detector gain drift correction, the variation δ_p of the peaks positions p with respect to a reference spectrum must be obtained for each run. Then, a second-order polynomial is used to fit the points $\{p, p + \delta_p\}$:

$$p \mapsto p_{corr} = \mathscr{P}_2(p)$$

The sorting code SOCO [SS17] was used for this purpose, since it automatically achieves the identification of the peaks present in one run through the calculation of its differential spectrum, and performs the polynomial fit. In a few cases the automatic procedure was not successful, due to low statistics and the fits were done manually [Gam].

$LaBr_3$(Ce) detectors energy calibration

Due to the very high statistics, the important amount of γ-rays produced, and the broad energy range covered, the ^{252}Cf spontaneous fission source data have been used to perform the energy calibration of the FATIMA detectors. Once their gain has been corrected for all runs, a single calibration per detector must be obtained. The event-based structure of the data allows for posing different energy gates in the calibrated Gammasphere detectors, to ensure the selection of the coincident, isolated peak in each $LaBr_3$(Ce) detector. Table 5.2 lists the sets of energy gates used

Gate [keV]	Fragment	Detected transitions [keV]
288	^{135}I	1134
297	^{134}Te	1279
352	^{100}Zr	172
		213
400		1220
458	^{140}Xe	377
484	^{138}Xe	241
		423
		482
		589
		688
		730
576	^{110}Ru	241
		423
		483
		511
		705
815	^{96}Sr	978

Table 5.2.: Energies used to calibrate the FATIMA detectors.

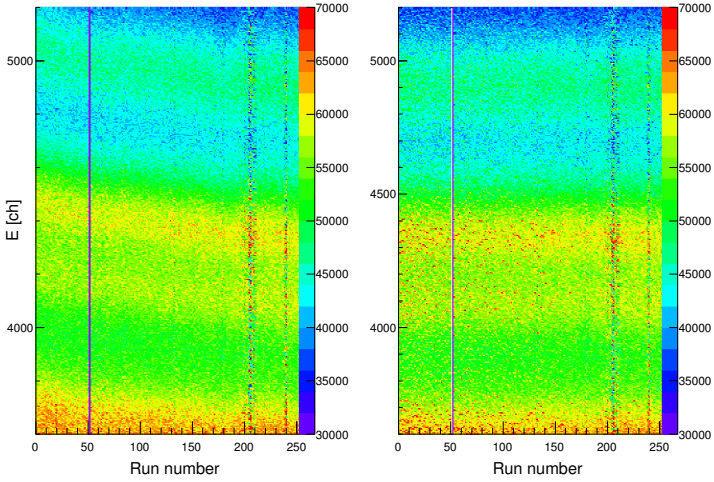

Figure 5.8.: Gain drift correction for detector 15. *Left:* Non corrected spectra. *Right:* Gain-matched spectra with respect to last run.

in Gammasphere, and the coincident transitions detected in the FATIMA, together with the nucleus they are emitted from.

A fourth-order polynomial has been used. Hence,

$$p \mapsto p_{cal} = E = \mathscr{P}_4(p) \tag{5.2}$$

The set of calibration fits is shown in figures from 5.9 to 5.13. For some detectors, a non-monotonic behaviour of $\mathscr{P}_4(p)$ has been observed at energies higher than the relevant energy range for this work, leading to the appearance of values $E_1 = \mathscr{P}_4(p_1) > E_2 = \mathscr{P}_4(p_2)$ for $p_1 < p_2$. To overcome this problem, the calibration is restricted to values $p < p_0$ such that $\mathscr{P}_4(p_0) = 1350$ keV.

FATIMA energy resolution

Once all the FATIMA detectors have been calibrated, a calibration measurement with a ^{166}Ho source allows to perform a energy resolution calibration for the whole array. The function 5.3 has been fitted to the experimental points $p_i = \frac{FWHM_i}{E_i} = \frac{2.355\sigma}{E_i}$, where the σ_i values are extracted from a gaussian fit of the energy peaks.

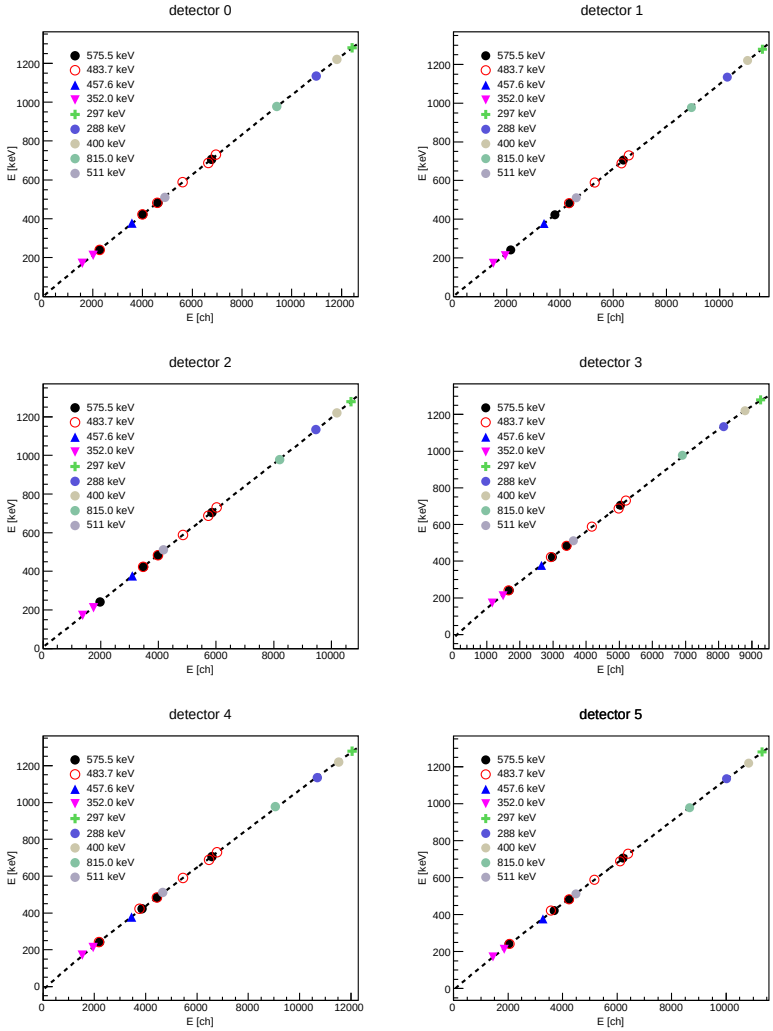
detector 0
detector 1
detector 2
detector 3
detector 4
detector 5
575.5 keV
483.7 keV
457.6 keV
352.0 keV
297 keV
288 keV
400 keV
815.0 keV
511 keV
E [keV]
E [ch]

Figure 5.9.

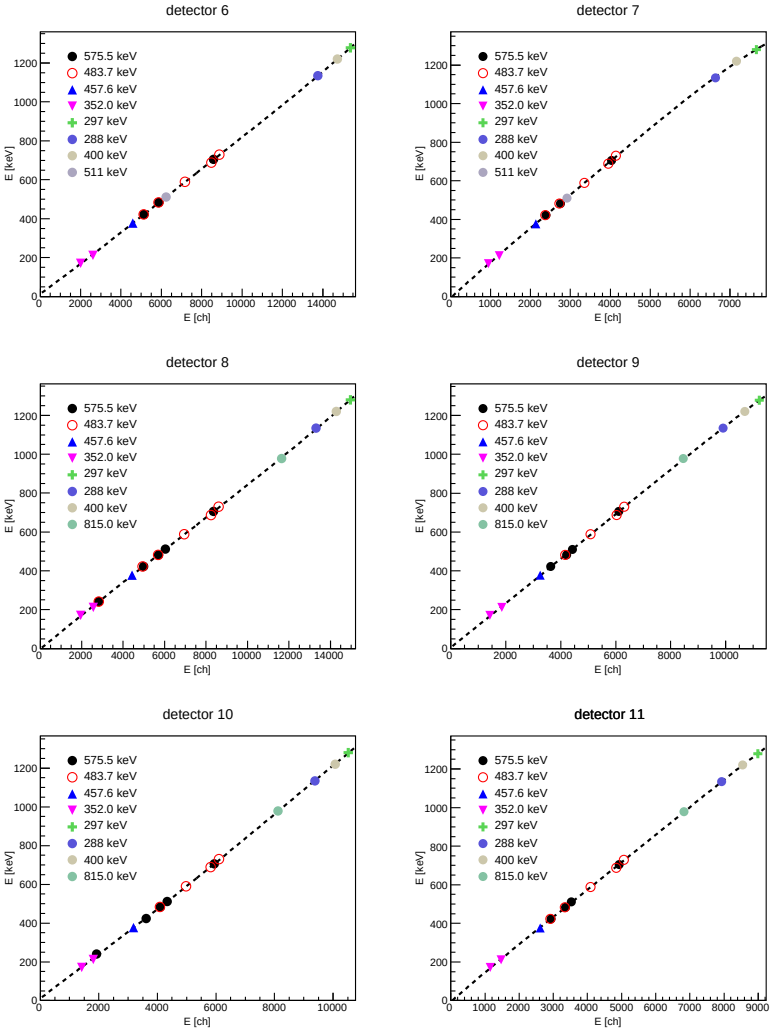
detector 6
detector 7
detector 8
detector 9
detector 10
detector 11
575.5 keV
483.7 keV
457.6 keV
352.0 keV
297 keV
288 keV
400 keV
511 keV
815.0 keV
E [keV]
E [ch]

Figure 5.10.

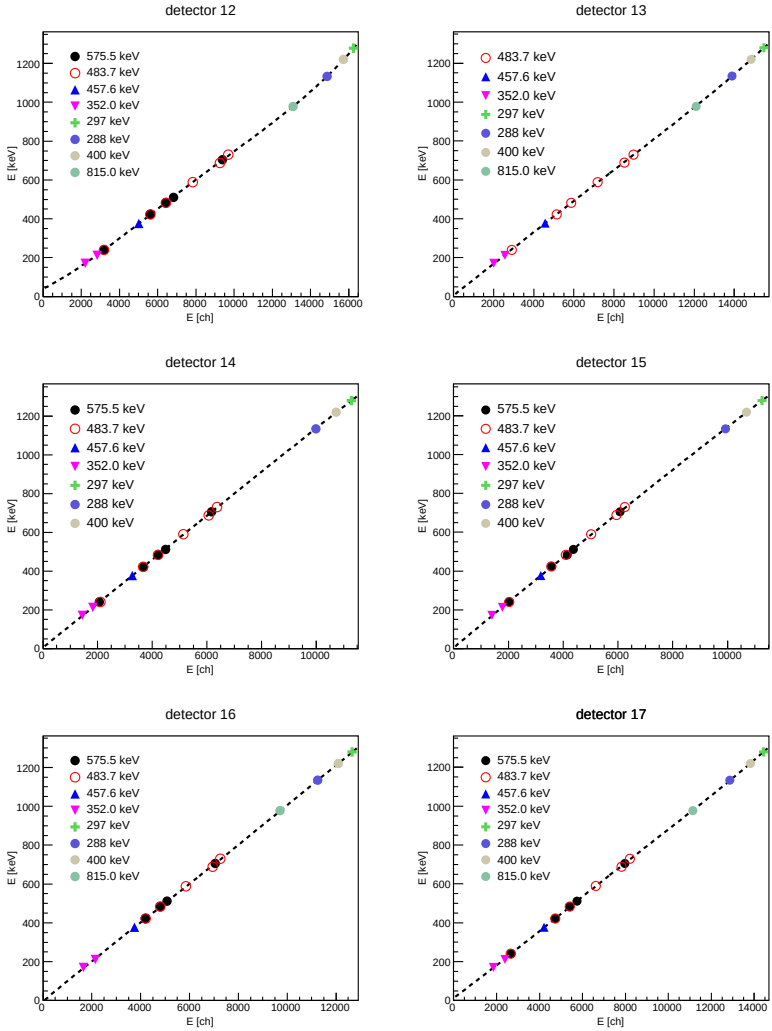
detector 12
detector 13
detector 14
detector 15
detector 16
detector 17
575.5 keV
483.7 keV
457.6 keV
352.0 keV
297 keV
288 keV
400 keV
815.0 keV
E [keV]
E [ch]

Figure 5.11.

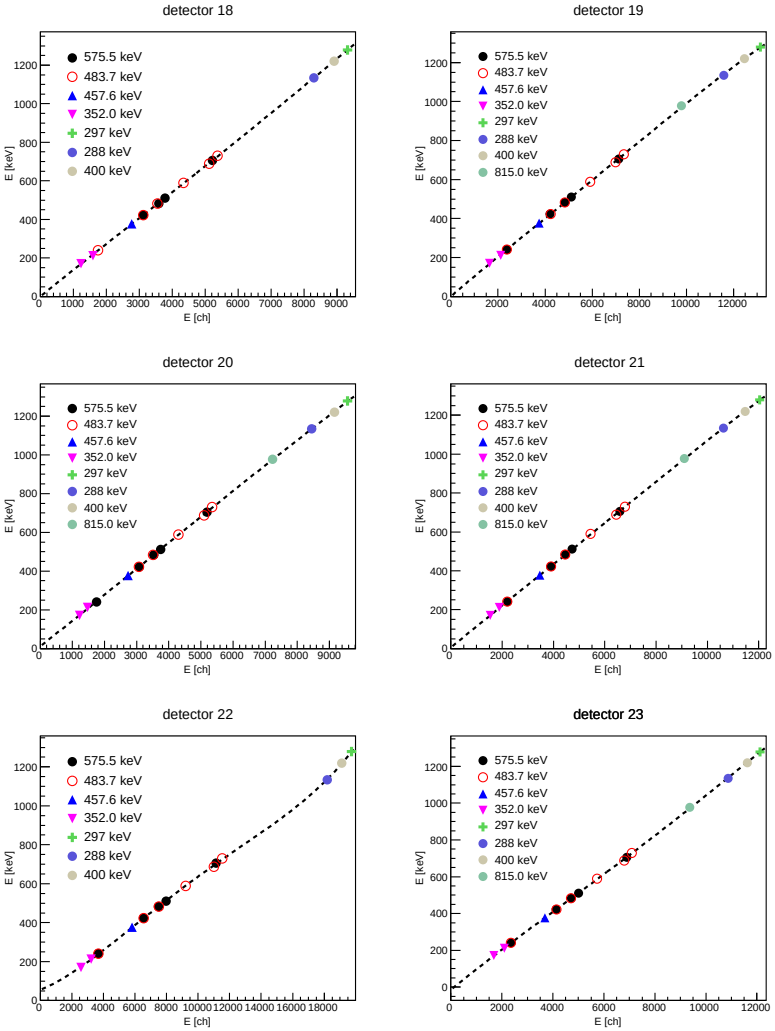
detector 18
detector 19
detector 20
detector 21
detector 22
detector 23
575.5 keV
483.7 keV
457.6 keV
352.0 keV
297 keV
288 keV
400 keV
815.0 keV
E [keV]
E [ch]

Figure 5.12.

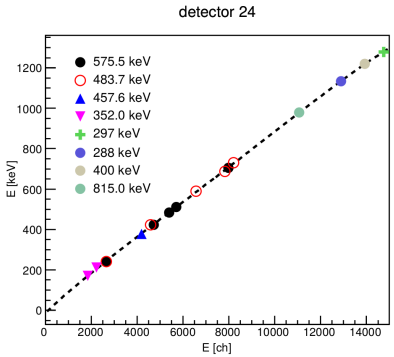

Figure 5.13.

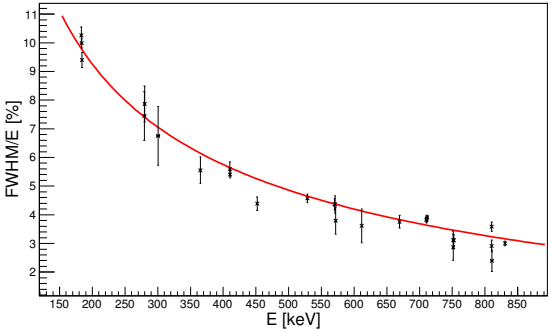

Figure 5.14.: Energy resolution of the FATIMA

$$f(E) = \frac{A}{\sqrt{E}} + B \tag{5.3}$$

A	$169.3(33)\,\sqrt{\text{keV}}$
B	$-2.71(14)$

Table 5.3.: FATIMA energy resolution parameters. They have been obtained from the fit in figure 5.14.

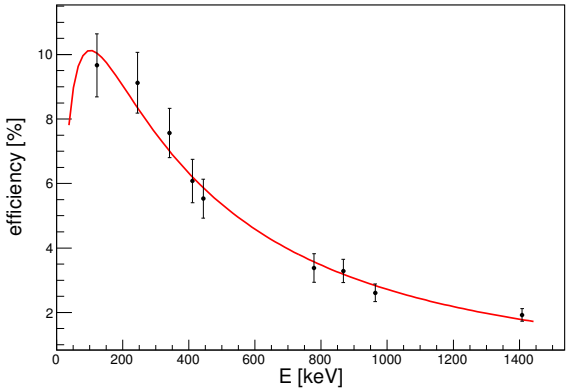

Figure 5.15.: Efficiency curve of the FATIMA [Gam]

P_1	1.00(5)
P_2	−1.2(1)
P_3	−0.25(6)

Table 5.4.: Parameters of the FATIMA efficiency curve. They have been obtained from the fit in figure 5.15.

FATIMA efficiency

As it as been mentioned above, an important parameter of a detector is its efficiency. In order to obtain an absolute efficiency curve for the whole FATIMA, a ^{152}Eu source with well known activity was used [Gam], and the number of detected γ rays in each detector was divided by their expected total number, for the set of energies the source offers. Equation 5.4 has been fitted to the experimental points drawn in figure 5.15. The values of the parameters obtained are summarised in table 5.4.

$$\varepsilon(E) = e^{P_1 + P_2 \cdot ln(E) + P_3 \cdot [ln(E)]^2} \tag{5.4}$$

Timing calibration

As it is explained in section 3.2.2, the precise knowledge of the prompt response difference function, characteristic of the fast timing array is a necessary ingredient for the correct determination of timing using the Generalised Centroid Difference Method. The steps that must be followed to obtain the *PRD* curve with respect to a certain reference transition are [Rég11]:

(i) To choose a transition that depopulates (or populates) a state which is fed by (or decays via) several transitions of energies E_i. That is the reference transition, of energy E_{ref}.

(ii) To pose the necessary number of energy gates in the Gammasphere detectors to ensure clean coincidences in the FATIMA.

(iii) To set i energy gates with values E_i and E_{ref} in the FATIMA detectors.

(iv) To get the i delayed distributions $D_{stop_i}(t)$ for coincidences such that E_i were detected in the *start* detector and E_{ref} was detected in the *stop* detector.

(v) To get the i delayed distributions $D_{start_i}(t)$ for coincidences such that E_i were detected in the *stop* detector and E_{ref} was detected in the *start* detector.

(vi) To calculate the i centroid differences ΔC_i between $D_{stop_i}(t)$ and $D_{start_i}(t)$.

(vii) To calculate the values $PRD(E_i)$ for each E_i, according to equation:

$$PRD(E_i) = \Delta C_i - 2\tau$$

where τ is the lifetime of the state populated (depopulated) by E_i and depopulated (populated) by E_{ref}.

(viii) To use the pairs $\{E_i, PRD(E_i)\}$ to fit the following function:

$$PRD(E) = \frac{A}{\sqrt{B+E}} + \mathscr{P}_n(E) \tag{5.5}$$

where $\mathscr{P}_n(E)$ is a polynomial of n-th order. Note the similarities between the *PRD* function (equation 5.5) and the equation 3.6, that describes the dependency of the detectors time walk with energy in a fast timing setup. The latter one is deduced for detectors that show a linear dependency between the signal amplitude and rise time; the first one accounts for other possible dependencies; hence their difference.

These steps can be repeated as many times as different reference transitions the calibration source offers. Eventually, all the *PRD* curves obtained are combined into a single one.

In this work, two calibration sources have been used: ^{166}Ho and ^{152}Eu. In table 5.5, that lists all γ-rays identified in the calibration source energy spectrum (whose level scheme is draw in figure 5.16), it can be seen that ^{166}Ho offers several possible reference transitions. Among them, the deexcitation of the first 2^+, the 4^+, and 6^+ excited states stand out, since they are fed by many transitions, and their lifetimes are precisely known. However, $2^+ \rightarrow 0^+$ turns out not to be a good choice because the contribution of the background at that energy is very large. A proper combination of sufficiency of statistics and cleanliness of the timing spectra is only achieved when $4^+ \rightarrow 2^+$ and $6^+ \rightarrow 4^+$ are used as reference.

Both reference transitions are γ-rays that depopulate the states; therefore, $D_{stop_i}(t)$ ($D_{start_i}(t)$) corresponds to distributions in which E_{ref} was detected in the *stop* (*start*) detector and the set of feeding transitions of E_i were detected in the *start* (*stop*) detector. From now on, in order to simplify the nomenclature, $D_{stop_i}(t)$ will be referred to as *delayed distribution*, while $D_{start_i}(t)$ will be referred to as *antidelayed distribution*, following [Rég+15] [Ili+16]. The closeness of some of the energies of interest to other contaminant transitions energies, also from the ^{166}Ho deexcitation, made the usage of energy gates in the Gammasphere necessary. A list of the transitions used for each reference transition, as well as the energy gates posed in the Gammasphere detectors can be found in table 5.6.

Figures 5.18 and 5.19 show the delayed (in blue) and antidelayed (in red) distributions obtained for the two sets of energies for reference energies $E_{ref} = 184$ keV and $E_{ref} = 280$ keV, respectively, as well as the centroids and their difference. These centroid differences are used to calculate the values $PRD(E_i)$. It is interesting to point out that, thanks to the mirror symmetry inherent to the method, the following statements are necessarily satisfied:

(i) $PRD_{E_{ref}=184\text{keV}}(184\text{keV}) = 0$

(ii) $PRD_{E_{ref}=280\text{keV}}(280\text{keV}) = 0$

(iii) $PRD_{E_{ref}=280\text{keV}}(184\text{keV}) = -PRD_{E_{ref}=184\text{keV}}(280\text{keV})$

This allows for the inclusion of three additional points to fit equation 5.5, as it is shown in figure 5.20.

In table 5.7 a summary of the parameters obtained for the two curves is given. Parameter C is the slope of the polynomial function in equation 5.5, and D is its offset. The knowledge of the arithmetic expression of the two *PRD* curves and their

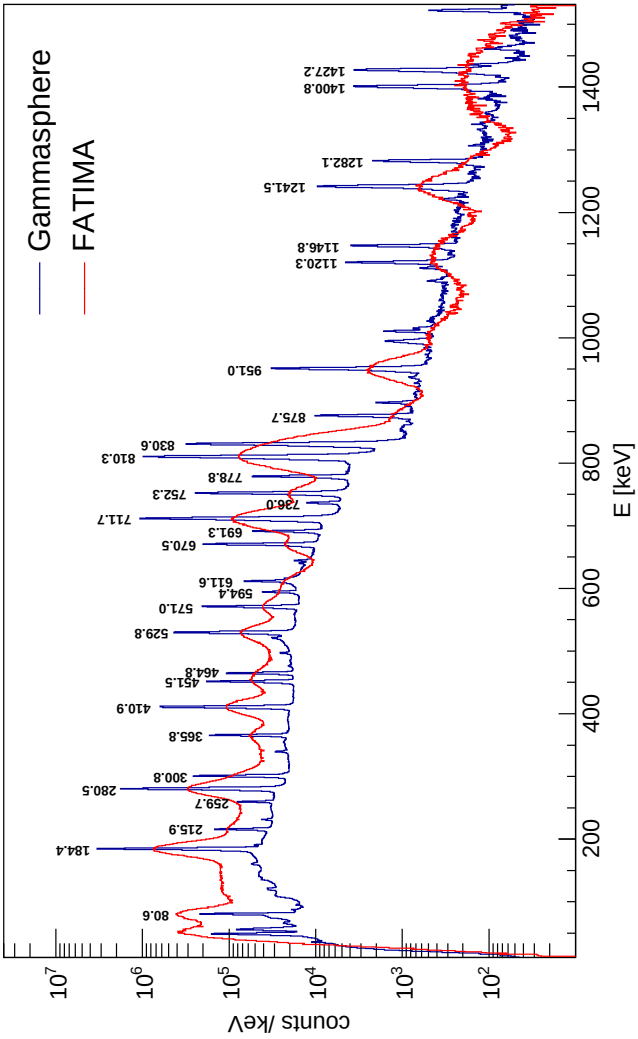

Figure 5.16.: ^{166}**Er spectrum from the deexcitation of a** ^{166}**Ho source.**
All energies are in keV.

E_{level} [keV]	J^{Π}	τ [ps]	E_{γ} [keV]	Final level	
0	0^+	STABLE			
80.5776	2^+	2618	80.576	0	0^+
264.990	4^+	170	184.4113	80.576	2^+
545.454	6^+	22	280.464	264.990	4^+
859.389	3^+	6.5	594.409	264.990	4^+
			778.839	80.576	2^+
911.208	8^+	5.94	365.760	545.454	6^+
956.232	4^+	5.0	691.251	264.990	4^+
			875.650	80.5776	2^+
1075.277	5^+	3.9	215.8887	859.389	3^+
			529.807	545.454	6^+
			810.293	264.990	4^+
1215.968	6^+	6.3	259.740	956.232	4^+
			670.516	545.454	6^+
			950.964	264.990	4^+
1376.035	7^+	7.1	300.755	1075.277	5^+
			464.832	911.208	8^+
			830.585	545.454	6^+
1665.799	$5^{(-)}$		1120.330	545.454	6^+
			1400.770	264.990	4^+
1692.297	5^-		736.02	956.232	4^+
			1146.825	545.454	6^+
			1427.227	264.990	4^+
1786.975	6^-		410.944	1376.035	7^+
			570.976	1215.968	6^+
			711.681	1075.277	5^+
			1241.500	545.454	6^+
1827.557	6^-		451.542	1376.035	7^+
			611.555	1215.968	6^+
			752.313	1075.277	5^+
			1282.058	545.454	6^+

Table 5.5.: List of levels and transitions in ^{166}Er. These γ-rays have been identified in the spectrum shown in figure 5.16. All values are taken from [Nnd].

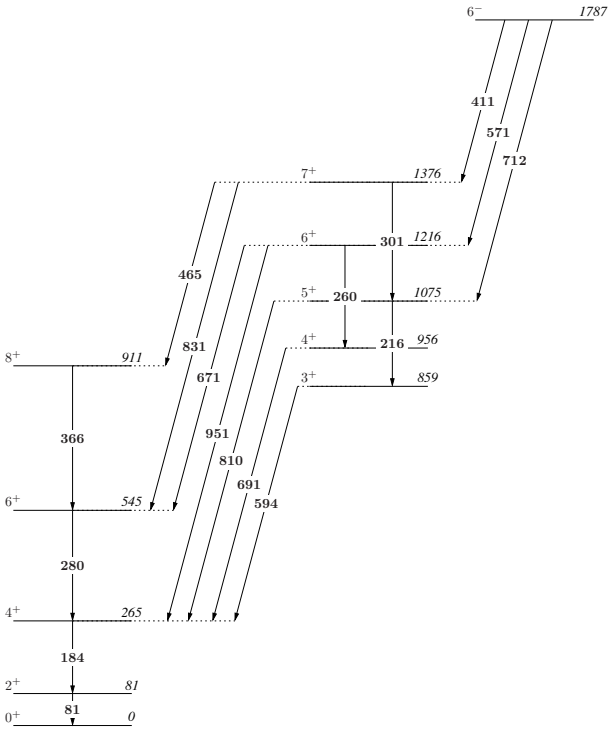

Figure 5.17.: Partial level scheme of ^{166}Er. It shows the transitions used in the PRD calibration. All energies are in keV.

E_{ref} [keV]	E_i [keV]	Gammasphere gates [keV]
184	280	671
	594	216, 712
	691	260
	810	301, 411
	951	571
280	366	465
	671	571
	831	411

Table 5.6.: Transitions used to calibrate the PRD curve. Two energy gates mean the usage of a double energy gate in the Gammasphere.

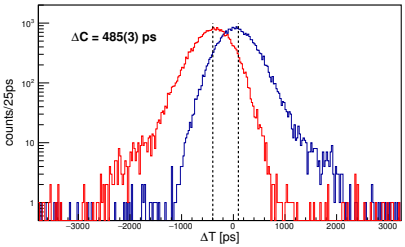

(a) Gate: 280-184 keV

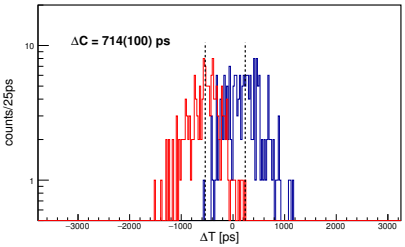

(b) Gate: 594-184 keV

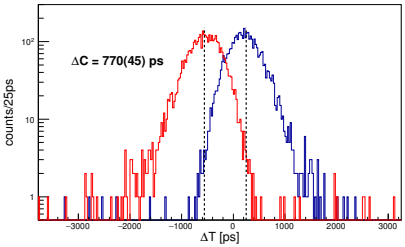

(c) Gate: 691-184 keV

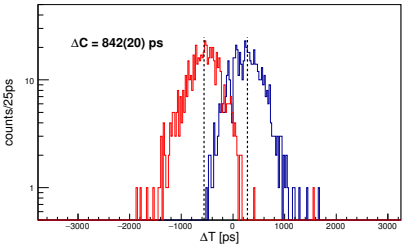

(d) Gate: 810-184 keV

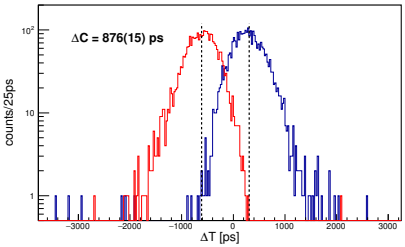

(e) Gate: 951-184 keV

Figure 5.18.: Delayed and antidelayed distributions obtained with E_{ref} = 184 keV

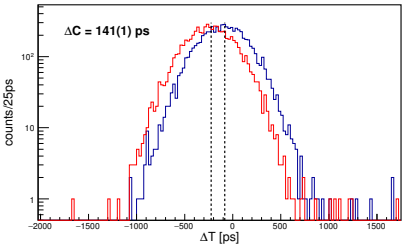

(a) Gate: 366-280 keV

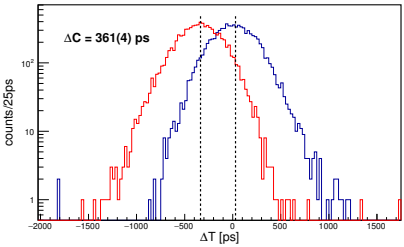

(b) Gate: 671-280 keV

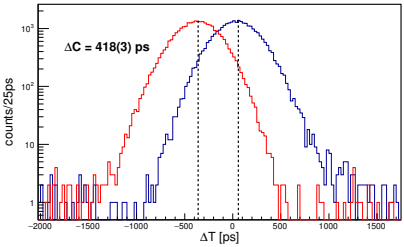

(c) Gate: 831-280 keV

Figure 5.19.: Delayed and antidelayed distributions obtained with E_{ref} = 280 keV

symmetric behaviour permits to shift one of them towards the other to make them overlap:

$$PRD_{E_{ref}=184\text{keV}}(E) \mapsto PRD_{E_{ref}=184\text{keV}}(E) - PRD_{E_{ref}=184\text{keV}}(280)$$

After this operation, a new fit that yields new parameters with smaller relative uncertainties can be performed.

In order to obtain the final expression for $PRD(E)$, the values $\{E_i, PRD(E_i)\}$ derived from a ^{152}Eu calibration source [Gam] have been included. They have been shifted to overlap the ^{166}Ho following the same strategy explained above. Results are shown in figure 5.21 and table 5.8

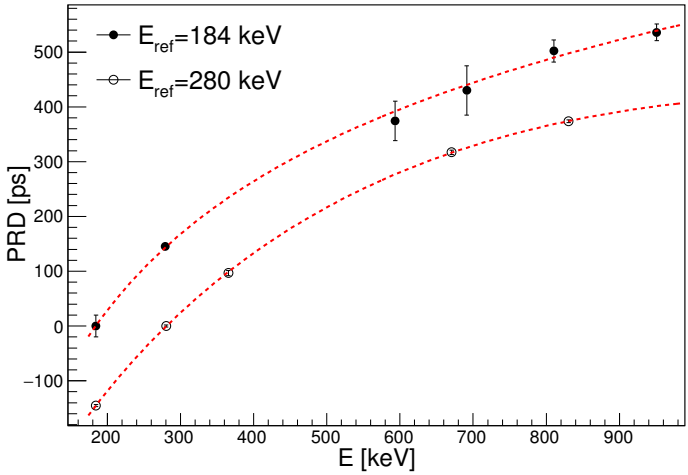

Figure 5.20.: *PRD* curves obtained for two reference energies. Note that the zero-crossing point for each curve corresponds to the reference energy used for the calculation of the points.

	$\mathbf{PRD}_{ref=184\mathbf{keV}}$	$\mathbf{PRD}_{ref=280\mathbf{keV}}$
A [ps$\sqrt{\text{keV}}$]	-15927(21034)	-82342(39073)
B [keV]	87(237)	503(171)
C [ps/keV]	0.087(360)	0.57(28)
D [ps]	951(933)	3101(1157)

Table 5.7.: Result of the fits

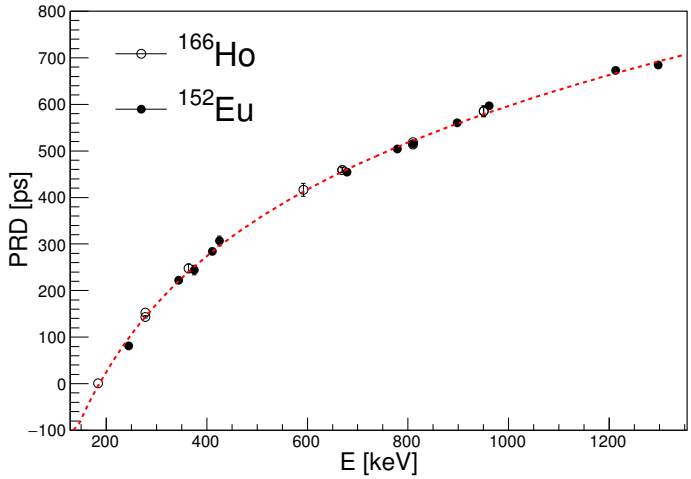

Figure 5.21.: Final *PRD* curve.

A [ps$\sqrt{\text{keV}}$]	-16647(3269)
B [keV]	95.6(444)
C [ps/keV]	0.12735(4091)
D [ps]	973(129)

Table 5.8.: Final *PRD* curve parameters

6 Analysis

In this chapter, the analysis of the data taken with the FATIMA&Gammasphere combined array that led to the determination of the lifetimes of low-lying excited states in the neutron-rich cerium isotopes ^{146}Ce, ^{148}Ce and ^{150}Ce will be explained.

6.1 Fast neutron-induced background suppression

As it has been explained in section 5.2.3, no conditions have been imposed for the time differences between individual hits in the TDC module. Figure 6.1 shows a histogram in which the time difference between all combinations of hits in one event and their energy are plotted. Two different structures arise: firstly, a very intense distribution of events that span the whole energy range, centered around $\Delta T \approx 0$; secondly, a set of events that span the whole energy range, as well, but are not centered around $\Delta T \approx 0$, but are shifted by $|\Delta T_{del}| > 3$ ns with respect to other hits in the same event. These events have been suggested to have their origin in the coincidences between γ rays emitted from the fission fragments and γ rays produced in the FATIMA after the interaction of the fission neutrons with the detector material [Gam].

There are two reasons that support this hypothesis. On one hand, the identification [Kie+15] of several peaks that belong to ^{139}La, ^{79}Br and ^{81}Br in the energy spectrum of events whose $\Delta T > 5$ ns. Among them, the transitions $5/2^+ \rightarrow 7/2^+$ in ^{139}La with an energy of $E = 165.9$ keV, $5/2^- \rightarrow 3/2^-$ in ^{81}Br with an energy of $E = 276.0$ keV, and $5/2^- \rightarrow 3/2^-$ with an energy of $E = 217.1$ keV, $3/2^- \rightarrow 3/2^-$ with an energy of $E = 261.3$ keV and $1/2^- \rightarrow 3/2^-$ with an energy of $E = 306.5$ keV in ^{79}Br stand out (figure 6.2), implying that the most relevant interaction is the inelastic scattering of fast neutrons on the nuclei of $LaBr_3$(Ce). On the other hand, the shape of the timing distribution approximately reveals the time passed since the neutron emission until their interaction with the detectors. Taking into account that the distance between the focal plane of the Gammasphere, where the ^{252}Cf was placed and the FATIMA is $d \approx 13.4$ cm and that the average neutron energy in the spontaneous fission of ^{252}Cf is $E \approx 2$ MeV [Abb+03], this time can be calculated to be $t \approx 6.5$ ns, in good agreement with the time spectrum shown in figure 6.3.

In order to make the FATIMA energy spectra as clean as possible for the fast timing analysis, all events whose $\Delta T > 3$ ns have been discarded.

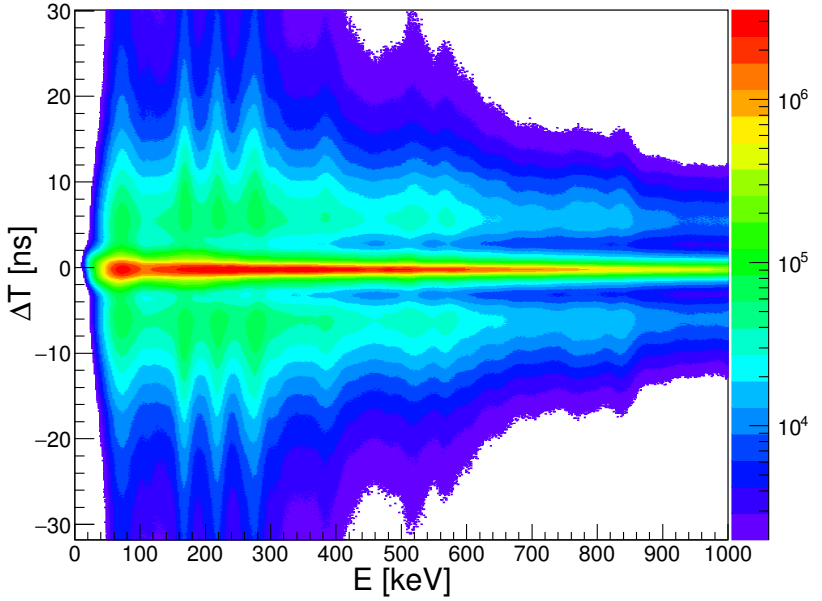

Figure 6.1.: Histogram of the time difference between hits in FATIMA detectors and their energy

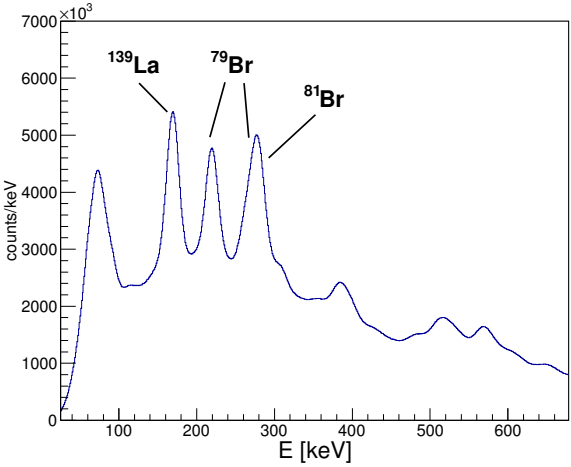

Figure 6.2.: Energy spectrum of events whose $\Delta T > 3$ ns.

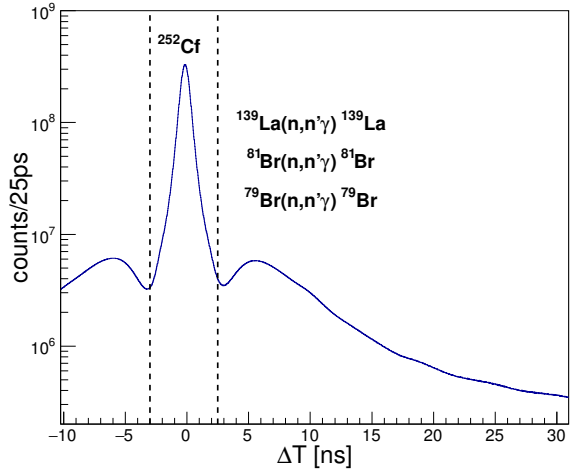

Figure 6.3.: Timing distribution: two regions can be separated.

6.2 Analysis of the timing distributions

The timing distributions are, in general, obtained by the subtraction of all possible different combinations of time values stored in every FATIMA event, $t_j - t_i$, $\forall\ i, j \ni ID_i < ID_j$. This latter condition is required to avoid double-counting. For instance, a coincidence in which 4 FATIMA detectors trigger (multiplicity 4) yields a total amount of $\frac{4\cdot(4-1)}{2} = 6$ different combinations of t_i and t_j without repetition, therefore 6 different values of ΔT.

In order to obtain the timing distributions for a particular excited state with characteristic transitions of energy E_f and E_d, one of them must be chosen as time-walk reference, E_{ref}. The other transition is referred to as E. Next, only times t_{ref} and t whose associated energies are E_{ref} and E are considered to obtain the delayed distribution $D(t)$ ($\Delta T = t - t_{ref}$) and the antidelayed distribution $A(t)$ ($\Delta T = t_{ref} - t$). This is the way to build *energy-gated* timing distributions, that characterise a certain excited state. The similarities between these steps and the ones followed in section 5.3 to perform the timing calibration of the setup are obvious.

The centroids of these energy-gated timing distributions are calculated easily using the following formulas:

$$C^D =< t_D >= \frac{\int_{-\infty}^{\infty} tD(t)dt}{\int_{-\infty}^{\infty} D(t)dt} \tag{6.1}$$

$$C^A =< t_A >= \frac{\int_{-\infty}^{\infty} tA(t)dt}{\int_{-\infty}^{\infty} A(t)dt} \tag{6.2}$$

where C^D stands for the delayed distribution centroid and C^A, for the antidelayed distribution centroid. Their uncertainty is given by $\sigma_C = \sqrt{< t^2 > - < t >^2}$. In practice, the integration limits in formulas 6.1 and 6.2 must be carefully chosen to span only the width of the timing distributions, and avoid background contributions. Therefore they become:

$$C^D =< t_D >= \frac{\int_a^b tD(t)dt}{\int_a^b D(t)dt}$$

$$C^A =< t_A >= \frac{\int_a^b tA(t)dt}{\int_a^b A(t)dt}$$

where a and b are symmetric with respect to the point $\frac{C^D+C^A}{2}$. In figure 6.4 two arbitrary timing distributions are drawn. The point $\frac{C^D+C^A}{2}$ is marked with a vertical line, and the dependency of ΔC on the upper integration limit is represented with the red line. For small $b-a$, ΔC shows an increasing, monotonic behaviour as $b-a$ increases. Beyond the range the timing distributions span, ΔC becomes stable. This is the expected dependency for sufficiently clean timing spectra; however, this asymptotic behaviour is not exhibited if there is a non-negligible amount of background. In that case $\Delta C(a,b)$ gets quickly distorted for $b-a$ greater than the combined width of the timing distributions. Therefore, a and b must be carefully chosen for every pair of timing distributions to include only $D(t)$ and $A(t)$.

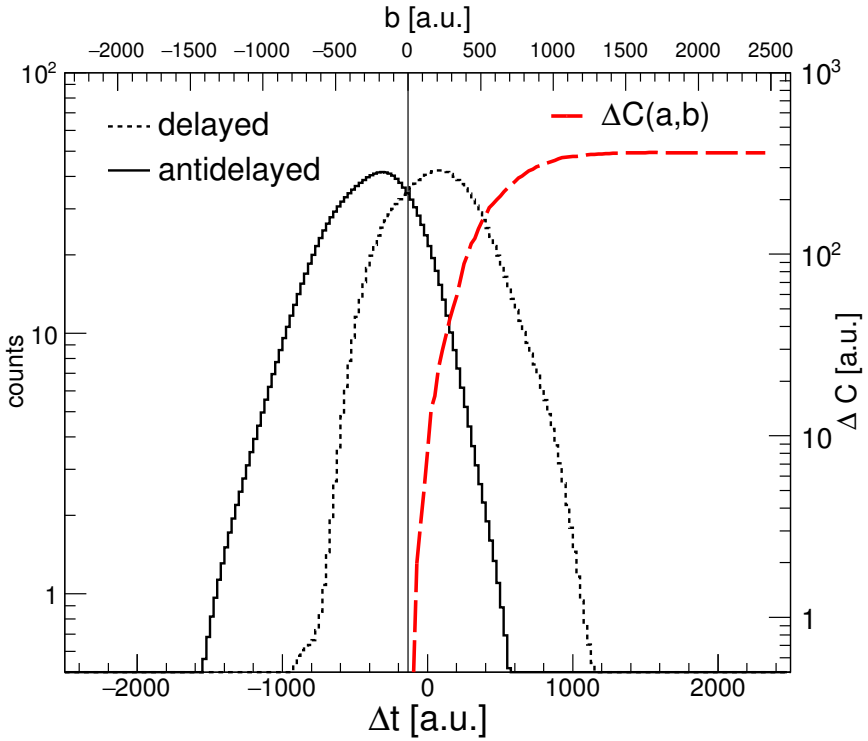

Figure 6.4.: Dependency of ΔC on the integration limits.

Despite the effort made to avoid background contributions to the delayed and antidelayed distributions that affect the determination of ΔC, the timing distribu-

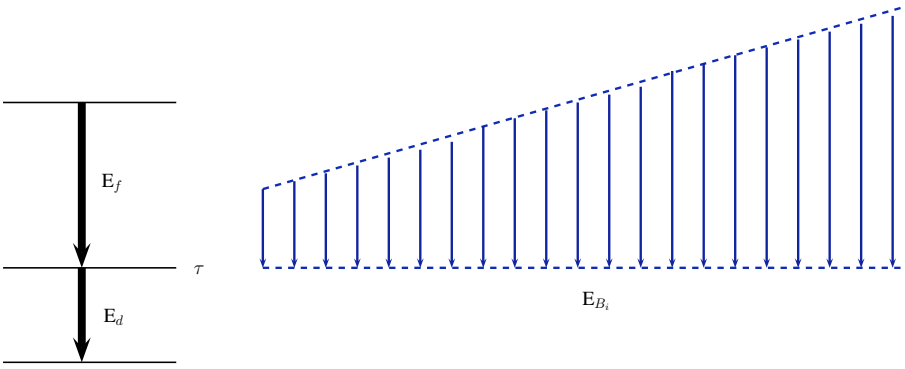

Figure 6.5.: Two possible kinds of coincidences detected in the FATIMA detectors. *Left:* True coincidences between transitions that populate and depopulate the state. *Right:* Random coincidences between a set of transitions unrelated to the deexcitation process, of energies $E_{B_i} \approx E_f$, and the transition that depopulates the state.

tions obtained experimentally are always a superposition of the timing distributions of true coincidences, and the timing distributions of random coincidences unrelated to the deexcitation process. To illustrate how the disentanglement of these two contributions is achieved, let us consider a cascade that involves a state connected by two transitions of energy E_f and E_d.

For the sake of simplicity, the decay transition, E_d, is arbitrarily chosen to serve as time-walk reference transition. Therefore the set of transitions in coincidence with it is formed by those ones of energy E_f originated from the population of the state, or *true* coincidences (figure 6.5, left), and those ones which are randomly detected, or *random* coincidences (figure 6.5, right), that span a broad energy range around E_f and constitute the background continuum. The resulting energy distribution for transitions in coincidence with E_d is drawn in figure 6.6.

In figure 6.7 the centroid difference dependency on energy can be seen for these two contributions: the dashed line represents the prompt response difference; the background centroid difference is drawn in blue and it appears shifted at a certain distance from the *PRD*; finally, the true centroid difference is shifted by an additional ΔC_T with respect to its underlying background, ΔC_B. From this illustration it is clear that the measured centroid difference ΔC, which is the only one experimentally accessible, can be modeled as a linear combination of true centroid differences ΔC_T, and background centroid differences ΔC_B:

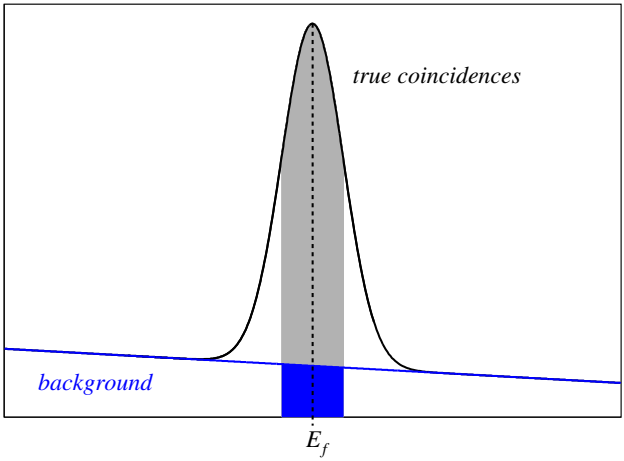

Figure 6.6.: Energy spectrum of transitions in coincidence with the reference transition, of energy E_d.

$$\Delta C = \frac{P}{P+B}\Delta C_T + \frac{B}{P+B}\Delta C_B \tag{6.3}$$

Dividing equation 6.3 by B and solving for ΔC_T yields:

$$\Delta C_T = \Delta C + \frac{\Delta C - \Delta C_B}{\Pi} \tag{6.4}$$

where P and B are the number of true and background centroids, respectively, and $\Pi = \frac{P}{B}$.

Therefore, the calculation of ΔC_T is subject not only to the measurement of ΔC, but also to the extraction of ΔC_B and Π from the experimental data.

On one hand, a function that describes the dependency of ΔC_B on energy must be fitted to a set of points $\{\Delta C_{B_i}, E_i\}$ measured with the same reference transition gate at E_d. This allows for the extraction of $\Delta C_B(E;\beta_1 ... \beta_n)$, where $\{\beta_1 ... \beta_n\}$ are fitting parameters, and the eventual interpolation of $\Delta C_B(E_f)$. The uncertainty of $\Delta C_B(E_f)$ is given by:

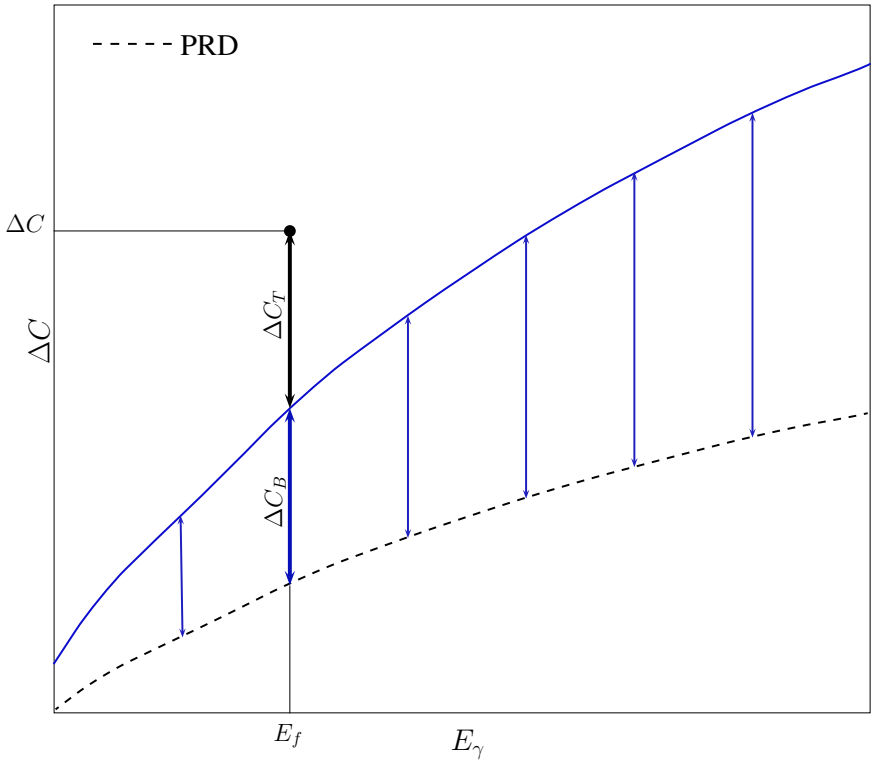

Figure 6.7.: ΔC

$$\sigma^2_{\Delta C_B} = \begin{pmatrix} \frac{\partial \Delta C_B(E_f;\beta_1...\beta_n)}{\partial \beta_1} ... \frac{\partial \Delta C_B(E_f;\beta_1...\beta_n)}{\partial \beta_n} \end{pmatrix} \Sigma \begin{pmatrix} \frac{\partial \Delta C_B(E_f;\beta_1...\beta_n)}{\partial \beta_1} \\ ... \\ \frac{\partial \Delta C_B(E_f;\beta_1...\beta_n)}{\partial \beta_n} \end{pmatrix} \tag{6.5}$$

where Σ is the covariance matrix of $\{\beta_1...\beta_n\}$.

On the other hand, Π is extracted from the energy spectrum of the transitions in coincidence with E_d, like the one drawn in figure 6.6. The peak-to-background ratio is given by:

$$\Pi(\beta_1...\beta_n) = \frac{\int_{E_f-\sigma_E}^{E_f+\sigma_E} p(E;\beta_1...\beta_k)dE}{\int_{E_f-\sigma_E}^{E_f+\sigma_E} b(E;\beta_{k+1}...\beta_n)dE} \tag{6.6}$$

where $p(E;\beta_1...\beta_k)$ and $b(E;\beta_{k+1}...\beta_n)$ are the analytical functions fitted to the energy spectrum $S(E)$, such that $S = p + b$. p is always a gaussian function, whose fitting parameters are constrained by the energy E_f of the transition, and by the FATIMA resolution at E_f (equation 5.3), whereas b is a n-th order polynomial that may include additional gaussian functions if other peaks are nearby. The value of the peak-to-background uncertainty σ_Π is given by the same equation as 6.7:

$$\sigma^2_{\Pi} = \begin{pmatrix} \frac{\partial \Pi(\beta_1...\beta_n)}{\partial \beta_1} ... \frac{\partial \Pi(\beta_1...\beta_n)}{\partial \beta_n} \end{pmatrix} \Sigma \begin{pmatrix} \frac{\partial \Pi(\beta_1...\beta_n)}{\partial \beta_1} \\ ... \\ \frac{\partial \Pi(\beta_1...\beta_n)}{\partial \beta_n} \end{pmatrix} \tag{6.7}$$

6.3 Summation of timing distributions

In section 6.2 it was shown how to calculate the lifetime of any excited state from measured values of ΔC, ΔC_B and Π, under the assumption that the detection of coincidences in the FATIMA yields sufficiently clean energy and timing spectra. However, in the case of a fission experiment like the one analysed in this work, this assumption is no longer valid, due to the presence of many different excited fission fragments that emit a large amount of γ rays. For this reason, two additional energy gates are required in the Gammasphere detectors.

The construction of timing distribution is therefore subject to the detection of two transitions in the FATIMA and two additional transitions in the Gammasphere. A new problem arises at this point, associated to the statistics: as the number

of energy gates increases, the probability of detecting coincidences that fulfil all of them decreases, making the statistics lower. A way to improve them taking advantage of the large number of HPGe detectors in the Gammasphere array has been used.

Let M_{Gs} be the total number of γ-rays detected in the Gammasphere, usually referred to as *multiplicity*. Assuming no background contributions, each of those γ rays of energy E_i, $i = 1...M_{Gs}$, is characteristic of the fission event. Then, every combination without repetitions of 2 elements, $\{E_i, E_j\}$, in that set of M_{Gs} elements is characteristic of the fission event, too.

Due to the constraints on charge and mass of the ^{252}Cf spontaneous fission fragments, the emission of cerium nuclei implies the emission of coincident zirconium fission partners. Therefore, a cerium nucleus can be identified by the detection of not only its characteristic decay cascades, but also by the decay cascades in the correlated zirconium isotopes. Table 6.1 summarises the fission yields for correlated fragments of cerium and zirconium.

	^{144}Ce	^{146}Ce	^{147}Ce	^{148}Ce	^{149}Ce	^{150}Ce
^{98}Zr		0.04(2)	0.02(2)	0.07(2)	0.08(4)	0.17(4)
^{99}Zr		0.04(4)		0.13(4)	0.26(14)	0.13(5)
^{100}Zr		0.11(3)	0.29(8)	0.63(5)	0.25(14)	0.29(5)
^{101}Zr	0.04(3)	0.47(9)	0.63(21)	0.62(16)	0.16(12)	0.06(3)
^{102}Zr	0.02(2)	0.41(5)	0.52(10)	0.44(5)	0.05(5)	0.03(3)
^{103}Zr	0.05(6)	0.15(5)	0.16(1)	0.12(5)		
^{104}Zr		0.07(3)		0.05(5)		

Table 6.1.: Yields of correlated fragment pairs in percent, taken from reference [TA+97]

Thus, the strategy to improve statistics consists of summing up energy and timing spectra detected in FATIMA only if at least one pair of coincident transitions detected in the Gammasphere fulfil the following requirements:

(i) Both transitions belong to a cascade in cerium, or one of the transitions belongs to cerium and the other, to one of the zirconium fission partners.

(ii) The double gate at the aforementioned pair of energies results in the detection of clean, isolated transitions of energy E_f and E_d in the FATIMA. The isolation of the peaks is constrained by the FATIMA energy resolution, which is, in that region, of $FWHM \approx 20$ keV.

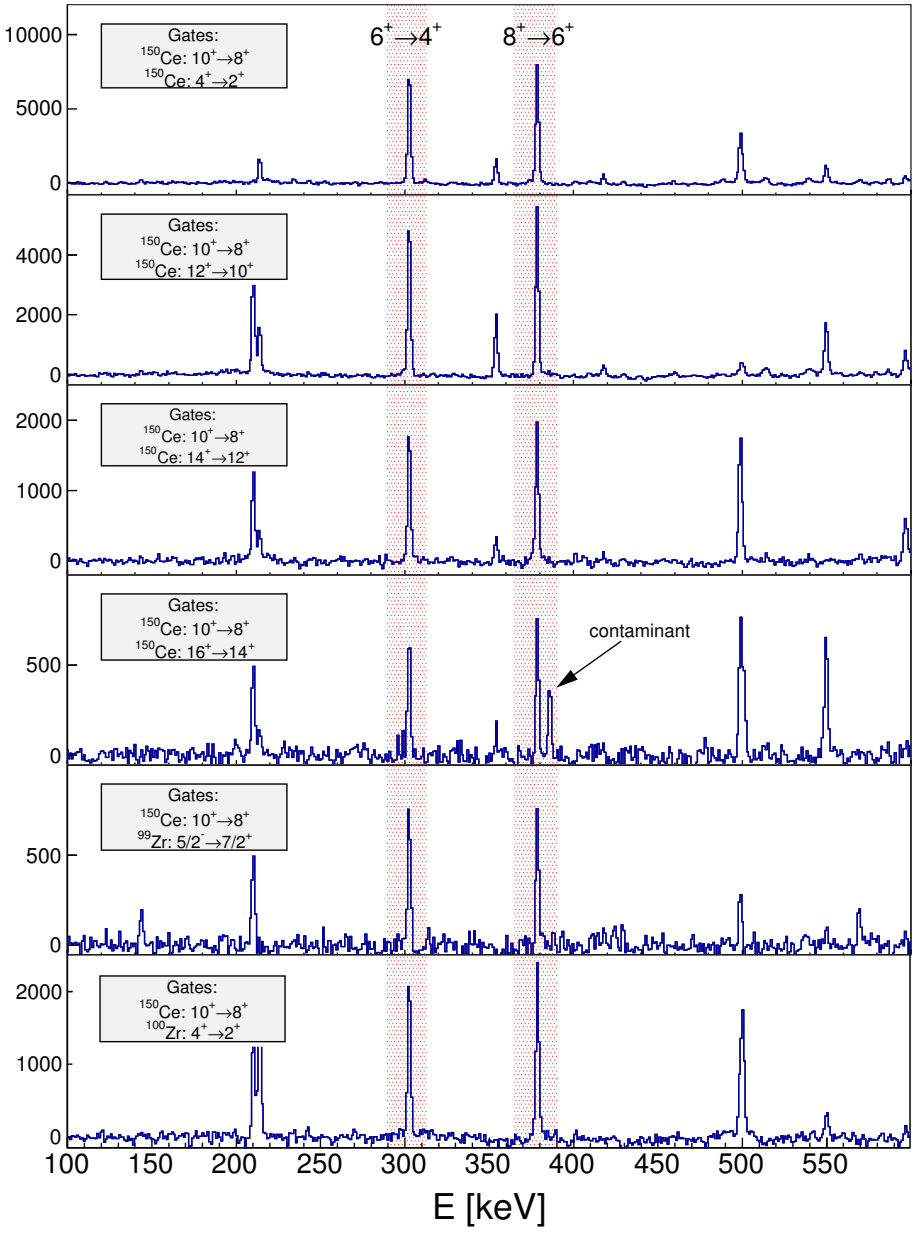

Figure 6.8.: Double-gated energy spectra to select the 6^+ state in ^{150}Ce.

In order to obtain the set of appropriate energy gates, all possible combinations of transitions in the cerium isotopes and their corresponding fission partners have been checked prior to the fast timing analysis. For this task, only data taken for spectroscopic purposes have been analysed using the software package Radware [Rad], suitable for Gammasphere coincidences analysis.

In figure 6.8, an example of double-gated energy spectra detected in the Gammasphere is depicted. In particular, these gates aim to select the 6^+ excited state of ^{150}Ce, characterised by the transitions that populate and depopulate it, of $E_f = 376$ keV and $E_d = 300$ keV, respectively. In the first three cases, the energy gates have been posed in transitions that belong to ^{150}Ce, and result in the spectra where E_f and E_d are sufficiently populated and isolated. The detection of its fission partners ^{99}Zr ($E = 415$ keV, $E = 546$ keV) and ^{100}Zr ($E = 213$ keV, $E = 352$ keV) is unavoidable. The fourth spectrum is given as an example of a double gate which is not appropriate (and therefore not considered) to achieve clean energy and timing FATIMA spectra. Although the superior energy resolution of the Gammasphere allows for the separation of the peak at E_f from the one at a slightly higher energy, these peaks are not distinguishable for the FATIMA. Finally, the two spectra in the bottom are obtained after posing one gate in a characteristic cerium transition and the other gate in a transition of ^{99}Zr (fifth spectrum) and ^{100}Zr (sixth spectrum). It is interesting to point out the convenience of using gates in fission partners to prevent their transitions to contaminate the spectra. In the case of the sixth spectrum, the two energies that the gates have been posed on are $E = 440$ keV and $E = 352$ keV, being the latter a transition between states of ^{100}Zr. Obviously, the peak at $E = 352$ keV visible on the first four spectra vanishes. Furthermore, this peak at $E = 352$ keV also vanishes when the gates are posed on energies characteristic of other fission fragments, as ^{99}Zr, like in the fifth spectrum.

6.4 Energy level schemes

In this section the level schemes of the even-even $^{146-150}$Ce and their fission partners $^{98-102}$Zr including all transitions between states populated in the spontaneous fission of ^{252}Cf [Nnd] are plotted. All energies shown are in keV.

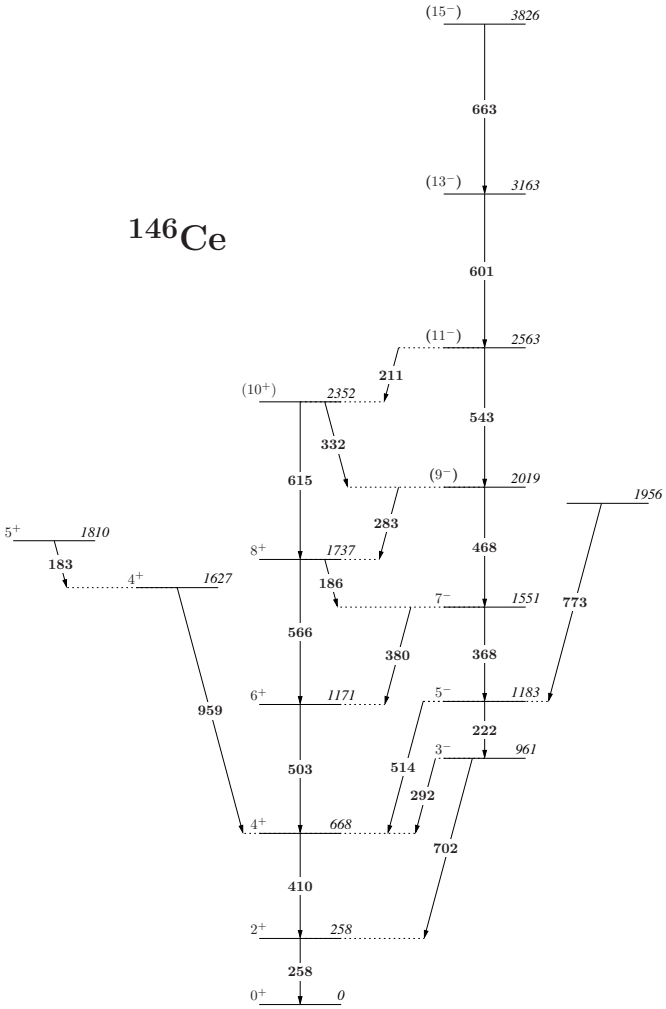
146Ce
(15−) 3826
663
(13−) 3163
601
(11−) 2563
211
(10+) 2352
543
332
615
(9−) 2019
1956
283
5+ 1810
8+ 1737
468
183
4+ 1627
186
7− 1551
773
566
380
368
6+ 1171
5− 1183
959
222
3− 961
503
514
292
4+ 668
702
410
2+ 258
258
0+ 0

Figure 6.9.

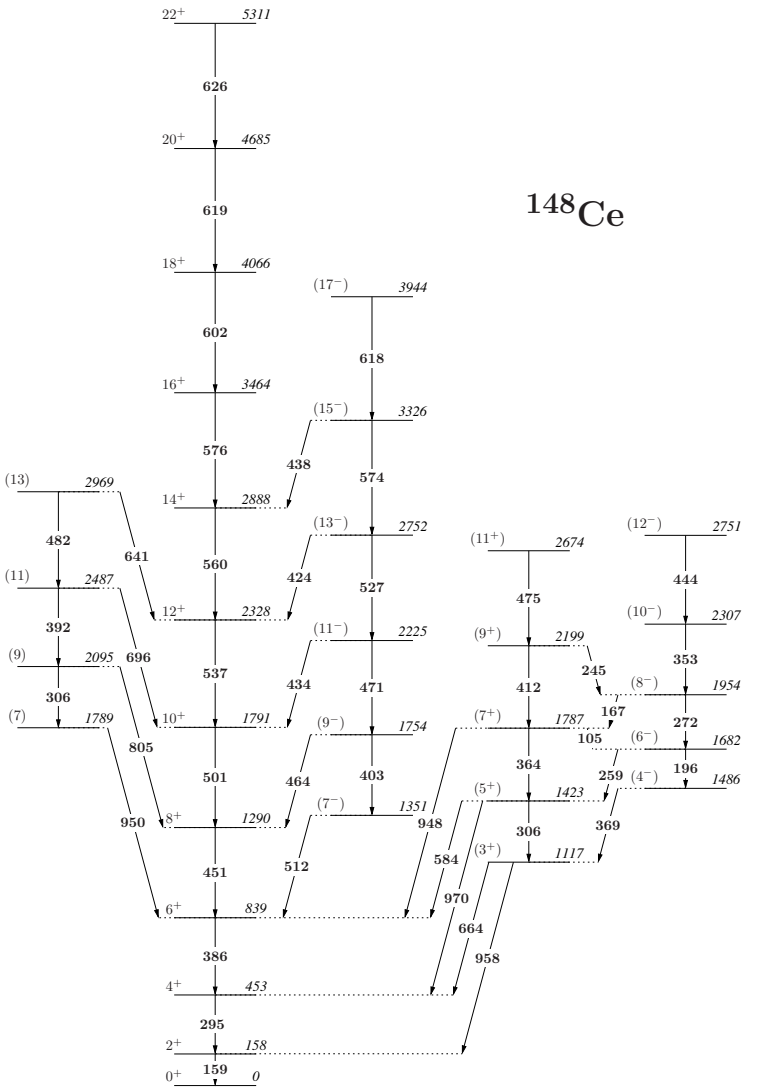
148Ce
22+ 5311
626
20+ 4685
619
18+ 4066
602
16+ 3464
576
14+ 2888
560
12+ 2328
537
10+ 1791
501
8+ 1290
451
6+ 839
386
4+ 453
295
2+ 158
0+ 159 0
(17−) 3944
618
(15−) 3326
574
(13−) 2752
527
(11−) 2225
471
(9−) 1754
403
(7−) 1351
438
424
434
464
512
948
(13) 2969
482
(11) 2487
392
(9) 2095
306
(7) 1789
641
696
805
950
(11+) 2674
475
(9+) 2199
412
(7+) 1787
364
(5+) 1423
306
(3+) 1117
584
970
664
958
245
167
105
259
369
(12−) 2751
444
(10−) 2307
353
(8−) 1954
272
(6−) 1682
196
(4−) 1486

Figure 6.10.

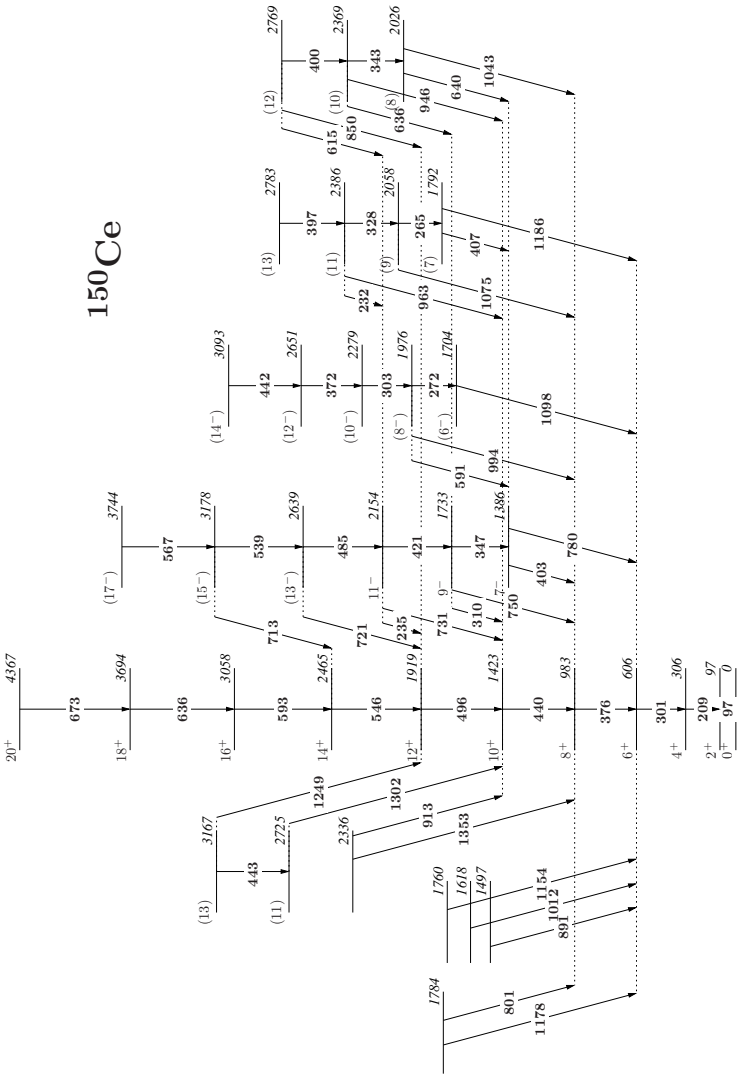

Figure 6.11.

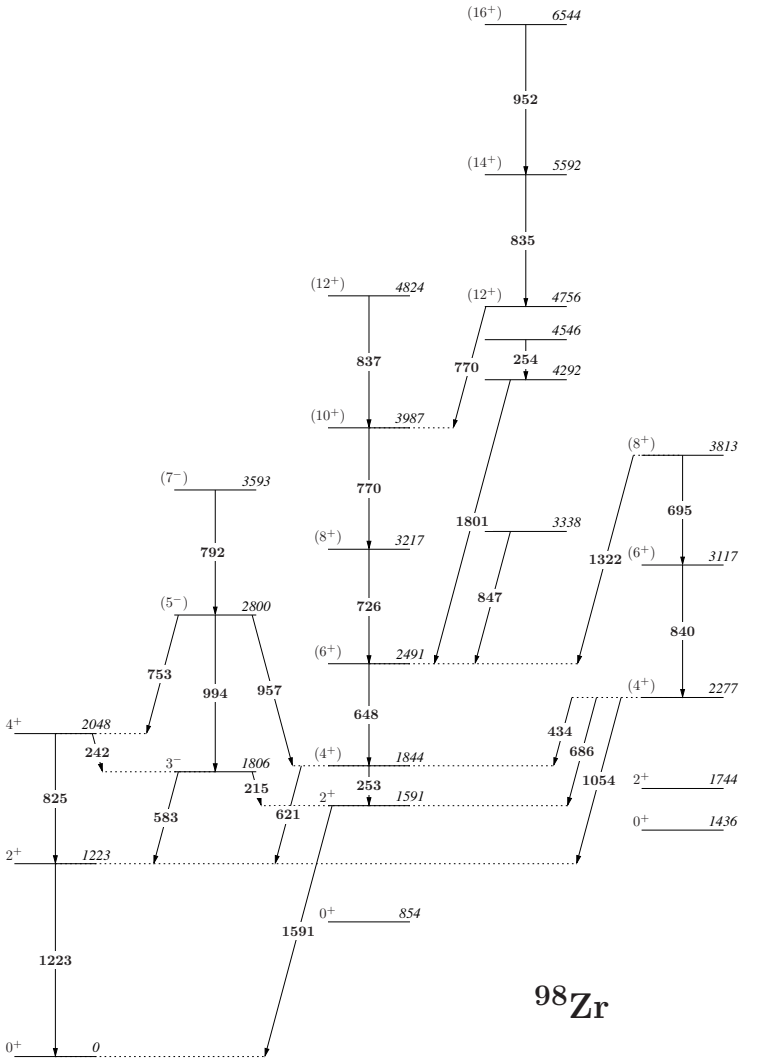
(16+) 6544
952
(14+) 5592
835
(12+) 4824
(12+) 4756
4546
837
770
254
4292
(10+) 3987
(8+) 3813
(7−) 3593
770
695
1801
3338
792
(8+) 3217
1322
(6+) 3117
(5−) 2800
726
847
840
753
994
957
(6+) 2491
(4+) 2277
648
4+ 2048
434
242
3− 1806
(4+) 1844
686
215
253
2+ 1744
825
2+ 1591
1054
583
621
0+ 1436
2+ 1223
0+ 854
1591
1223
98Zr
0+ 0

Figure 6.12.

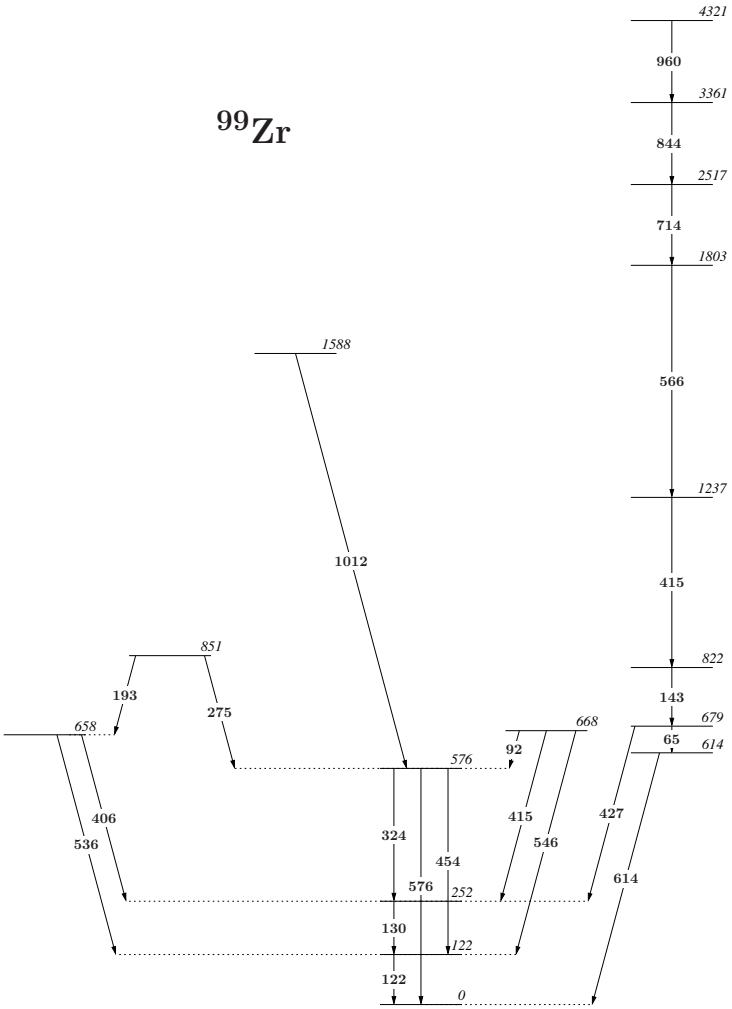
99Zr
4321
960
3361
844
2517
714
1803
566
1237
415
822
143
679
65
614
1588
1012
851
193
275
658
668
92
576
406
536
324
454
415
546
427
614
576
252
130
122
122
0

Figure 6.13.

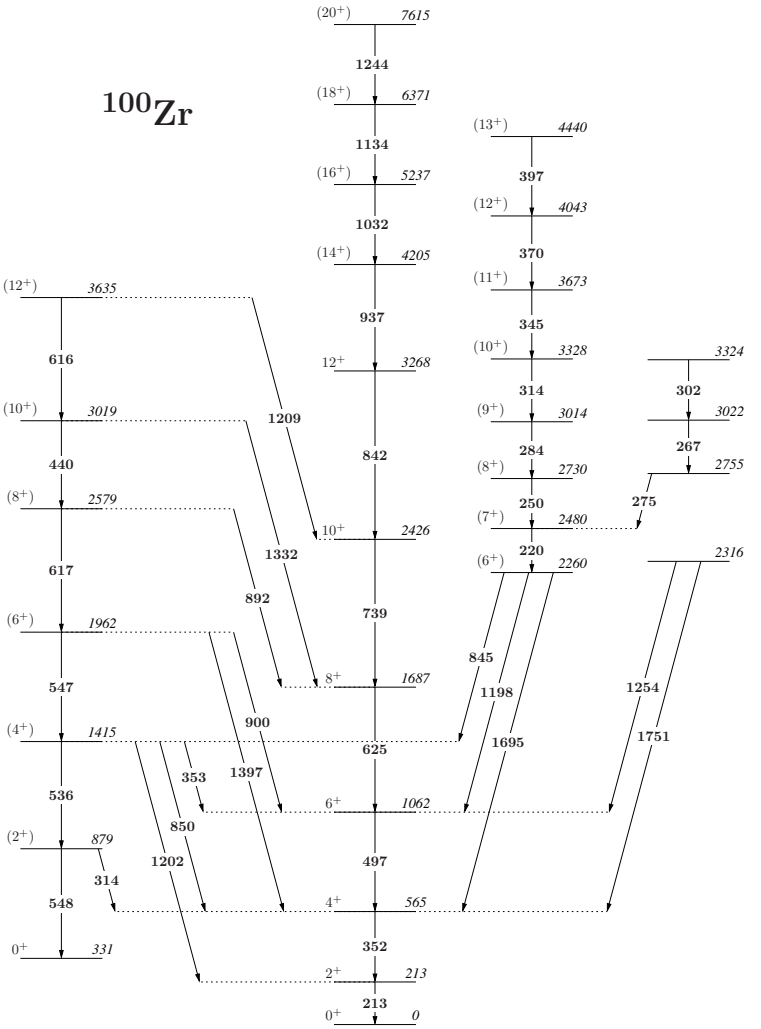
100Zr
(20+) 7615
1244
(18+) 6371
1134
(16+) 5237
1032
(14+) 4205
937
12+ 3268
842
10+ 2426
739
8+ 1687
625
6+ 1062
497
4+ 565
352
2+ 213
213
0+ 0
(13+) 4440
397
(12+) 4043
370
(11+) 3673
345
(10+) 3328
314
(9+) 3014
284
(8+) 2730
250
(7+) 2480
220
(6+) 2260
845
1198
1695
(12+) 3635
616
(10+) 3019
440
(8+) 2579
617
(6+) 1962
547
(4+) 1415
536
(2+) 879
548
0+ 331
1209
1332
892
900
1397
353
850
1202
314
3324
302
3022
267
2755
275
2316
1254
1751

Figure 6.14.

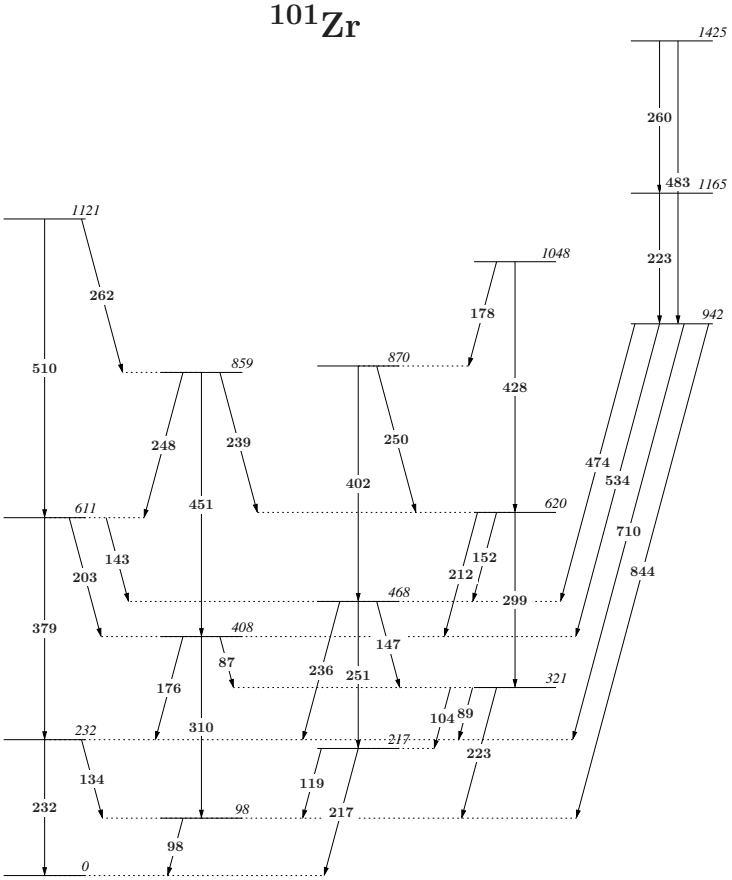
101Zr
1425
260
483
1165
223
942
1121
262
1048
178
510
859
870
428
248
239
250
474
534
402
620
611
451
710
143
152
212
844
203
468
299
379
408
147
87
236
251
321
176
104
89
232
310
217
223
134
119
232
98
217
98
0

Figure 6.15.

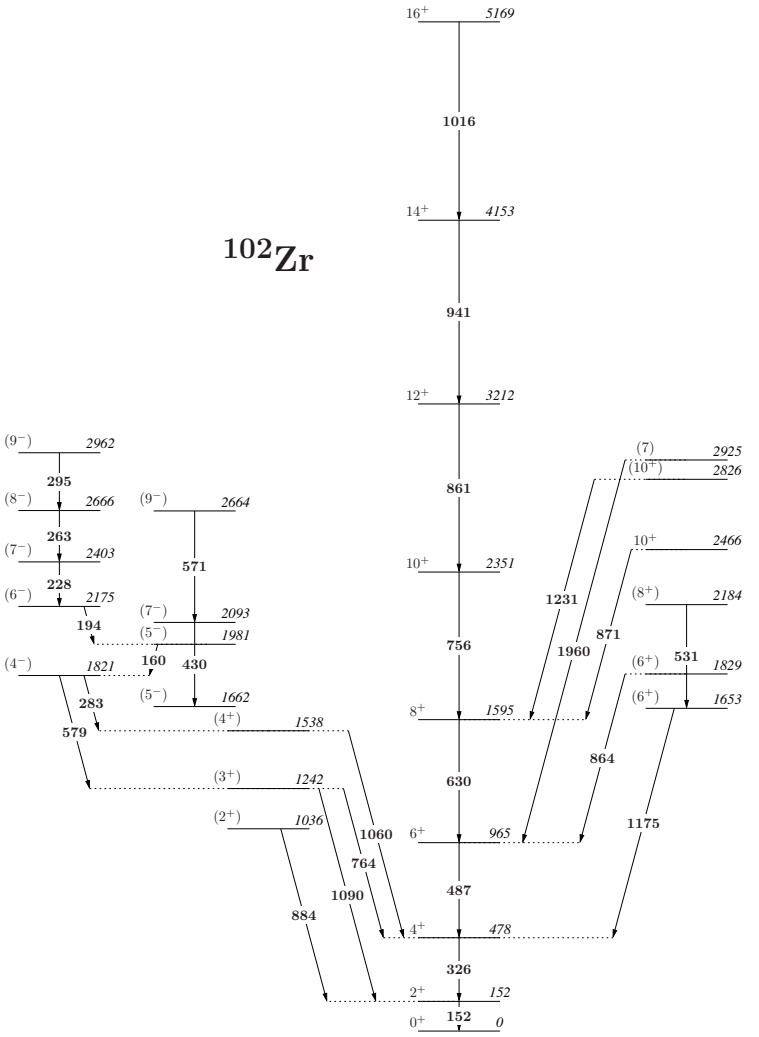
102Zr
16+ 5169
1016
14+ 4153
941
12+ 3212
861
10+ 2351
756
8+ 1595
630
6+ 965
487
4+ 478
326
2+ 152
0+ 152 0
(9−) 2962
295
(8−) 2666
263
(7−) 2403
228
(6−) 2175
194
(4−) 1821
283
579
(9−) 2664
571
(7−) 2093
(5−) 1981
160
430
(5−) 1662
(4+) 1538
(3+) 1242
(2+) 1036
1060
764
1090
884
(7) 2925
(10+) 2826
1231
1960
10+ 2466
(8+) 2184
871
531
(6+) 1829
(6+) 1653
864
1175

Figure 6.16.

6.5 Determination of lifetimes

In this section, the analysis of the ^{252}Cf spontaneous fission data is performed to obtain the lifetimes of the 2^+ and 4^+ states of ^{146}Ce, the 4^+ and 6^+ states of ^{148}Ce, and the 4^+ and 6^+ states of ^{150}Ce. Due to the constraint imposed in the time differences between FATIMA detectors due to the fast-neutron induced background, the determination of the lifetime of the first 2^+ states in ^{148}Ce and ^{150}Ce, reported in [Nnd] to be well above 1 ns, has been impossible from this experimental campaign data set.

6.5.1 ^{146}Ce

2^+ state ($E_f = 410$ keV; $E_d = 258$ keV)

^{146}Ce has a fission yield of 1.01(16)% [Nnd], which is a very favourable circumstance for the fast-timing analysis of its most strongly populated state. As it has been already explained in section 3.2.2, the determination of τ_{2^+} is subject to the proper extraction of the centroid difference between the timing distributions derived from the population and the depopulation of the 2^+ state. This can be achieved by posing energy gates in the Gammasphere detectors at energies that characterise the decay cascade in ^{146}Ce, i.e., in ^{146}Ce (figure 6.9) and its fission partners, ^{A}Zr (figures 6.12 to 6.16).

However, the unfortunate closeness, in terms of the FATIMA energy resolution, of E_f and E_d to the energies of the transitions $4^+ \rightarrow 2^+$ and $2^+ \rightarrow 0^+$, respectively, both in ^{108}Ru and ^{110}Ru, and the high yield of correlated ruthenium and xenon isotopes, strongly restrict the set of possible combinations of energy gates to be posed in the Gammasphere to the ones that characterise unambiguously the cascade in ^{146}Ce. Table 6.2 shows the transitions considered in ^{146}Ce whose energies are similar to energies of transitions in ^{108}Ru, ^{110}Ru. From the results shown, it seems clear that special attention must be paid to the correlated fragments ^{108}Ru-^{140}Xe and ^{110}Ru-^{140}Xe, with yields of 0.67(4)% and 0.39(4)%, respectively [TA+97]. Therefore, the double energy gates posed in the Gammasphere are restricted to combinations of energies in ^{146}Ce that include, at least, one energy that characterises unambiguously ^{146}Ce.

Other possible strategy to characterise the population and the depopulation of the 2^+ state in ^{146}Ce is to combine the energy gates at energies in ^{146}Ce with energy gates in transitions between its fission partners most strongly populated states. The candidate transitions are, therefore, the ones between yrast states in ^{146}Ce (among

^{146}Ce		Contaminant		
Transition	E [keV]	Transition	E [keV]	Nucleus
$4^+ \rightarrow 2^+$	410	$4^+ \rightarrow 2^+$	423	^{108}Ru
			423	^{110}Ru
$2^+ \rightarrow 0^+$	258	$2^+ \rightarrow 0^+$	242	^{108}Ru
			241	^{110}Ru
$8^+ \rightarrow 6^+$	566	$8^+ \rightarrow 6^+$	566	^{140}Xe
$7^- \rightarrow 6^+$	380	$2^+ \rightarrow 0^+$	377	^{140}Xe
$9^- \rightarrow 7^-$	468	$2_2^+ \rightarrow 2^+$	466	^{108}Ru
$11^- \rightarrow 9^-$	543	$13^- \rightarrow 12^+$	543	^{140}Xe
$13^- \rightarrow 11^-$	601	$6_2^+ \rightarrow 4_2^+$	600	^{110}Ru

Table 6.2.: Problematic transitions in ^{146}Ce whose energies coincide with energies in ^{108,110}Ru or ^{A}Xe. The detection of the two first transitions in the FATIMA may actually characterise the first 2^+ state in ^{108}Ru or ^{110}Ru, with a lifetime of $\tau = 0.46(3)$ns [Nnd]. The second set of energies is detected in the Gammasphere.

which the transition $6^+ \rightarrow 4^+$ is the most relevant) and in ^{102}Zr. However, the closeness of the energy of the transition $\frac{21}{2}^+ \rightarrow \frac{17}{2}^+$ in ^{147}Ce, of $E = 501$ keV, to the energy of the $6^+ \rightarrow 4^+$ in ^{146}Ce, of $E = 503$ keV, as well as the higher yield of the correlated ^{147}Ce-^{102}Zr (0.52(10)%) than of the correlated ^{146}Ce-^{102}Zr (0.41(5)%) makes the usage of the transitions in ^{102}Zr very inconvenient. These numerous constraints yield the reduced set of combinations of energies which can be used as cleaning gates shown in table 6.3.

Figures 6.17a and 6.17b show the energy spectra obtained with the energy gates explained above, posed in the Gammasphere detectors, and an additional energy gate in a FATIMA detector. In the *direct* case ($2^+ \rightarrow 0^+$ transition used as time-walk reference), the gate in the FATIMA detector is at $E_d = 258$ keV, whereas in the *inverse* ($4^+ \rightarrow 2^+$ transition used as time-walk reference) case, the gate in the FATIMA detector is at $E_f = 410$ keV. The parameters of the gaussian functions that have been fitted to the spectra 6.17a and 6.17b, shown in table 6.5, confirm the cleanliness of the peaks, even in the case of the FATIMA. The mean value $\mu_{Ref.:4^+\rightarrow 2^+} = 256$ keV is slightly off the actual value of $E_d = 258$ keV, yet still within the energy resolution. However, a more careful inspection of the Gammasphere spectra reveals the presence of the transition $4^+ \rightarrow 2^+$ from ^{108}Ru and ^{110}Ru, with an energy of $E = 422$ keV, in figure 6.17a, whereas the transition $2^+ \rightarrow 0^+$ in the same isotopes,

	503 keV	566 keV	615 keV	380 keV	468 keV	543 keV	601 keV	959 keV	183 keV
503 keV		•	•	•	•	•	•		
566 keV	•								
615 keV	•								
380 keV	•								
468 keV	•								
543 keV	•								
601 keV	•								
959 keV									•
183 keV								•	

Table 6.3.: Combinations of energies in ^{146}Ce used as double gates in the Gammasphere to characterise the population and depopulation of the 2^+ state in ^{146}Ce in the FATIMA

with an energy of $E = 241$ keV, is visible in figure 6.17a. Despite the small height, their contribution to the timing distributions must be considered. Since the fission yield of ^{110}Ru is almost twice as large as that of ^{108}Ru, and their contribution to timing is expected to be very similar, due to the similar lifetimes of their 2^+ states [Nnd], only ^{110}Ru will be considered, for the sake of simplicity.

As explained in section 6.2, the measured centroid difference, ΔC, can be expressed as a linear combination of centroid differences originated from coincidences between the time-walk reference transition and the other transition of the cascade, ΔC_{Ce}, energies that constitute the Compton background, ΔC_B, and in this particular case, transitions in ^{110}Ru, ΔC_{Ru}:

$$\Delta C = \frac{P_{Ru}}{P_{Ru}+P_{Ce}+B}\Delta C_{Ru} + \frac{P_{Ce}}{P_{Ru}+P_{Ce}+B}\Delta C_{Ce} + \frac{B}{P_{Ru}+P_{Ce}+B}\Delta C_B \qquad (6.8)$$

where P_{Ru}, P_{Ce} and B are the number of coincidences from ^{110}Ru, ^{146}Ce and background, respectively. It is very convenient to express equation 6.8 as:

$$\Delta C = \frac{P_{Ru}+P_{Ce}}{P_{Ru}+P_{Ce}+B}\left(\frac{P_{Ru}}{P_{Ru}+P_{Ce}}\Delta C_{Ru} + \frac{P_{Ce}}{P_{Ru}+P_{Ce}}\Delta C_{Ce}\right) + \frac{B}{P_{Ru}+P_{Ce}+B}\Delta C_B \qquad (6.9)$$

which is equivalent to equation 6.3, with P being the sum of counts in the peak, both from ^{146}Ce and ^{110}Ru, and ΔC_T being the weighted sum of centroid differences, ΔC_{Ce} and ΔC_{Ru}:

Ref. trans.	μ [keV]	σ [keV]	FWHM [%]	FWHM$_{calib}$ [%]
$2^+ \rightarrow 0^+$	410.4(12)	8.2(11)	4.7(7)	5.6(2)
$4^+ \rightarrow 2^+$	255.6(12)	8.7(13)	8.0(12)	7.9(2)

Table 6.4.: Properties of the fits in figures 6.17a and 6.17b: *Left:* Parameters of the gaussian functions fitted to the full-energy peaks; *Right:* Derived energy resolution from the fits and from the calibration equation 5.3.

Ref. trans.	Π	ΔC [ps]	ΔC_B [ps]	ΔC_T [ps]
$2^+ \rightarrow 0^+$	0.33(4)	447(16)	353(3)	732(77)
$4^+ \rightarrow 2^+$	0.32(4)	-447(16)	-352(9)	-744(85)

Table 6.5.: Parameters used in the calculation of τ_{2^+}

$$\Delta C_T = \frac{P_{Ce}}{P_{Ce}+P_{Ru}}\Delta C_{Ce} + \frac{P_{Ru}}{P_{Ce}+P_{Ru}}\Delta C_{Ru} \tag{6.10}$$

Thus, the determination of ΔC_{Ce} and, subsequently τ, requires firstly the extraction of ΔC_T as if it was produced by a single cascade and secondly, the calculation of the fractions P_{Ce}/P_T and P_{Ru}/P_T, assuming that ΔC_{Ru} can be calculated from the lifetime found in literature and the calibrated *PRD*.

Figure 6.18 shows the delayed and antidelayed timing distributions obtained when including the energy gate in the FATIMA detectors around the fitted value, μ. The centroid differences diagrams depicted in figures 6.19a and 6.19b show the dependency of the centroid difference on energy. In order to interpolate the contribution of the Compton background to the timing at the transition energy, the centroid differences at several positions of the energy spectrum around the peak, marked with vertical arrows in figures 6.17a and 6.17b, have been calculated. In table 6.5, a summary of the parameters necessary to extract the ΔC_T, obtained when using both the $2^+ \rightarrow 0^+$ and the $4^+ \rightarrow 2^+$ as reference transitions is presented.

In order to disentangle the individual contributions of the 2^+ in ^{146}Ce and in ^{110}Ru to the timing spectra 6.18, the calculation of the fractions $\frac{P_{Ce}}{P_{Ce}+P_{Ru}}$ and $\frac{P_{Ru}}{P_{Ce}+P_{Ru}}$ is needed. Since their extraction from the FATIMA energy spectrum is not possible due to its poor energy resolution, the Gammasphere energy spectrum has been used. Figures 6.20a y 6.20b show a close view of the Gammasphere energy spectra at the region of interest, both for the *direct* and *inverse* cases. From their integral and the efficiency calibration of the arrays, the number of counts in the FATIMA is calculated and shown in table 6.6. Its large uncertainty originates from the large

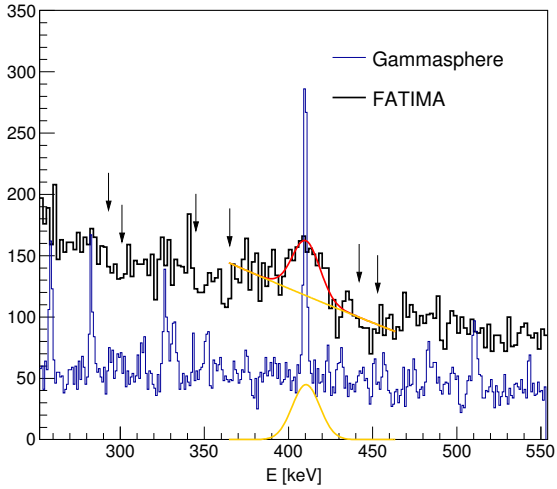

(a) Direct

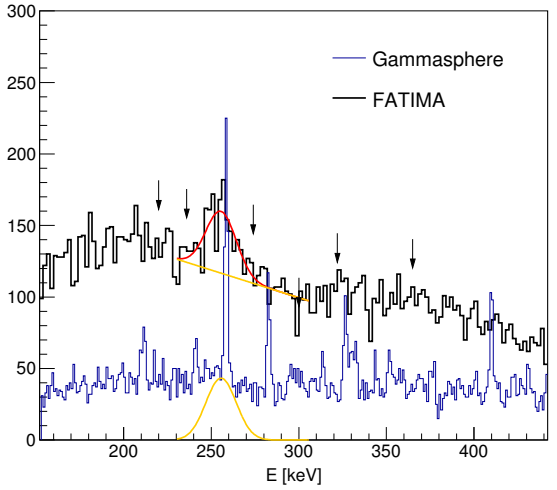

(b) Inverse

Figure 6.17.: FATIMA and Gammasphere energy spectra

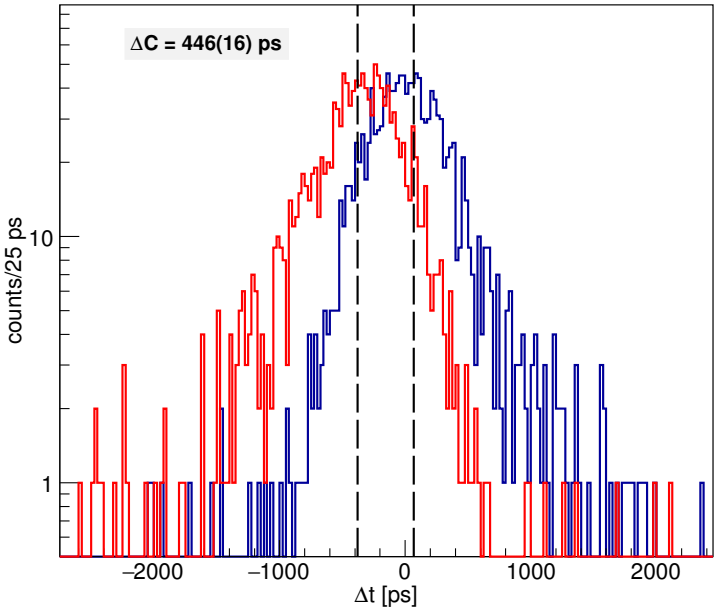

Figure 6.18.: Delayed and antidelayed timing distributions

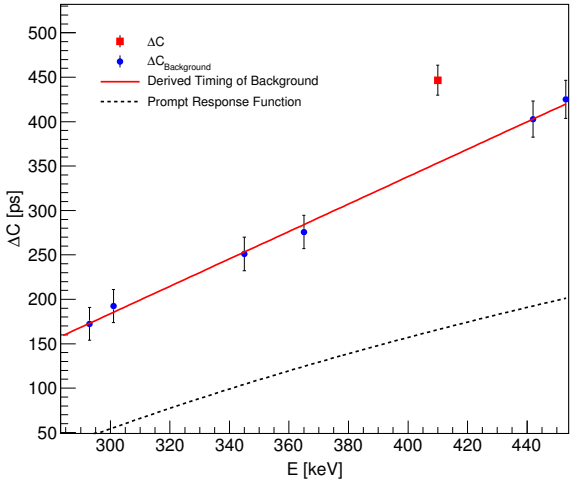

(a) Direct

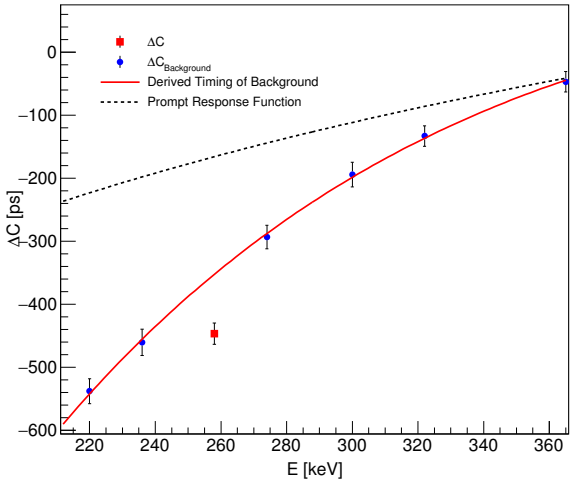

(b) Inverse

Figure 6.19.: Centroid difference diagrams

Ref. trans.		Gammasphere	FATIMA
$2^+ \rightarrow 0^+$	P_{Ce}	607.8(247)	457.6(604)
	P_{Ru}	64.3(83)	47.9(85)
$4^+ \rightarrow 2^+$	P_{Ce}	394.4(199)	370.7(697)
	P_{Ru}	61.5(79)	60.6(139)

Table 6.6.: Number of counts detected in the Gammasphere and calculated in the FATIMA

Ref. trans.	P_{Ru}	ΔC_{Ru} [ps]	P_{Ce}	ΔC_{Ce} [ps]	τ [ps]
$6^+ \rightarrow 4^+$	48(9)	1124(59)	458(61)	711(59)	273(31)
$8^+ \rightarrow 6^+$	61(14)	-1124(59)	371(70)	-700(60)	267(32)

Table 6.7.: Parameters used in the calculation of τ_{6^+} in ^{146}Ce

uncertainty in the FATIMA efficiency calibration. Thus, in order to confirm these values, the gaussian functions fitted to the FATIMA energy spectra in figures 6.17a and 6.17b, that were originally used to determine the peak-to-background ratio, Π, have been integrated leading to total sums of $P = 449.8(223)$ and $P = 342.4(531)$ for the *direct* and *inverse* cases, respectively. They are in good agreement with $P_{Ce} + P_{Ru} = 505.5(610)$ and $P_{Ce} + P_{Ru} = 431.3(711)$, derived from the results in table 6.6.

Eventually, the determination of the lifetime is possible using the parameters listed in table 6.7. ΔC_{Ru} has been obtained using the equation 3.23 with a lifetime $\tau = 462(29)$ ps [Nnd] and a prompt response difference $PRD = 200(10)$ ps. The lifetime derived is $\tau_{2^+} = 270(22)$ ps. It is interesting to point out that the similarity between ΔC_T shown in table 6.5 and ΔC_{Ce} shown in table 6.7, is an indication of the weak influence of ^{110}Ru in the timing distributions 6.18.

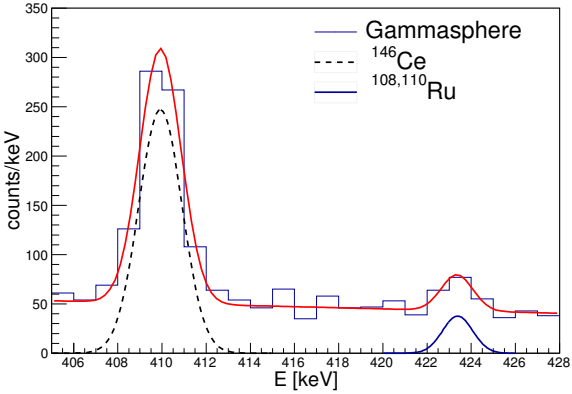

(a) Direct

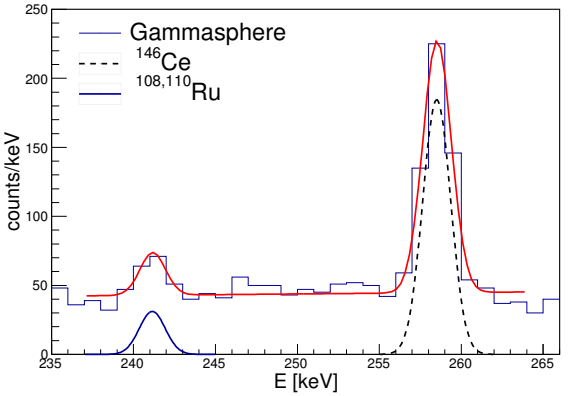

(b) Inverse

Figure 6.20.: Gammasphere energy spectra: in this close view, the contribution of the transitions in ^{146}Ce and in ^{108,110}Ru can be easily separated, due to the superior Gammasphere energy resolution.

	258 keV	566 keV	283 keV	380 keV	543 keV	487 keV
258 keV		•		•	•	•
566 keV	•					
283 keV					•	
380 keV	•				•	
543 keV	•		•	•		
487 keV	•					

Table 6.8.: Combinations of energies in ^{146}Ce (left) and in ^{146}Ce and ^{102}Zr (right) used as double gates in the Gammasphere to characterise the population and depopulation of the 4^+ state in ^{146}Ce in the FATIMA

4^+ state ($E_f = 503$ keV; $E_d = 410$ keV)

The determination of the lifetime of the first 4^+ state in ^{146}Ce requires the detection of the transitions $6^+ \rightarrow 4^+$, with energy $E = 503$ keV, and $4^+ \rightarrow 2^+$, with energy $E = 410$ keV in the FATIMA detectors. As it has been already mentioned in the previous section, $E = 410$ keV is, in terms of the FATIMA energy resolution, close to the energy of the transitions $4^+ \rightarrow 2^+$ in ^{108}Ru and ^{110}Ru, of $E = 423$ keV in both cases. However, unlike in the previous case, the occasional detection of these contaminants does not contribute to the timing distributions with an effective ΔC due to the different energies involved, which simplifies the analysis. Nevertheless, the choice of energies to pose the cleaning gates on, must be careful no to coincide with energies characteristic of ^{108}Ru, ^{110}Ru, nor with their fission partners, ^{A}Xe. Following the same criteria as in the case of the 2^+ state, of using pairs of energies in which at least one of them characterises unambiguously ^{146}Ce, the set of double energy gates depicted in table 6.8 is obtained.

The application of this set of double energy gates in the Gammasphere detectors and an additional energy gate at the reference transition in the FATIMA yield the energy spectra depicted in figures 6.21a and 6.21b. In the *direct* case, i. e. using the transition $4^+ \rightarrow 2^+$ as time-walk reference transition, it is clear from the Gammasphere spectrum that the peak at $E = 503$ keV is not properly distinguishable for the FATIMA detectors from the peak at $E = 511$ keV present in the background radiation in the laboratory. However, when using the transition $6^+ \rightarrow 4^+$ as time-walk reference the true coincidences peak at $E_{4^+ \rightarrow 2^+} = 410$ keV arises from the random coincidences in the background, making the analysis possible. Therefore, in order to calculate the lifetime of the 4^+ state, only the *inverse* case has been used.

Ref. trans.	μ [keV]	σ [keV]	FWHM [%]	FWHM$_{calib}$ [%]
$6^+ \rightarrow 4^+$	408.6(10)	8.9(13)	5.1(7)	5.7(2)

Table 6.9.: Properties of the fit in figure 6.21b: *Left:* Parameters of the gaussian function fitted to the full-energy peak; *Right:* Derived energy resolution from the fit and from the energy resolution calibration.

Ref. trans.	Π	ΔC [ps]	ΔC_B [ps]	τ [ps]
$6^+ \rightarrow 4^+$	0.50(6)	-76(12)	-53(6)	25(20)

Table 6.10.: Parameters used in the calculation of τ_{4^+}

The agreement between the energy resolution obtained for the peak fitted in the FATIMA energy spectrum in figure 6.21b and its expected value from the energy resolution calibration, shown in table 6.9, confirms the proper isolation of the peak at $E = 410$ keV. The subsequent gate at that energy in the FATIMA detectors yields the delayed and antidelayed timing distributions drawn in figure 6.22.

The contribution of the Compton background to the timing must be interpolated at the energy of the transition $4^+ \rightarrow 2^+$. A second-order polynomial has been fitted to the set of centroid differences at several energies in the background, marked with vertical arrows in figure 6.23. The parameters used for the extraction of τ_{4^+}, summarised in table 6.10, yield a lifetime of $\tau_{4^+} = 25(20)$ ps.

It is worth to mention here the case of the 3^- state. The analysis of the data acquired for spectroscopic purposes (that involve only the Gammasphere detectors) yielded no evidences of its population in this experiment.

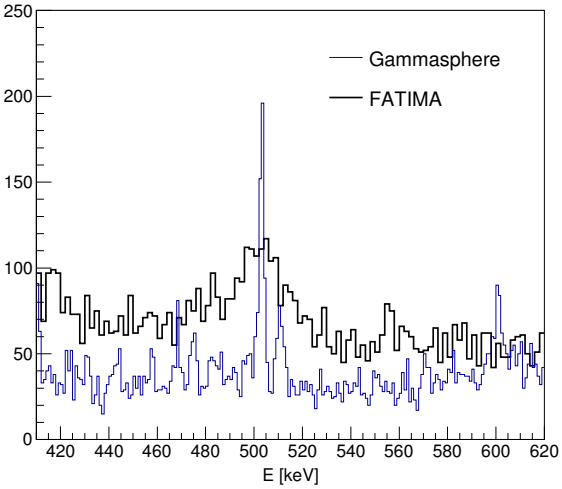

(a) Direct

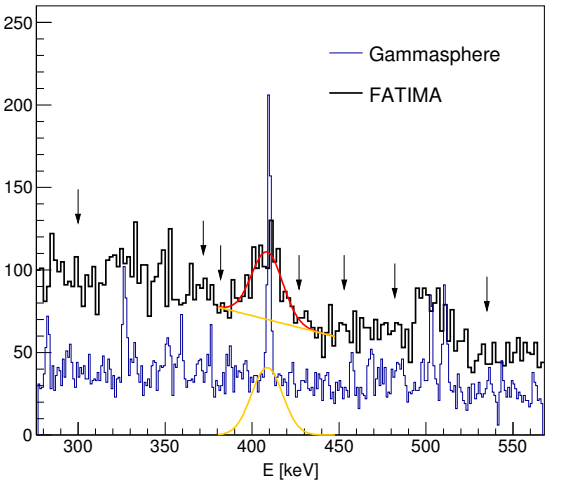

(b) Inverse

Figure 6.21.: FATIMA and Gammasphere energy spectra

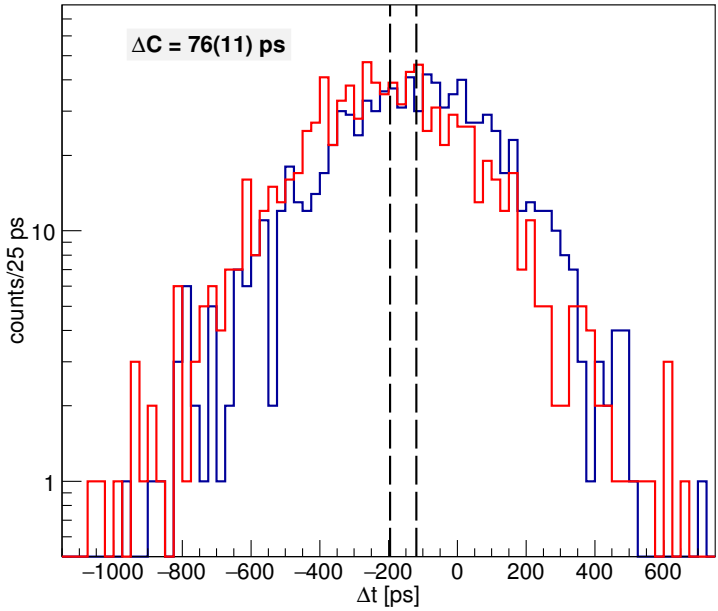

Figure 6.22.: Delayed and antidelayed timing distributions

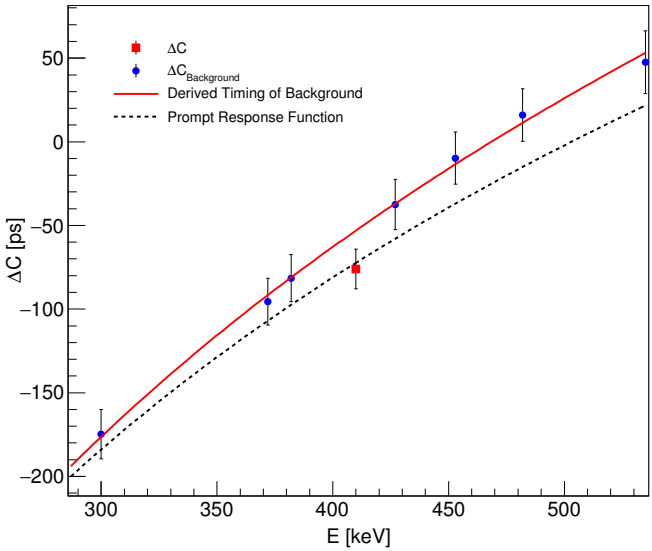

Figure 6.23.: Centroid difference diagram

6.5.2 ^{148}Ce

4^+ state ($E_f = 386$ keV; $E_d = 295$ keV)

The analysis that leads to the determination of the lifetime of the first 4^+ state is based on the work by C. Bieniek [Bie18]. Among the neutron-rich cerium isotopes, ^{148}Ce is the one with the highest fission yield, of 2.4(8)% [Nnd]. Therefore, the extraction of the mean lifetime of its first 4^+ state, strongly populated through the deexcitation of higher-lying levels, is relatively easier than the analysis of other neutron-rich cerium isotopes or other states in ^{148}Ce.

The fission yield of correlated fragments of ^{148}Ce and ^{A}Zr shown in table 6.1 makes the usage of energy gates in zirconium isotopes very convenient for the characterisation of the 4^+ state in ^{148}Ce. The yield of correlated ^{148}Ce and ^{100}Zr is 0.63(5)%, whereas the yield of correlated ^{148}Ce and ^{101}Zr is 0.62(16)%, the highest among the correlated Ce-Zr fragments [TA+97]. This is a clear advantage, since it allows for posing cleaning gates in a broad variety of energies.

Tables 6.11 and 6.12 show the set of energies that have been used to pose energy gates in the Gammasphere detectors. They correspond to combinations of energies from transitions in ^{148}Ce (table 6.11) and combinations of energies from transitions in ^{148}Ce and transitions in zirconium isotopes (table 6.12). As it can be seen in table 6.12, only one of the transitions in ^{100}Zr has been used. It is the transition between the yrast 4^+ and 2^+ states, with an energy of $E = 352$ keV. Two reasons explain this choice: its closeness to the energy of the transition $6^+ \rightarrow 4^+$ in ^{148}Ce, in terms of the FATIMA energy resolution, and its strong population from many other states in ^{100}Zr. Using it as the only energy gate from ^{100}Zr ensures the minimisation of its contribution to the timing distributions, whereas it does not strongly affect their statistics.

The usage of these cleaning gates in the Gammasphere yields the energy and timing spectra in the FATIMA displayed in figures 6.24 and 6.25, respectively. The presence of an isolated peak in the Gammasphere energy spectrum ensures the cleanliness of the spectra in the FATIMA. Nevertheless, as a verification of this statement, the parameters of the gaussian function necessary for calculation of the peak-to-background ratio Π are listed in table 6.13. The excellent agreement between the values of the mean and standard deviation extracted from the fit, and their values expected from the FATIMA energy resolution calibration (see section 5.3.2) ensures a proper characterisation of the 4^+ state.

Figure 6.25 shows the timing distributions obtained when imposing the gate in the FATIMA at the energy of the peaks fitted in figures 6.24a and 6.24b. In order to extract the contribution of the Compton background to these timing distributions,

	159 keV	451 keV	501 keV	537 keV	560 keV	576 keV	602 keV	512 keV	464 keV	434 keV	948 keV
159 keV		•	•	•	•	•		•	•		•
451 keV	•		•	•	•	•			•	•	
501 keV	•	•		•	•	•				•	
537 keV	•	•	•		•	•	•				
560 keV	•	•	•	•		•	•				
576 keV	•	•	•	•	•						
602 keV				•	•						
512 keV	•										
464 keV	•	•									
434 keV		•	•								
948 keV	•										

Table 6.11.: Combinations of energies in ^{148}Ce used as double gates in the Gammasphere to characterise the population and depopulation of the 4^+ state in ^{148}Ce in the FATIMA

	352 keV	176 keV	310 keV
159 keV	•	•	•
451 keV	•	•	•
537 keV	•		

Table 6.12.: Combinations of energies in ^{148}Ce and ^{100}Zr (left), and ^{101}Zr (right) used as double gates in the Gammasphere to characterise the population and depopulation of the 4^+ state in ^{148}Ce in the FATIMA

Ref. trans.	μ [keV]	σ [keV]	FWHM [%]	FWHM$_{calib}$ [%]
$4^+ \rightarrow 2^+$	384.9(6)	9.6(6)	5.9(3)	5.9(2)
$6^+ \rightarrow 4^+$	294.5(6)	8.5(5)	6.8(4)	7.2(2)

Table 6.13.: Properties of the fits in figures 6.24a and 6.24b: *Left:* Parameters of the gaussian functions fitted to the full-energy peaks; *Right:* Derived energy resolution from the fits and from the calibration equation 5.3.

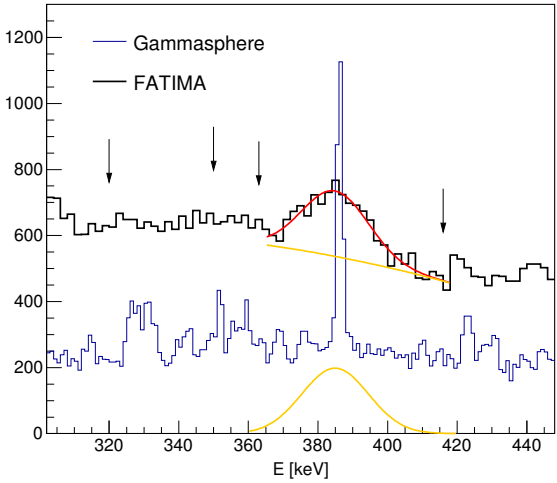

(a) Direct

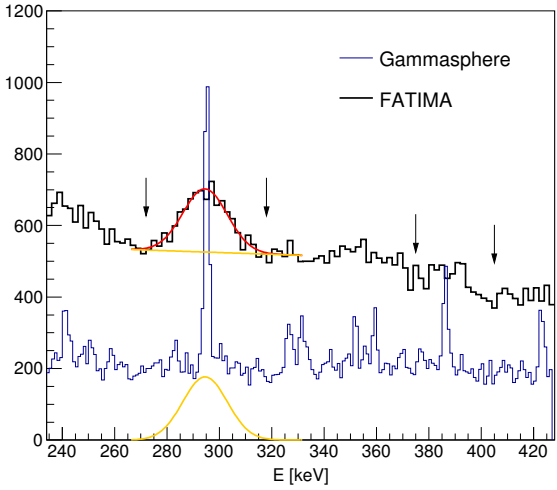

(b) Inverse

Figure 6.24.: FATIMA and Gammasphere energy spectra

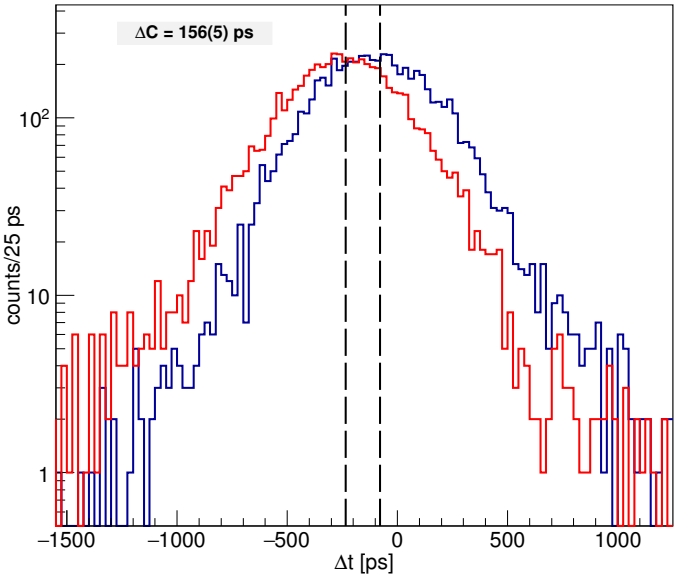

Figure 6.25.: Delayed and antidelayed timing distributions

Ref. trans.	Π	ΔC [ps]	ΔC_B [ps]	τ [ps]
$4^+ \rightarrow 2^+$	0.32(2)	156(6)	142(3)	52(14)
$6^+ \rightarrow 4^+$	0.29(2)	-156(6)	-144(4)	50(16)

Table 6.14.: Parameters used in the calculation of τ_{4^+}

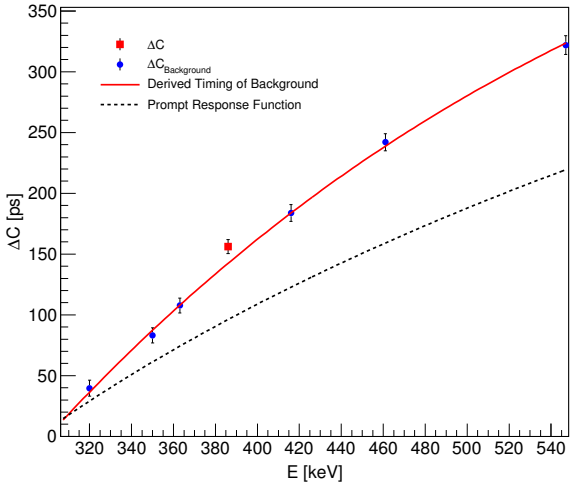

(a) Direct

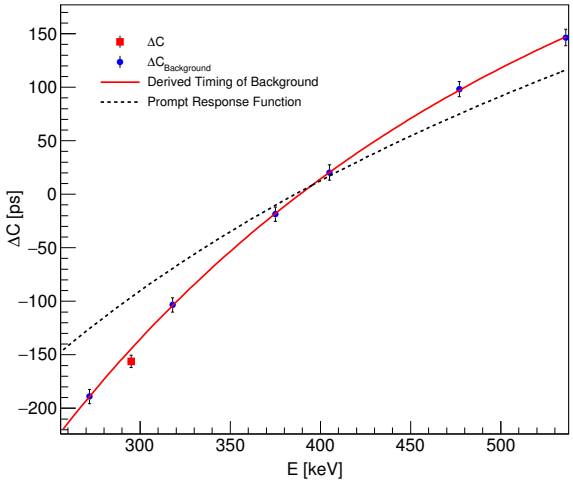

(b) Inverse

Figure 6.26.: Centroid difference diagrams

the dependency of ΔC_B on energy has been derived from the centroid differences obtained at several positions of the FATIMA energy spectra where only background is visible, marked with vertical arrows, and interpolated at the relevant energy, as it can be seen in figures 6.26a and 6.26b.

Table 6.14 shows the results obtained for the different parameters necessary to calculate the lifetime, which has been determined to be $\tau_{4^+} = 51(10)\,\mathrm{ps}$.

6^+ state ($E_f = 451\,\text{keV}$; $E_d = 386\,\text{keV}$)

The case of the first 6^+ state of ^{148}Ce is more challenging than the one of the 4^+ state, since $E_f = 451\,\text{keV}$ and $E_d = 386\,\text{keV}$ are undistinguishable from the energies $E_{4^+\to2^+} = 458\,\text{keV}$ and $E_{2^+\to0^+} = 377\,\text{keV}$ of ^{140}Xe, within the FATIMA energy resolution. Since these are the transitions that populate and depopulate the 2^+ state, the measured centroid difference for the 6^+ state in ^{148}Ce can be strongly affected by the lifetime $\tau_{2^+} = 102\,\text{ps}$ of ^{140}Xe [Ili+16]. It is a situation very similar to the one described in the analysis of the 2^+ state in ^{146}Ce, with the aggravating circumstance that the lifetime of the 6^+ state in ^{148}Ce is expected to be shorter than that of the 2^+ state in ^{140}Xe. Therefore, the steps followed in this analysis are the extraction of ΔC_T as explained in section 6.5.1, and the subsequent estimation of the fractions of ^{148}Ce and ^{140}Xe that contribute to ΔC_T, and allow for the derivation of the lifetime of the 6^+ state in ^{148}Ce.

In order to minimise the contribution to timing of coincidences originated from ^{140}Xe, the set of combinations of energy gates in the Gammasphere shown in table 6.16 has been posed. Special attention to the presence of ruthenium has been paid (table 6.15), since the fission yield of ^{140}Xe and its correlated fragments ^{108}Ru (0.64 %) and ^{110}Ru (0.39 %) is comparable to the fission yield of ^{148}Ce [TA+97]. In particular, the transitions of the yrast band in ^{148}Ce $12^+ \to 10^+$, with energy $E = 537\,\text{keV}$, and $16^+ \to 14^+$, with energy $E = 576\,\text{keV}$, have not been used due to their closeness to the strong transitions between yrast states $6^+ \to 4^+$ with energy $E = 575.5\,\text{keV}$ in ^{108}Ru, and $6^+ \to 4^+$ with energy $E = 575.7\,\text{keV}$, as well as the transition from the level at 3175 keV to the level 2637 keV with energy $E = 538\,\text{keV}$, in ^{110}Ru. Unlike the previous case, transitions in ^{A}Zr have not been used as cleaning gates, due to the subsequently unavoidable presence of the transition from the level at 2751 keV to the level at 2307 keV, with energy $E = 444\,\text{keV}$ in ^{148}Ce, very close to $E_f = 451\,\text{keV}$. The only way to prevent its contribution to the timing distributions is to use transitions at higher energies in different bands. The combinations of energies used as double gates in the Gammasphere is shown in table 6.16. In figure 6.28 the delayed and antidelayed distributions obtained with this set of double energy gates is shown.

Figures 6.27a and 6.27b show the energy spectra obtained when using the $6^+ \to 4^+$ and the $8^+ \to 6^+$ transitions as time-walk reference transitions, respectively. As it was anticipated, and in spite of the usage of cleaning energy gates, a small contribution from ^{140}Xe is observed at $E = 458\,\text{keV}$ in the Gammasphere in 6.27a, and at $E = 377\,\text{keV}$ in the Gammasphere in 6.27b. Although the peaks are very small relatively to the ones from ^{148}Ce, their influence in the timing distributions must not be discarded. Thus, the analysis consists firstly on the extraction

^{148}Ce		Contaminant		
Transition	E [keV]	Transition	E [keV]	Nucleus
$8^+ \rightarrow 6^+$	451	$4^+ \rightarrow 2^+$	458	^{140}Xe
$6^+ \rightarrow 4^+$	386	$2^+ \rightarrow 0^+$	377	^{140}Xe
$12^+ \rightarrow 10^+$	537	$3175 \rightarrow 2637$	538	^{110}Ru
$16^+ \rightarrow 14^+$	576	$6^+ \rightarrow 4^+$	575.5	^{108}Ru
		$6^+ \rightarrow 4^+$	575.7	^{110}Ru

Table 6.15.: Problematic transitions in ^{148}Ce whose energies coincide with energies in ^{140}Xe or ^{A}Ru. The detection of the two first transitions in the FATIMA may actually characterise the first 2^+ state in ^{140}Xe, with a lifetime of $\tau = 102(7)$ns [Ili+16]. The second set of energies is detected in the Gammasphere.

	159 keV	295 keV	501 keV	560 keV	602 keV	618 keV	463 keV	434 keV
159 keV		•	•	•			•	
295 keV	•		•	•		•	•	•
501 keV	•	•		•				•
560 keV	•	•	•		•			
602 keV				•				
618 keV		•						
463 keV	•	•						
434 keV		•	•					

Table 6.16.: Combinations of energies in ^{148}Ce used as double gates in the Gammasphere to characterise the population and depopulation of the 6^+ state in ^{148}Ce in the FATIMA

Ref. trans.	μ [keV]	σ [keV]	FWHM [%]	FWHM$_{calib}$ [%]
$6^+ \rightarrow 4^+$	448.8(12)	9.7(14)	5.1(7)	5.3(2)
$8^+ \rightarrow 6^+$	387.8(10)	8.3(13)	5.0(8)	5.9(2)

Table 6.17.: Properties of the fits in figures 6.27a and 6.27b: *Left:* Parameters of the gaussian functions fitted to the full-energy peaks; *Right:* Derived energy resolution from the fits and from the calibration equation 5.3.

Ref. trans.	Π	ΔC [ps]	ΔC_B [ps]	ΔC_T [ps]
$6^+ \rightarrow 4^+$	0.29(3)	91(8)	93(6)	87(44)
$8^+ \rightarrow 6^+$	0.32(4)	-91(8)	-91(4)	-95(42)

Table 6.18.: Parameters used in the calculation of ΔC_T

of ΔC_T, and secondly, on the determination of the fraction of ^{148}Ce and ^{140}Xe that contribute to the timing distributions.

In order to extract the peak-to-background ratio of the peaks in figures 6.27a and 6.27b, the background has been modelled with a first order polynomial, in the first case, and a second order polynomial, in the second case. Table 6.17 summarises the parameters obtained for the mean and standard deviation values of the gaussian functions, as well as the energy resolution values derived from the fit parameters and expected from the calibration expression. The result obtained when using E_d as time-walk reference transition is worse than the other one, but still acceptable within the error bars.

The timing distributions shown in figure 6.28 have been obtained when including the energy gate in the FATIMA at the energy of the fitted peak. In the centroid difference diagrams in figure 6.29, the dependency on energy of the centroid differences is plotted. Out of the parameters extracted from this graph, and listed in table table 6.18, it is possible to obtain the value of ΔC_T.

The calculation of the fractions $\frac{P_{Ce}}{P_{Ce}+P_{Xe}}$ and $\frac{P_{Xe}}{P_{Ce}+P_{Xe}}$ has been performed using the Gammasphere energy spectrum and the efficiency of the arrays, like in section 6.5.1. Figures 6.30a and 6.30b show the Gammasphere energy spectra at the region of interest, both for the *direct* and *inverse* cases. The integral of the gaussian functions that have been fitted, as well as the calculated number of events detected in the FATIMA are shown in table 6.19.These values, of $P_{Ce} + P_{Xe} = 511.2(557)$ and $P_{Ce} + P_{Xe} = 614.3(724)$ are in good agreement with the total number of events integrated directly in the spectra in figures 6.27a and 6.27b, of $P = 482.4(225)$ and $P = 557.1(238)$.

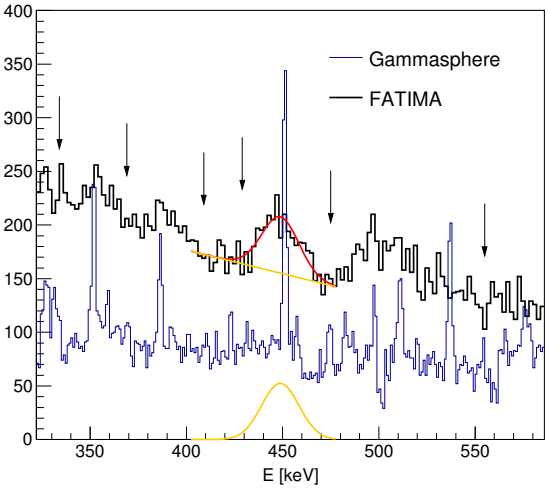

(a) Direct

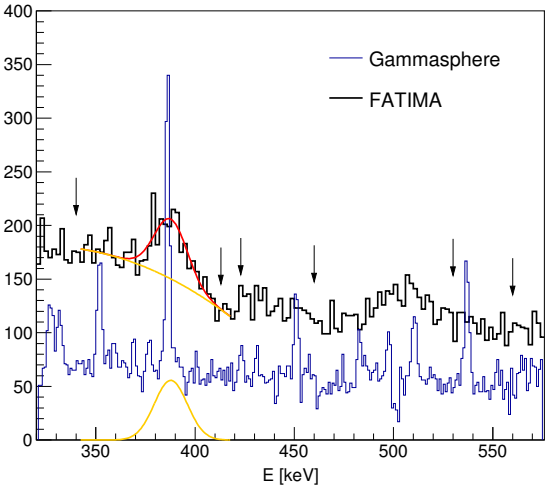

(b) Inverse

Figure 6.27.: FATIMA and Gammasphere energy spectra

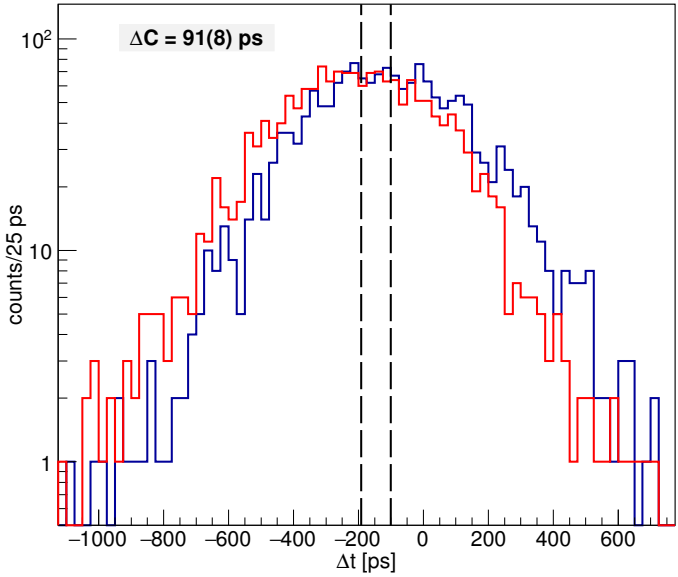

Figure 6.28.: Delayed and antidelayed timing distributions

Ref. trans.		Gammasphere	FATIMA
$6^+ \rightarrow 4^+$	P_{Ce}	620.7(250)	452.3(550)
	P_{Xe}	81.3(92)	58.9(94)
$8^+ \rightarrow 6^+$	P_{Ce}	663.1(257)	510.2(705)
	P_{Xe}	134.1(118)	104.1(549)

Table 6.19.: Number of counts detected in the Gammasphere and calculated in the FATIMA.

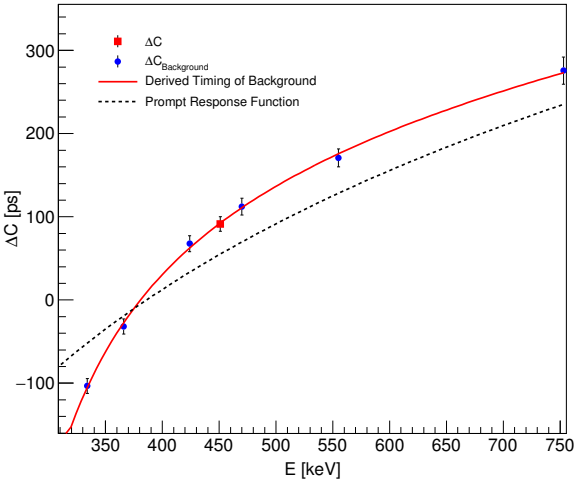

(a) Direct

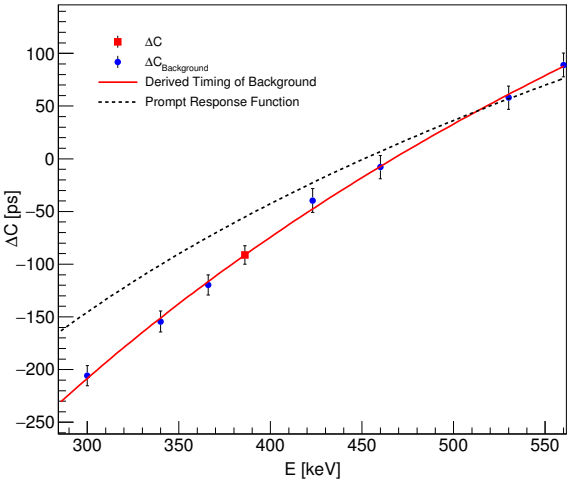

(b) Inverse

Figure 6.29.: Centroid difference diagrams

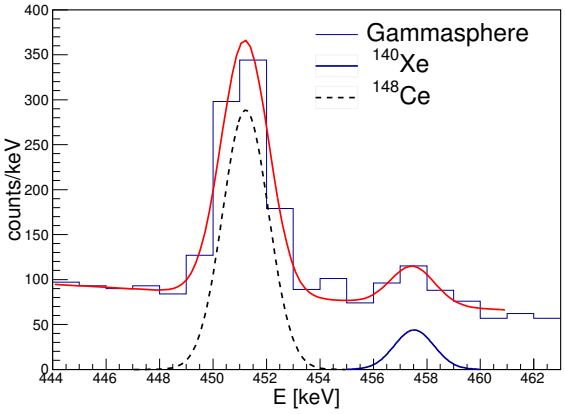

(a) Direct

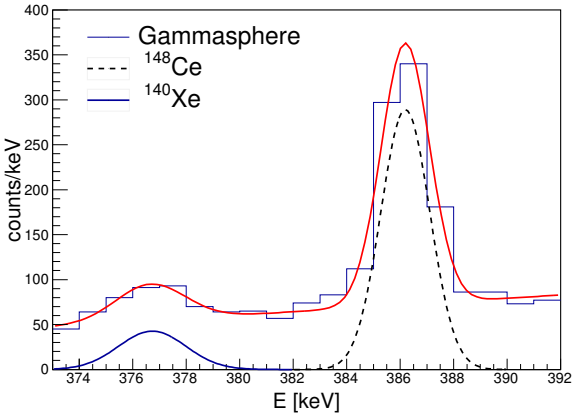

(b) Inverse

Figure 6.30.: Gammasphere energy spectra: in this close view, the contribution of the transition $8^+ \rightarrow 6^+$ in ^{148}Ce and $8^+ \rightarrow 6^+$ in ^{140}Xe can be easily separated, due to the superior Gammasphere energy resolution.

Ref. trans.	P_{Xe}	ΔC_{Xe} [ps]	P_{Ce}	ΔC_{Ce} [ps]	τ [ps]
$6^+ \rightarrow 4^+$	59(10)	283(17)	452(55)	61(52)	3(28)
$8^+ \rightarrow 6^+$	104(17)	-283(17)	510(71)	-51(52)	2(28)

Table 6.20.: Parameters used in the calculation of τ_{6^+} in ^{148}Ce

The knowledge of the fractions of ^{148}Ce and ^{140}Xe, as well as of the lifetime of the 2^+ state of ^{140}Xe, allows for the calculation of ΔC_{Ce} and the subsequent extraction of the lifetime of the 6^+ state. Table 6.20 shows the parameters needed for its calculation. ΔC_{Xe} has been obtained using the equation 3.23 with a lifetime $\tau = 101(7)$ ps [Ili+16] and a prompt response difference of $PRD = 69(10)$ ps. The values obtained are much lower than the sensitivity of the method, allowing only for the establishment of an upper limit for the lifetime of the 6^+ state, $\tau_{6^+} < 22$ ps.

	376 keV	440 keV	547 keV	750 keV	213 keV
376 keV					•
440 keV					•
547 keV					•
750 keV					•
213 keV	•	•	•	•	

Table 6.21.: Combinations of energies in ^{150}Ce and ^{100}Zr used as double gates in the Gammasphere to characterise the population and depopulation of the 2^+ state in ^{146}Ce in the FATIMA

6.5.3 ^{150}Ce

4^+ state ($E_f = 301$ keV; $E_d = 209$ keV)

Among the neutron-rich cerium isotopes studied in this work, ^{150}Ce is the one with the lowest fission yield, of 0.9(6)%. Besides this disadvantage, the construction of the timing distributions that characterise the population and depopulation of the first 4^+ state is strongly affected by the ^{150}Ce main fission partner, ^{100}Zr. Their correlated fission yield is 0.29(5)% and the energy of the transition $2^+ \rightarrow 0^+$ in ^{100}Zr with an energy of $E = 213$ keV, which is indistinguishable from the transition $4^+ \rightarrow 2^+$ in ^{150}Ce for the FATIMA detectors. In order to prevent the contribution from this transition in Zr from contaminating the energy and timing spectra, it must be constantly used as a cleaning gate posed in the Gammasphere detectors, together with characteristic transitions of ^{150}Ce. Besides this important source of possible contamination, no further problematic energies have been found to be relevant. In table 6.21, the set of energies in which cleaning gates have been posed is shown. The three first energies correspond to transitions between states in the yrast band of ^{150}Ce. The transition $2^+ \rightarrow 0^+$ has been discarded, due to the low efficiency of the Gammasphere detectors at that energy ($E_{2^+\rightarrow 0^+} = 97$ keV). In addition, the transition $12^+ \rightarrow 10^+$, with an energy of $E_{12^+\rightarrow 10^+} = 496$ keV has also been discarded, due to its closeness to the energy of the transition $6^+ \rightarrow 4^+$ in ^{100}Zr, $E_{6^+\rightarrow 4^+} = 497$ keV.

The energy spectra resulting from the application of the aforementioned energy gates in the Gammasphere and an additional energy gate in the FATIMA at the energy of the reference transition, are depicted in figures 6.31a (refer-

Ref. trans.	μ [keV]	σ [keV]	FWHM [%]	FWHM$_{calib}$ [%]
$4^+ \rightarrow 2^+$	298.2(12)	9.0(13)	7.1(10)	7.1(2)
$6^+ \rightarrow 4^+$	208.3(19)	8.1(10)	9.2(11)	9.0(3)

Table 6.22.: Properties of the fits in figures 6.27a and 6.27b: *Left:* Parameters of the gaussian functions fitted to the full-energy peaks; *Right:* Derived energy resolution from the fits and from the calibration equation 5.3.

Ref. trans.	Π	ΔC [ps]	ΔC_B [ps]	τ [ps]
$4^+ \rightarrow 2^+$	0.37(4)	441(22)	398(3)	226(44)
$6^+ \rightarrow 4^+$	0.19(4)	-441(22)	-412(2)	231(74)

Table 6.23.: Parameters used in the calculation of τ_{4^+}

ence transition energy of $E = 209\,\text{keV}$) and 6.31b (reference transion energy of $E = 301\,\text{keV}$). A small contribution of the transition $4^+ \rightarrow 2^+$ in ^{148}Ce, with an energy of $E = 295\,\text{keV}$ is observed close to the peak at $E = 301\,\text{keV}$ in the Gammasphere energy spectrum 6.31a. The detection of that energy in the FATIMA is irrelevant, as long as the energies of neither the $2^+ \rightarrow 0^+$ transition nor the $6^+ \rightarrow 4^+$ transition are detected. Indeed, these energies are $E = 159\,\text{keV}$ and $E = 386\,\text{keV}$, very different from $E = 301\,\text{keV}$ in ^{150}Ce. The polynomial functions that are fitted to the background have been chosen for the gaussian function to reproduce the expected parameters for the mean and the standard deviation, according to the FATIMA energy resolution. A summary of the parameters is shown in table 6.22. The mean obtained for the $6^+ \rightarrow 4^+$, $\mu = 298.8(12)\,\text{keV}$ is slightly lower than the reported value in reference [Nnd], of $E = 300.7\,\text{keV}$. However, the value of the energy resolution from the fit parameters is in very good agreement with the value expected at that energy from the calibration equation 5.3.

Figure 6.32 shows the timing distributions obtained when posing the energy gate around the peak detected in the FATIMA. The centroid difference diagrams shown in figures 6.33a and 6.33b show the dependency of the centroid differences on energy. The determination of ΔC_B has been done by interpolating, at the energy of interest, the function fitted to the set of centroid differences calculated for regions of the energy spectra around the peak where only background is present.

Table 6.23 summarises the parameters necessary for the determination of τ_{4^+}, which has been calculated to be $\tau_{4^+} = 227(38)\,\text{ps}$.

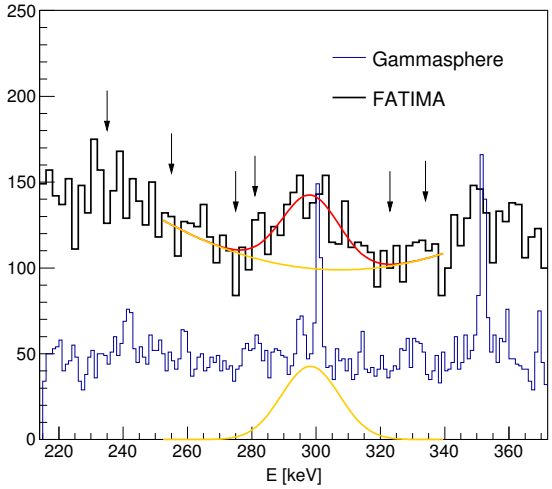

(a) Direct

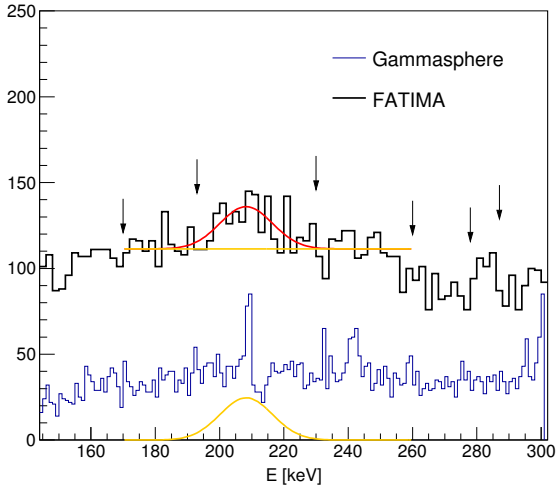

(b) Inverse

Figure 6.31.: FATIMA and Gammasphere energy spectra

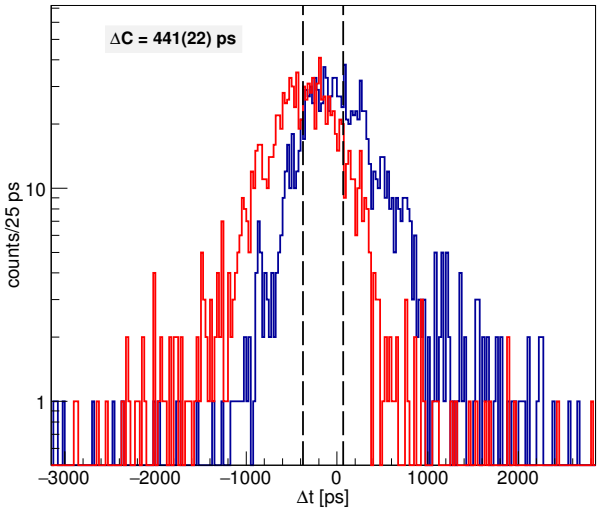

Figure 6.32.: Delayed and antidelayed timing distributions

6^+ state ($E_f = 376$ keV; $E_d = 301$ keV)

The analysis of the 6^+ state in ^{150}Ce is, like the cases of the 2^+ in ^{146}Ce and the 6^+ in ^{148}Ce, especially challenging, because the two transitions that must be detected in coincidence and provide the timing information are undistinguishable from two transitions in ^{148}Ce that populate and depopulate its 4^+ state. Therefore, one of the aims of this analysis is to minimise the contamination from ^{148}Ce, whose fission yield is higher than that of ^{150}Ce. As it has been already done in previous sections, this is achieved by posing energy gates in the Gammasphere in characteristic transitions of ^{150}Ce or its fission partners. In this case, the only Zr isotope whose correlated yield with ^{150}Ce is relevant is ^{100}Zr, as mentioned in the previous section. However, the energy of one of the characteristic transitions in ^{100}Zr ($E_{4^+\rightarrow 2^+} = 352$ keV) is quite close to the energy of the transition $8^+ \rightarrow 6^+$ in ^{150}Ce, of $E = 376$ keV. Despite they are distinguishable for the FATIMA, that energy in ^{100}Zr is the only one that has been picked among the fission partners in order to optimise the cleanliness of the spectra. The other energies, listed in table 6.24, belong to the yrast band of ^{150}Ce.

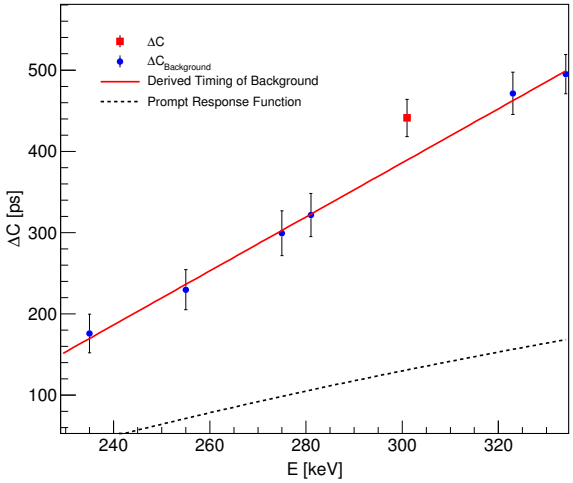

(a) Direct

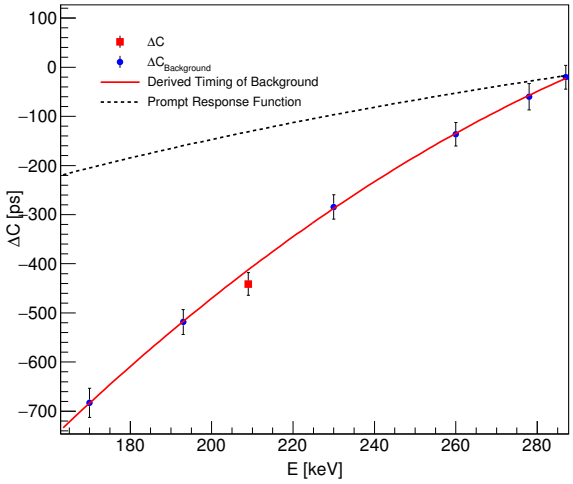

(b) Inverse

Figure 6.33.: Centroid difference diagrams

	352 keV	209 keV	440 keV	496 keV	546 keV	593 keV
352 keV			•			
209 keV			•	•	•	•
440 keV	•	•		•	•	
496 keV		•	•			•
546 keV		•	•			•
593 keV		•		•	•	

Table 6.24.: Combinations of energies in ^{150}Ce and ^{100}Zr used as double gates in the Gammasphere to characterise the population and depopulation of the 6^+ state in ^{150}Ce in the FATIMA

The energy spectra resulting from the application of the aforementioned energy gates in the Gammasphere and an additional energy gate in the FATIMA at the energy of the reference transition are depicted in figures 6.34a and 6.34b. The functions that are fitted to the FATIMA energy spectra to calculate the peak-to-background ratio have been chosen for the gaussian function to reproduce the expected parameters for the mean and the standard deviation, according to the energy resolution calibration. Like in the cases of the 2^+ in ^{146}Ce and the 6^+ in ^{148}Ce, small contributions from the contaminant at $E = 386\,\text{keV}$ in the Gammasphere energy spectrum in figure 6.34a, as well as at $E = 295\,\text{keV}$ in figure 6.34a, and at in figure 6.34a are visible.

As it can be seen in figure 6.34a, the peak at the energy of the transition $8^+ \rightarrow 6^+$ is not properly isolated in the FATIMA energy spectrum. For that reason, only the energy spectrum obtained when using the transition that depopulates the 6^+ state as reference has been considered. The parameters obtained from the fit to the peak at $E = 301\,\text{keV}$ are summarised in table 6.25. In spite of the slightly high value of σ, it is in agreement with the value expected from the FATIMA energy resolution, within the error bars. The centroid differences between the transitions around $E = 301\,\text{keV}$ and $E = 376\,\text{keV}$ (where the FATIMA energy gate is posed) is plotted in figure 6.35. The interpolation of the timing contribution of the background at $E = 301\,\text{keV}$ is achieved by fitting a second order polynomial to the set of centroid differences at the positions marked with vertical arrows in figure 6.34b. The combination of these results, drawn in the centroid differences diagram in figure 6.36 yields a value of $\Delta C_T = 163(54)\,\text{ps}$.

In order to extract P_{148} and P_{150} at the FATIMA, the number of counts detected in the Gammasphere has been calculated. Figure 6.37 shows the gaussian functions

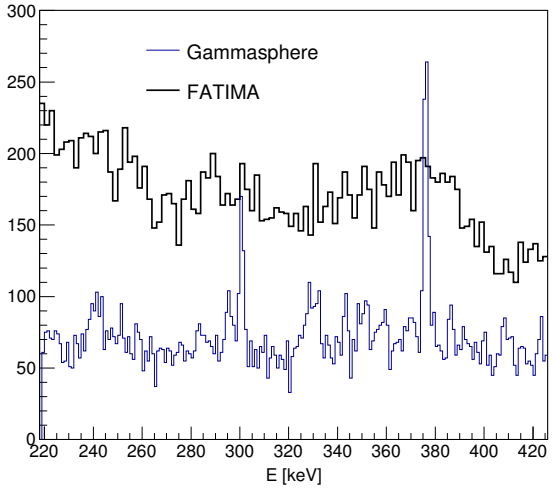

(a) Direct

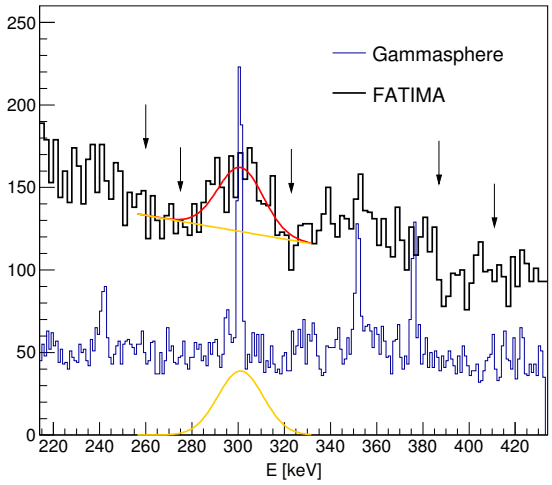

(b) Inverse

Figure 6.34.: Energy spectra

Ref. trans.	μ [keV]	σ [keV]	FWHM [%]	FWHM$_{calib}$ [%]
$8^+ \rightarrow 6^+$	301.0(15)	9.8(14)	7.7(11)	7.0(2)

Table 6.25.: Properties of the fits in figures 6.27a and 6.27b: *Left:* Parameters of the gaussian functions fitted to the full-energy peaks; *Right:* Derived energy resolution from the fits and from the calibration equation 5.3.

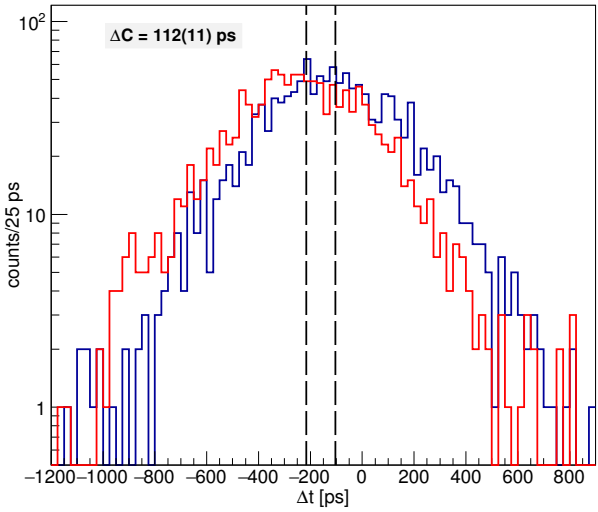

Figure 6.35.: Delayed and antidelayed timing distributions

Ref. trans.	Π	ΔC [ps]	ΔC_B [ps]	ΔC_T [ps]
$8^+ \rightarrow 6^+$	0.27(3)	-112(11)	-99(3)	163(54)

Table 6.26.: Parameters used in the calculation of ΔC_T

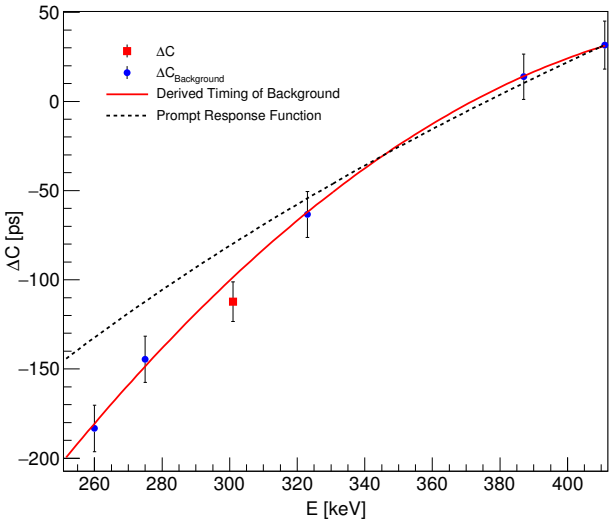

Figure 6.36.: Centroid difference diagram

fitted to the Gammasphere spectrum in figure 6.34b. Table 6.27 shows their integral, and the values calculated for the FATIMA, taking the efficiency of both arrays into account. The integral of the gaussian fit in figure 6.34b has been calculated to be $P = 402.2(207)$, which is in good agreement with the sum of the calculated values, $P_{148} + P_{150} = 439.4(653)$.

Taking into account the value obtained in section 6.5.2 for $\Delta C_{148} = 156(6)\,\text{ps}$ and the calculated relative intensity of both transitions in the FATIMA (summarised in table 6.28), the centroid difference due only to the transitions in ^{150}Ce, $\Delta\ C_{150} = 164(74)\,\text{ps}$. Finally, the application of the formula 3.23 yields a lifetime of $\tau_{6^+} = 42(38)\,\text{ps}$.

	Gammasphere	FATIMA
P_{150}	441.5 ± 21.0	377.9 ± 64.0
P_{148}	71.0 ± 8.5	61.5 ± 13.0

Table 6.27.: Number of counts detected in the Gammasphere and calculated in the FATIMA.

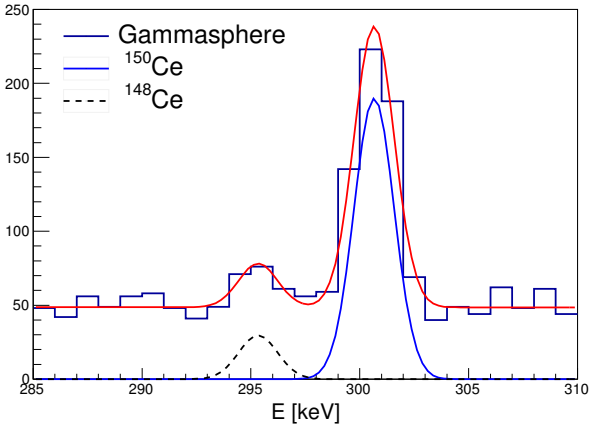

Figure 6.37.: Gammasphere energy spectrum where the transitions $4^+ \rightarrow 2^+$ in ^{148}Ce and $6^+ \rightarrow 4^+$ in ^{150}Ce are visible

P_{148}	ΔC_{148} [ps]	P_{150}	ΔC_{150} [ps]	τ [ps]
61.5(130)	-156(6)	377.9(640)	-164(74)	42(38)

Table 6.28.: Parameters used in the calculation of τ_{6^+}

7 Results and discussion

7.1 Lifetimes

A summary of the lifetimes obtained in this work is presented in table 7.1.

Isotope	State	τ [ps]
^{146}Ce	2^+	270(22)
	4^+	25(20)
^{148}Ce	4^+	51(10)
	6^+	<22
^{150}Ce	4^+	227(38)
	6^+	42(38)

Table 7.1.: Lifetimes obtained in this work

The lifetime obtained for the 2^+ state in ^{146}Ce, of 270(22) ps is in very good agreement with the one published by H. Mach and collaborators, of 273(15) ps [MGM89]. In that case, ^{146}Ce was populated via the β^- decay of ^{146}La, and the lifetime determined by the deconvolution of the timing spectrum between a thin plastic detector triggering with the β particles and a BaF_2 scintillator detecting the $E_{2^+\to 0^+} = 258$ keV γ rays. For the construction of the timing spectrum they used a cleaning energy gate in a HPGe detector. The superior timing resolution of both the BaF_2 scintillator and the plastic detector, compared to that of $LaBr_3$(Ce), allowed the application of the deconvolution method. In addition, the lower background environment eventually led to a better relative uncertainty than the one achieved in this work. However, both the results in this work and by H. Mach and collaborators are noticeably lower than those published by J. C. Jared and collaborators [JNT73], of 0.38(7) ns, and by J. B. Wilhelmy and collaborators [Wil+70], of 0.42 ns. In these two cases, ^{146}Ce was produced in the spontaneous fission of ^{252}Cf and its characteristic X rays and/or γ rays measured in coincidence with pairs of fission fragments. The direct determination of lifetimes was achieved from Doppler-shift considerations.

Unlike in the case of the 2^+ state in ^{146}Ce, only one value has been published for the lifetime of the 4^+ state in ^{150}Ce, of 0.26(10) ns. Furthermore, it is not a direct lifetime measurement, but the estimation A. G. Smith and collaborators made [Smi+99], in order to be able to extract the g-factor from the measured Larmor precession. The calculation of the lifetime is based on the rotational model and the deduced quadrupole moment from the lifetime of the 2^+ state. The value obtained in this work, of 227(38) ps, is in agreement with that estimation, with a better relative uncertainty. The lifetimes presented of the higher-lying states in ^{146}Ce and ^{150}Ce, and of the 4^+ and 6^+ states in ^{148}Ce are obtained for the first time.

7.2 Reduced transition probabilities

The direct determination of nuclear lifetimes makes the model-independent derivation of the reduced transition probabilities between states possible. From equation 2.15 obtained in section 2.2, the following expression for $B(E2)$ can be written:

$$B(E2;\downarrow) = \frac{8.161 \times 10^{17}}{E_\gamma^5 \cdot \tau \cdot (1+\alpha)} \tag{7.1}$$

where $B(E2)$ is expressed in e^2fm^4, E_γ in keV and τ in ps. In table 7.2 the results calculated are listed. The values of the internal conversion coefficient are calculated using the online tool [Brib], which is based on [Kib+08].

Isotope	J^π	E_γ [keV]	τ [ps]	α	B(E2;↓)[e^2fm^4]
^{146}Ce	2^+	258	270(22)	0.079	2451(201)
	4^+	410	25(20)	0.0189	2777(2195)
^{148}Ce	4^+	295	51(10)	0.0514	6841(1386)
^{150}Ce	4^+	209	227(38)	0.1585	7768(1293)
	6^+	301	42(38)	0.0482	7458(6767)

Table 7.2.

These values have been compared to theoretical predictions obtained by means of the Large Scale Shell-Model method (LSSM) and beyond-mean-field calculations, made by H. Naïdja and T. R. Rodríguez, respectively.

The shell-model calculations were performed in the model space spanned by the $2f_{7/2}$, $1h_{9/2}$, $2f_{5/2}$, $3p_{3/2}$, $3p_{1/2}$, $1i_{13/2}$ orbitals for neutrons and the $1g_{7/2}$, $2d_{5/2}$, $2d_{3/2}$, $3s_{1/2}$, $1h_{11/2}$ orbitals for protons above a ^{132}Sn core. The neutron and proton

single-particle energies were taken from experimental values of ^{133}Sn and ^{133}Sb by [Urb+04] and [And+97].

As a starting point a realistic interaction was employed, derived from chiral effective field theory potentials [EM03] denoted N3LO. Its short-range repulsion was renormalised through the low-momentum potential V_{low-k} with a cutoff $\Lambda = 2.2\,\mathrm{fm}^{-1}$. This renormalised interaction was adapted to the model space by many body perturbation theory techniques, including all the Q-box folded diagrams up to the second order [HJKO95]. In the second step the $1f_{7/2}$ neutron-neutron pairing matrix element of the realistic interaction was slightly reduced (by about 120 keV), in order to reproduce isomeric transitions in ^{134,136,138}Sn isotopes following [Sim+14; NNS15]. The resulting effective interaction N3LOP was applied to survey the properties of the cerium isotopes. The diagonalisation was not possible in the cases of ^{148}Ce and ^{150}Ce due to the large dimension of the Hamiltonian matrices, of 37×10^{12} and 5×10^{14}, respectively. Truncation was necessary in the case of ^{146}Ce, keeping up to 4p-4h excitations. The diagonalisation was performed with the ANTOINE shell-model code [Cau+05; CN99]. The calculation of the electric matrix elements was performed with effective charges $e_\pi = 1.6\,e$ and $e_\nu = 0.6\,e$, for protons and neutrons, respectively [Naïxt; Naï+17].

In the case of the beyond-mean-field approach, symmetry conserving configuration mixing (SCCM) calculations were performed, using the effective nucleon-nucleon Gogny D1S interaction. In this framework, the final nuclear states were built as linear combinations of a set of quadrupolar collective states, including axially-symmetric and triaxial shapes. Their coefficients were obtained in a variational manner, following the generator coordinate method (GCM). The many-body states that are mixed in the GCM were found by projecting intrinsic many-body states with a product-like structure (generalised Slater determinants) onto good particle number and angular momentum quantum numbers. These intrinsic (mean-field, product-like) states were obtained by solving variation after particle number projection (PN-VAP) equations [Rodxt; Rod16].

Figure 7.1 shows the comparison between the experimental values and the theoretical calculations for the energies of the 2^+ and 4^+ states. The shell-model calculations are in good agreement in both cases. The beyond-mean-field approach describes the decrease of the excitation energy for increasing masses qualitatively well, although the predicted values are systematically stretched with respect to the experimental data. This is a well-known effect in this kind of calculations and it can be solved if cranking states are included in this framework [Rodxt; Rod16].

Figure 7.2 shows the comparison between the reduced transition probabilities values obtained in this work and their theoretical predictions. The shell model calculation predicts the measured $B(E2; 4^+ \rightarrow 2^+)$ in ^{146}Ce very well, whereas

$B(E2;4^+ \rightarrow 2^+)$ is lower than the experimental one. In the case of the beyond-mean-field calculations, the results are very good in the case of ^{146}Ce; in the case of ^{148}Ce and ^{150}Ce, the calculations are below the measured values. However, the increase of $B(E2;4^+ \rightarrow 2^+)$ for increasing masses in the isotopic chain is properly predicted.

In light of these results, both theoretical models considered seem appropriate to describe the investigated properties of $^{146-150}$Ce. On one hand, beyond-mean-field calculations predict the trends for both the excitation energies and the reduced transition probabilities well, although their values are different than the measured ones. On the other hand, shell-model predictions are accurate, but it is not possible to establish any conclusion on the trends along the isotopic chain.

In conclusion, despite the $B(E2;2^+ \rightarrow 0^+)$ values for ^{148}Ce and ^{150}Ce have not been extracted in this experiment due to the large neutron-induced background in the detectors, it can be stated that:

(i) The isotopes under study show a rotational collective behaviour, as the excitation energies decrease and the ratio between the excitation energies of the 4^+ and the 2^+ states, R_{42}, approaches the characteristic limit of 3.3, for increasing masses;

(ii) The prolate, quadrupolar deformation becomes enhanced for increasing masses. The experimentally obtained trend for the $B(E2;4^+ \rightarrow 2^+)$ values along the isotopic chain supports the trend predicted by SCCM calculations, that foresees that shape evolution. In particular, as it can be seen in figure 7.3, the β_2 deformation parameters evolve from $\beta_2 \approx 0.2$ in ^{146}Ce to $\beta_2 \approx 0.25$ in ^{150}Ce;

(iii) The isotopes studied show a small triaxial deformation, supported by both theoretical calculations presented. The shell-model calculation predicts deformation parameters $\beta_2 = 0.2$ and $\gamma = 14.7^\circ$ for the intrinsic shape of ^{146}Ce, whereas the SCCM calculations show $\gamma > 0$ for all isotopes, especially noticeable in ^{148}Ce and ^{150}Ce (figure 7.3).

7.3 Outlook

As it has been shown, the determination of lifetimes for the isotopes studied in this experiment was successful, thanks to the high sensitivity of the Generalised Centroid Difference Method and the use of a highly efficient detection array, that

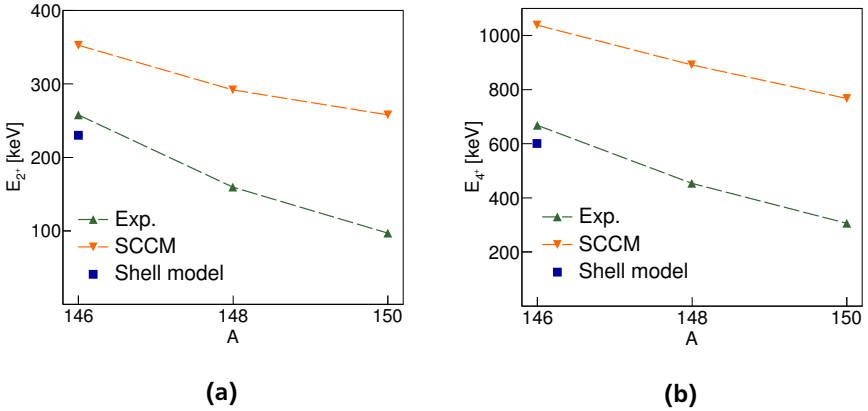

Figure 7.1.: Comparison between the experimental values and theoretical predictions for the excitation energies of the yrast 2^+ state (7.1a) and 4^+ state (7.1b) in the $^{146-150}$Ce isotopes [Naïxt; Rodxt]

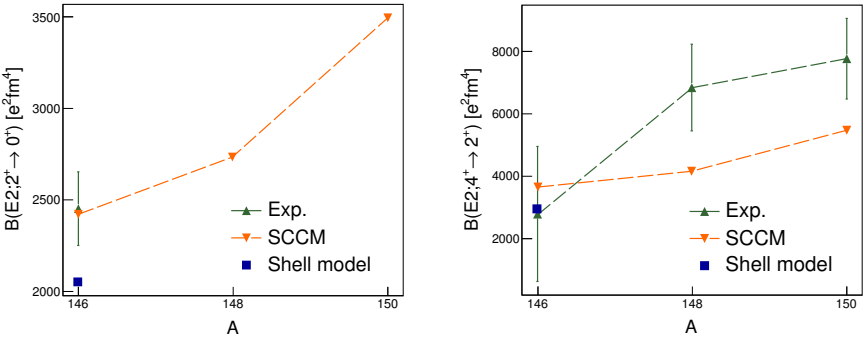

Figure 7.2.: Comparison between the experimental values and theoretical predictions for the reduced $2^+ \rightarrow 0^+$ (7.2a) and $4^+ \rightarrow 2^+$ (7.2b) probabilities in the cerium isotopes studied in this work [Naïxt; Rodxt]

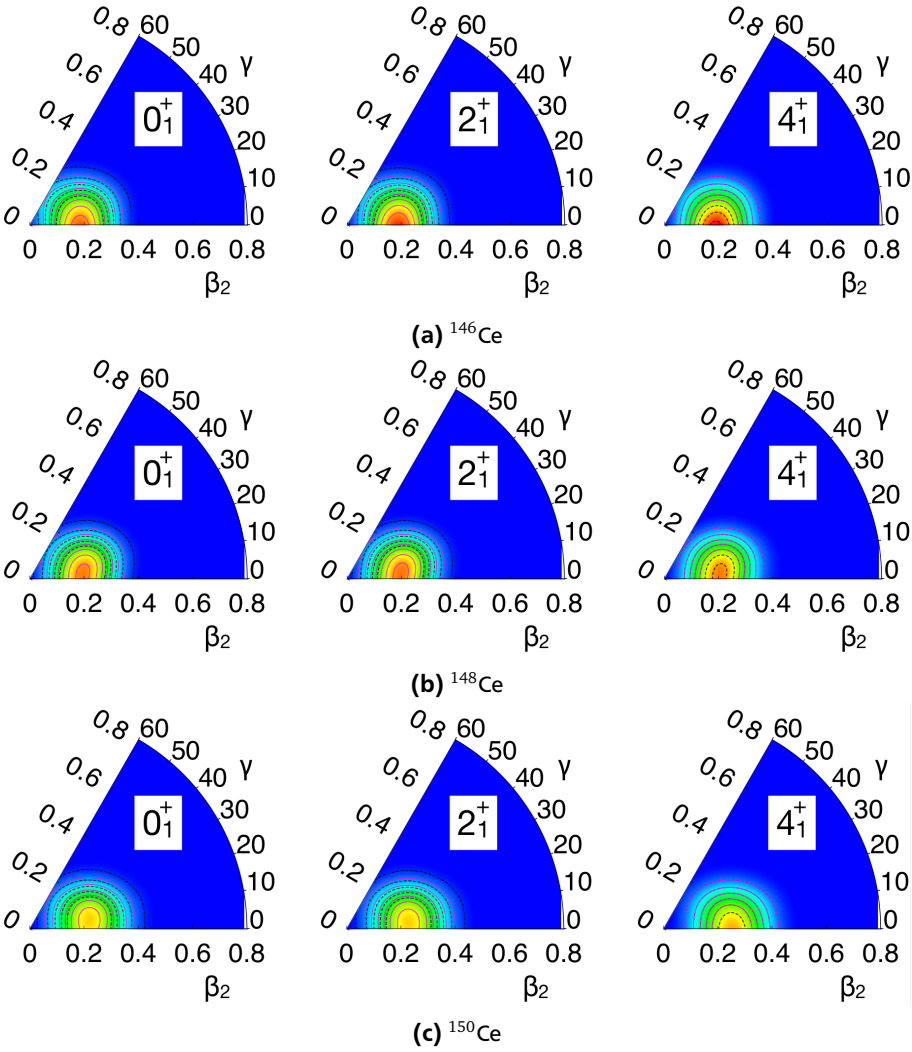

Figure 7.3.: Collective wave functions in the plane (β_2, γ) obtained with the SCCM calculations for the ground state and the first two excited states, including axially-symmetric and triaxial quadrupolar shapes [Rodxt]

combined the good energy resolution of the Gammasphere with the good timing resolution of the FATIMA.

However, it is worth to question the suitability of an event-based data acquisition system that introduces an average dead-time of approximately 1 ms for an experiment with such a high γ-ray multiplicity, not only from the spontaneous fission of ^{252}Cf, but also from the inelastic scattering of fission neutrons on the $LaBr_3$(Ce) detectors, and from the typical background present in the laboratory. Therefore, it is safe to claim that, unless the background conditions are very well known and do not affect the data acquisition, a triggerless event readout is more convenient than the event-based one used in this work. Obviously, the subsequent increase in the amount of data to be written is an effect that must be considered.

The lifetimes of the first excited states in ^{148}Ce and ^{150}Ce, that would provide crucial information on the nuclear deformation, could not be measured in this experiment. A possible way to measure them in a lower background environment than the one present in the case of fission experiments, would be to produce the neutron-rich cerium isotopes via β decay and to use an array of HPGe, $LaBr_3$(Ce) and plastic detectors. This could be done in ISOLDE, at the Decay Station (IDS). It would require the extraction of ^{146}Cs, ^{148}Cs and ^{150}Cs from the ion source, the subsequent production of the different beams, and their implantation in a position close to the detector array. There, the nuclei would decay via the emission of β particles to Ba, La and eventually to Ce. The identification of the cerium isotope would be achieved with the detection of the β particle in the plastic detector, as well as one or more characteristic energies in the HPGe detectors. The $LaBr_3$(Ce) detectors would, therefore, detect the times characteristic of the population and depopulation of the excited state.

At this point, it is worth to recall the aim of the FATIMA, within the DESPEC experiments in the future FAIR. Ideal experimental conditions will be achieved to make a clean measurement of sub-nanosecond lifetimes possible [Fra+15]. In this case, the fragment separator Super-FRS in combination with a high intensity primary beam will allow access to a large variety of neutron-rich nuclei along the r-process path with very high yields. The DESPEC experiment, placed at the end of the Low Energy Branch of the Super-FRS, will consist of an array of detectors that will include AIDA, a stack of highly segmented silicon-based, implantation detectors, FATIMA, and other devices, such as HPGe or neutron detectors.

A Particle discrimination in $LaBr_3$(Ce) and $CeBr_3$ crystals through pulse-shape analysis

A.1 Introduction

The future FAIR will hold the R^3B (**R**eactions with **R**elativistic **R**adioactive **B**eams) experimental setup. It will include CALIFA (**CAL**orimeter for **I**n **F**light detection of γ rays and high energy charged p**A**rticles), an array of scintillators around the target area which will work both as a calorimeter and a spectrometer, and will allow kinematically-complete measurements. One of its requirements, especially for the crystals placed at the most forward angles, is the ability to discriminate between γ rays and light charged particles emitted from the reaction zone [Aum+11; Aum+14] at very high rates.

Commonly, pulse-shape analysis methods used for particle discrimination are applied to scintillators that show two or more decay components, one of which may extend up to several microseconds [Wir+13]. This is a clear inconvenience for experiments that require a fast response of the detectors. In order to overcome this problem, the usage of $LaBr_3$(Ce) and $CeBr_3$ crystals in the CALIFA endcap has been considered [Aum+14], since both of them show a sole, fast decay time [Bria] [Sci] [Lec+06], in addition to a good combination of good energy resolution with high efficiency. In this work, their response to different incoming particle species has been tested. This feature had not been deeply investigated yet, especially in the case of $CeBr_3$. Some attempts had been made for $LaBr_3$(Ce) and $LaCl_3$(Ce) with digital electronics, although the great advantages that fast sampling analog-to-digital converters provide had not been fully exploited, since the majority of them were an adaptation of well-known analogical methods to a digital environment [Cre+09]. In this appendix, the performance of several methods for particle discrimination in $LaBr_3$(Ce) and $CeBr_3$ scintillators will be evaluated.

A.2 Detectors and data acquisition

Two scintillator detectors were used in this study: a $LaBr_3$(Ce) crystal manufactured by Saint Gobain under the commercial name BrilLanCe380 [Sai] and a $CeBr_3$ crystal manufactured by SCIONIX Holland B.V. [Sci]. Both were cylindrically-shaped, with a diameter of 1.5" and a length of of 1.5". They were coupled to Hamamatsu photomultipliers R9779 [Pmt]. The photomultiplier anode signals were read out and sampled using a fast analog-to-digital converter CAEN V1742B [V17a], and stored in a computer for their offline analysis.

A.3 Particle identification technique

Commonly, discrimination between different particles species exploits the dependencies among their physical properties such as charge, mass, etc., that are characteristic of each type of particle. For instance, a well established technique to distinguish charged particles of different mass is the Time-of-Flight method, in which each particle species is characterised by the dependency between velocity and momentum. These variables are experimentally determined by measuring, simultaneously, the particle time of flight across a known distance between two detectors and its energy, $\{t_{ToF}, E\}$ [Kle99]. Other way to distinguish among particles of different charge and mass is through the dependency of the energy loss while traversing matter on kinetic energy. This is experimentally achieved through the usage of the so-called telescope detectors, composed of a thiner detector that measures energy loss, and a thicker detector, that determines the remaining energy. In this case, the pair $\{\Delta E, E\}$ allows the particle discrimination [Kno89].

In the present work, the discrimination is not directly based on the dependencies among physical properties of the particles detected. However, the dependency on energy of a parameter P derived from the detectors pulse shape through a variety of methods is used and, thus, the pair $\{P, E\}$ must be obtained for each particle. Some methods to calculate this parameter, such as the ratio between integrated charge over different time intervals have been widely applied in the past [Wir+13]. However, the usage of novel digital electronics allows for the treatment of the sampled detectors' signals as elements $\boldsymbol{x}$ of a vector space $V = \mathbb{R}^n$, where the dimension n is the number of sampled values of each signal. Assuming that particles of different nature interact with the scintillating material in different ways, leading to differently shaped traces $\boldsymbol{x}$, it is possible to define a function $d(\boldsymbol{x_1}, \boldsymbol{x_2}) : \mathbb{R}^n \to \mathbb{R}$ that makes an unambiguous particle discrimination possible, $\{d(\boldsymbol{x_1}, \boldsymbol{x_2}), E\}$. Furthermore, the knowledge of a model $\boldsymbol{x}$ for each kind of particle allows for the particle identification of all sampled signals. In section A.3.1, the procedure to calculate

the model pulses for the different particle species is explained. In section A.3.2, the discrimination performance of several $d(\boldsymbol{x_1}, \boldsymbol{x_2})$ definitions is evaluated.

A.3.1 Calculation of model traces

Getting the model trace of any kind of particle is an iterative process illustrated in the first two branches of the flux diagram drawn in figure A.1. Each one of its iterations consists of the following steps:

(i) To take the trace $\boldsymbol{x_{in_j}} = \{x^1_{in_j}, x^2_{in_j}, ..., x^n_{in_j}\}$, composed of $n = 1000$ sampled values.

(ii) To calculate its baseline, bs_j, as the average value of its first hundred samples, where no relevant signal is present.

(iii) To calculate its energy, E_j, as the area under the trace, which has been previously baseline restored.

(iv) To compare its energy to a previously defined energy gate. Only traces whose energy lies on a narrow energy interval are used in the calculation, in order to exclude any possible dependency of the pulse shape on energy.

(v) To normalise $\boldsymbol{x_{in_j}}$ to $\boldsymbol{x_{N_j}} = \frac{N_1}{E_j}\boldsymbol{x_{in_j}}$, where N_1 is a normalisation factor.

(vi) To align the trace $\boldsymbol{x_{N_j}}$ in time with respect to a reference trace $\boldsymbol{x_R}$ to obtain $\boldsymbol{x_{A_j}}$. The alignment consists of a horizontal shift of the trace $\boldsymbol{x_{N_j}}$ of magnitude given by the point at which the function $f(\delta) = \sqrt{\sum_{i=0}^{w}(x_j^{w_0+i+\delta} - x_R^{\tau_R+i})^2}$ reaches its minimum value. w_0 is the first sample of $\boldsymbol{x_{N_j}}$ used in the calculation of $f(\delta)$; w is the number of samples used; τ_R is the first sample of the reference trace used.

(vii) To go to the next trace in the data set, $\boldsymbol{x_{in_{j+1}}}$.

In this work, the iterative process has been carried until a total of $K = 100$ traces have been collected. Their average is the model trace, $\overline{\boldsymbol{x}} = \frac{1}{K}\sum_{m=0}^{K}\boldsymbol{x_{A_m}}$. In addition, and for the subsequent analysis, it is convenient to calculate the difference $\boldsymbol{f}$ between the model traces $\overline{\boldsymbol{x}}$ and $\overline{\boldsymbol{y}}$.

Figure A.2 shows a collection of sampled signals from the anode of a photomultiplier coupled to a $LaBr_3$(Ce) detector. No conditions have been imposed on them, leading to a set of traces that span a broad energy range. A set of traces from this data set in a narrow energy interval has been selected, normalised and drawn in figure A.3. Figure A.4 shows the result of the application of the aligning algorithm.

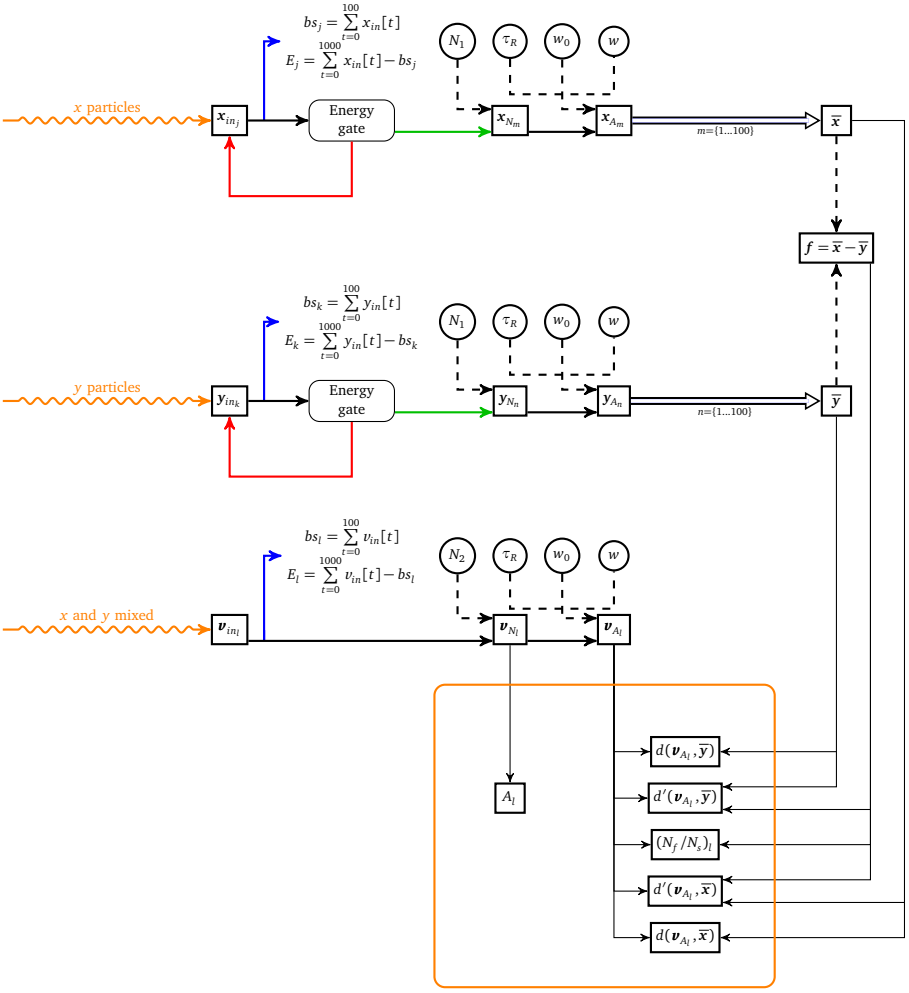

Figure A.1.: Flux diagram showing the steps necessary for the application of the different methods, listed inside the orange frame

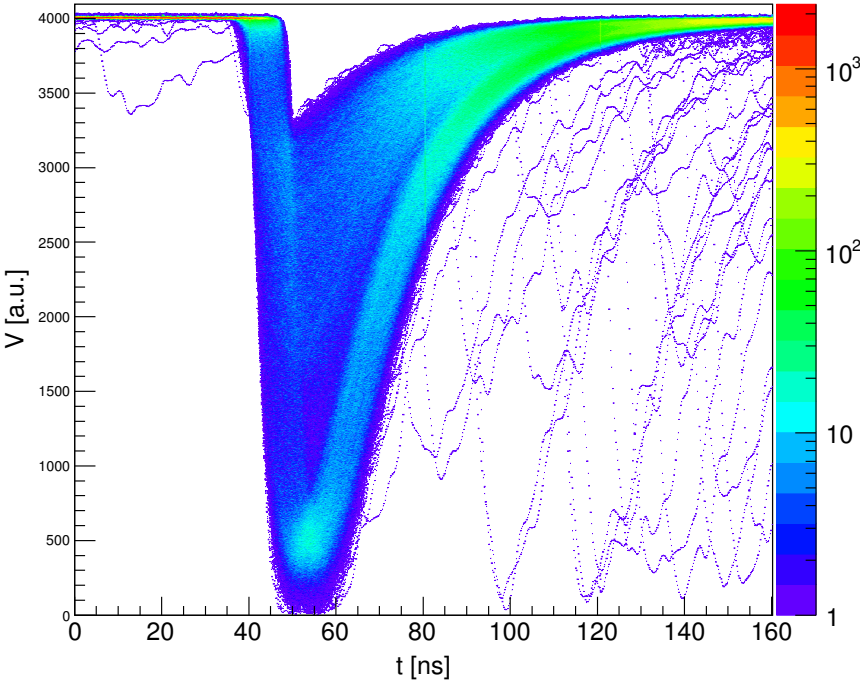

Figure A.2.: Raw traces

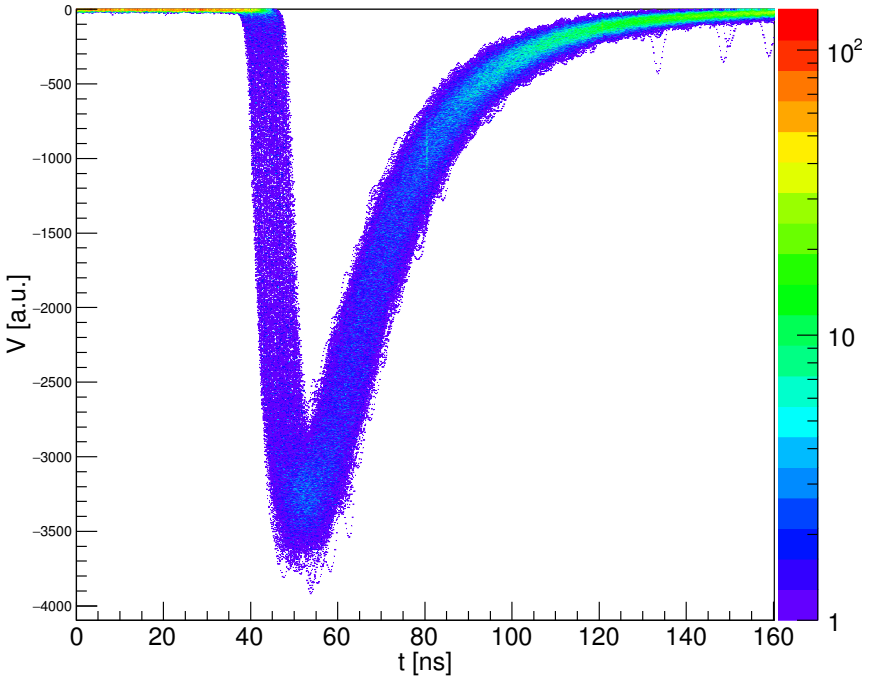

Figure A.3.: Normalised traces

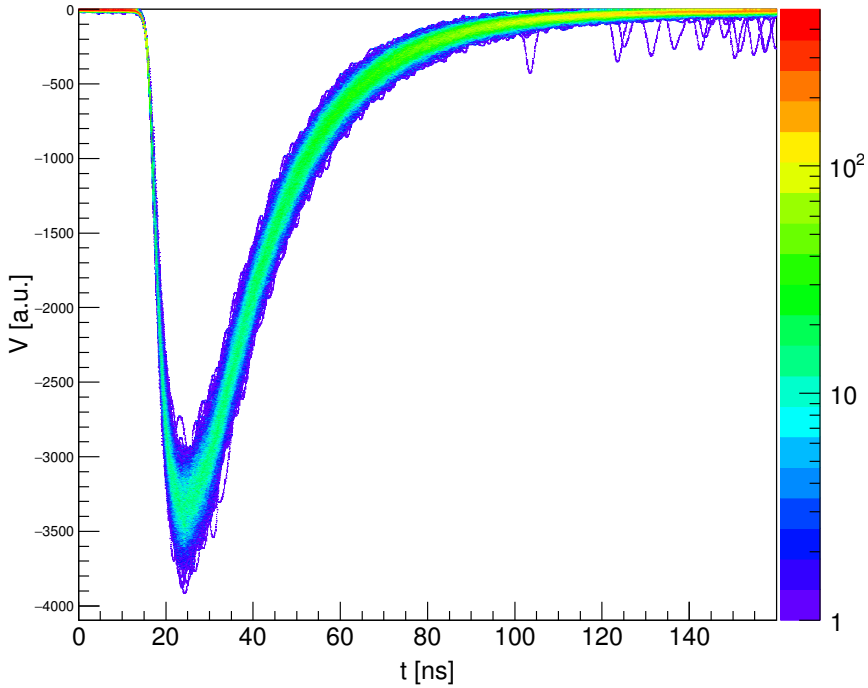

Figure A.4.: Aligned traces

A.3.2 Particle discrimination methods

In this section, the different methods used to calculate the characteristic parameter P, necessary to achieve the particle discrimination are described. As it can be seen in figure A.1, prior to the application of any method, the detectors' signals $\boldsymbol{v}$ need to undergo a preparation procedure very similar to the one explained in section A.3.1, that includes baseline restoration, energy calculation, normalisation (to a normalisation factor N_2, different to the one used for the calculation of the model trace) and time alignment with respect to a reference. The variety of methods and the parameters derived are shown in an orange frame in figure A.1, as well as the elements needed for their calculation.

Normalised trace amplitude

As it can be seen if figure A.1, this is the only method to calculate P that does not require the traces time alignment. In this case, P is the amplitude of the trace after its normalisation:

$$P \equiv A = v^i \ni v^i \text{is the absolute minimum} \tag{A.1}$$

Ratio between charge integrated over different time intervals

The parameter P is calculated as follows:

$$P \equiv \frac{N_f}{N_s} = \frac{\sum_{i=0}^{i_0} v^i}{\sum_{i=i_0}^{n} v^i} \text{ , where } i_0 \ni f(i_0) = 0 \tag{A.2}$$

The time intervals that determine the integration ranges are delimited by the point at which $\boldsymbol{f}$ is zero.

Distance to computed model pulses

The distance between any particle trace $\boldsymbol{v}$ and a model trace $\overline{\boldsymbol{x}}$ is the discrimination parameter, $P \equiv d(\boldsymbol{v}, \overline{\boldsymbol{x}})$, and can be calculated according to a set of expressions that take two standard norms into account [Wir+13], summarised in table A.1. Each of the norms has been used with and without the weighting function $\boldsymbol{f} = \overline{\boldsymbol{x}} - \overline{\boldsymbol{y}}$ intended to enhance the discrimination ability of the method (table A.1).

	Absolute-value norm	Euclidean norm
non-weighted	$\sum_{i=0}^{n} \lvert v^i - \overline{x}^i \rvert$	$\sqrt{\sum_{i=0}^{n} (v^i - \overline{x}^i)^2}$
weighted	$\sum_{i=0}^{n} \lvert f^i \cdot (v^i - \overline{x}^i) \rvert$	$\sqrt{\sum_{i=0}^{n} [f^i \cdot (v^i - \overline{x}^i)]^2}$

Table A.1.: Definitions of $d(\boldsymbol{v}, \overline{\boldsymbol{x}})$ used.

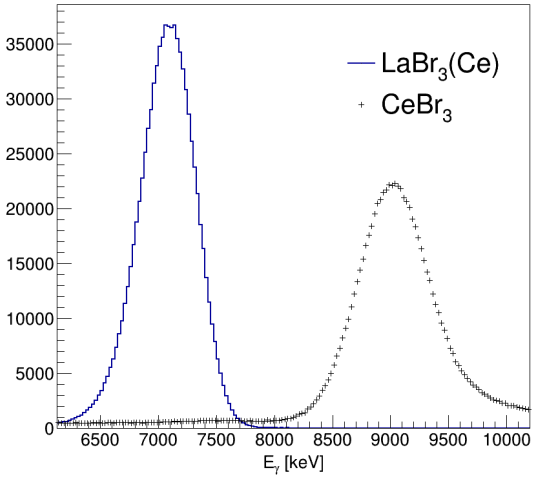

Figure A.5.: Proton energy spectra obtained with both detectors placed at the beam

A.4 Experiment

In this section, the experimental setups used to acquire data sets to calculate the proton, γ-ray and α-particle model traces, and to test the particle discrimination methods will be explained.

The experiment was performed in the Maier-Leibnitz Laboratorium, in Garching, near Munich, and took advantage of its tandem-van de Graaff accelerator, that can provide proton beams with energies up to $E_p = 24$ MeV. In the case of this experiment, the energy of the proton beam was $E_p = 22$ MeV. In the first instance, the $LaBr_3$(Ce) and $CeBr_3$ detectors were consecutively placed at the proton beamline, in order to sample enough proton signals to calculate their model trace, $\overline{\boldsymbol{p}}$.

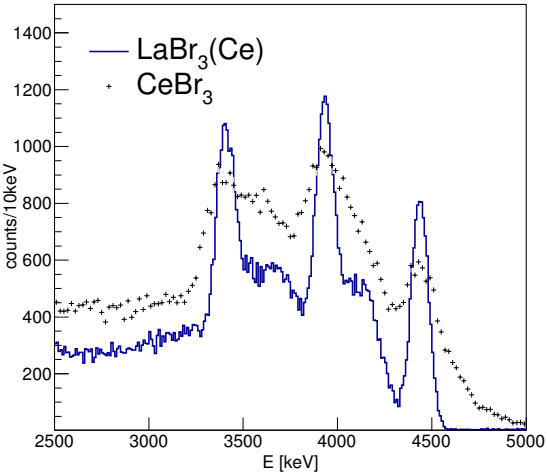

Figure A.6.: γ-ray energy spectra obtained with both detectors

The energy spectra obtained are depicted in figure A.5. Despite both peaks correspond to the beam energy, their positions do not overlap due to two reasons. The first one is the combination of the usage of γ-ray sources to perform the energy calibration and the effect called quenching, i.e., the ratio between light yield induced by γ radiation and by protons varies for different crystals. The second one is a consequence of the different thickness of the scintillators encapsulation, that provokes a higher energy loss before reaching the $LaBr_3(Ce)$ crystal than the $CeBr_3$. A summary of the materials that protons have to pass through can be found in table A.2 [Rhe].

Crystal	Aluminum (μm)	Polymer (μm)
$LaBr_3(Ce)$	980	500
$CeBr_3$	500	500

Table A.2.: Summary of the various materials' thicknesses.

The collection of γ-ray traces necessary to calculate $\overline{\gamma}$ was subject to the production of photons that cause a light yield in the scintillators similar to the one caused by the protons. This was achieved by placing several carbon targets on the beamline

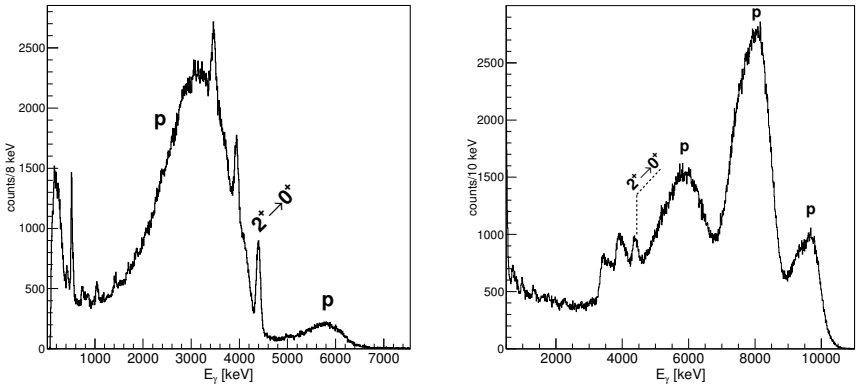

(a) $LaBr_3(Ce)$ **(b)** $CeBr_3$

Figure A.7.: Energy spectra of the mixture of protons and γ rays

in order to stop the protons completely and induce the reaction $^{12}C(p,p')^{12}C$. The inelastic scattering of the protons provokes the emission of γ rays with an energy of 4439 keV from the transition $2^+ \rightarrow 0^+$ in ^{12}C. The spectra obtained in both detectors are depicted in figure A.6, where the full energy peak at 4439 keV is clearly visible, as well as the single- and double-escape peaks. The energy resolution of the $CeBr_3$, with a relative value at $E = 4439$ keV for the full-width-at-half-maximum of $R = 6.4\%$, is much worse than the one achieved by the $LaBr_3(Ce)$, of $R = 2.5\%$. This setup was also used for the extraction of the $\overline{\boldsymbol{\alpha}}$ model trace, since α particles are a contaminant present in both the $LaBr_3(Ce)$ and the $CeBr_3$ crystals.

The last of the experimental setups was built up in order to record a mixture of proton and γ-rays signals lying on the same energy range that allows to test the performance of the particle discrimination methods. For that aim, several carbon targets of different thickness were placed at the beamline in order to induce the same reaction as explained above, and the detectors were placed at a scattering angle of 20°, where they recorded both the scattered protons and the γ-rays with energies of 4439 keV. This can be seen in the spectra depicted in figures A.7a and A.7b. In both cases, peaks from the detection of γ rays and protons are visible. On the energy spectrum measured with the $LaBr_3(Ce)$ detector, two broad peaks from the scattering of protons at the carbon target and at the target holder (a thin aluminum plate) are clearly visible, as well as the peaks already identified in figure A.6 originating from the high-energy γ rays. On the spectrum measured with the

$CeBr_3$ detector, an analogous situation can be described, although in this case an additional proton peak is detected at high energies. It originates from the protons scattered at the exit window of the last element of the beam pipe, whose trajectory towards the detector was not properly blocked.

A.5 Results

A.5.1 p-γ discrimination

$\overline{\gamma}$ and $\overline{p}$ model traces are drawn in figures A.8a and A.8b for $LaBr_3$(Ce) and $CeBr_3$, respectively. As it has already been explained in section A.3.1, each of them is the average of a hundred γ-ray and proton traces, respectively. On the bottom panels, the difference between both models, which will be later used as a weight function, is drawn. These two figures expose the dependency of the pulse shape on the particle species. Additionally, a dependency of pulse shape on the particle energy has been found. Let figures A.8c and A.8d serve as an example. They are the average traces of γ-ray pulses at two different energies: $E = 4439$ keV corresponding to the deexcitation of ^{12}C and $E = 1461$ keV corresponding to the deexcitation of ^{40}Ar, present in the experimental hall as a contaminant.

Figures A.9 and A.10 show the discrimination achieved when using the weighted, Euclidean distance definition as discrimination parameter applied to the data set containing γ rays and protons, detected in $LaBr_3$(Ce) and $CeBr_3$, respectively. Both the dependency on particle and energy species are observed. The discrimination between γ rays and protons (in a red frame) is successfully achieved and the particle identification, possible.

Figures A.11a and A.11b show the separation achieved by different methods at both crystals. It is obtained as a projection onto the discrimination parameter axis, P, of the events within a narrow energy interval with a width of 100 keV, marked in figures A.9 and A.10 with two dashed lines. The values P have been subjected to a linear calibration for the two species to appear around the arbitrary values of P =0 (protons) and $P = 1$ (γ rays). Additionally, in order to evaluate each method separation ability, the sum of two gaussian curves has been fitted to the peaks in figures A.11a and A.11b, and the following figure-of-merit defined:

$$\text{fom} = \left| \frac{\mu_p - \mu_\gamma}{\sigma_p + \sigma_\gamma} \right| \tag{A.3}$$

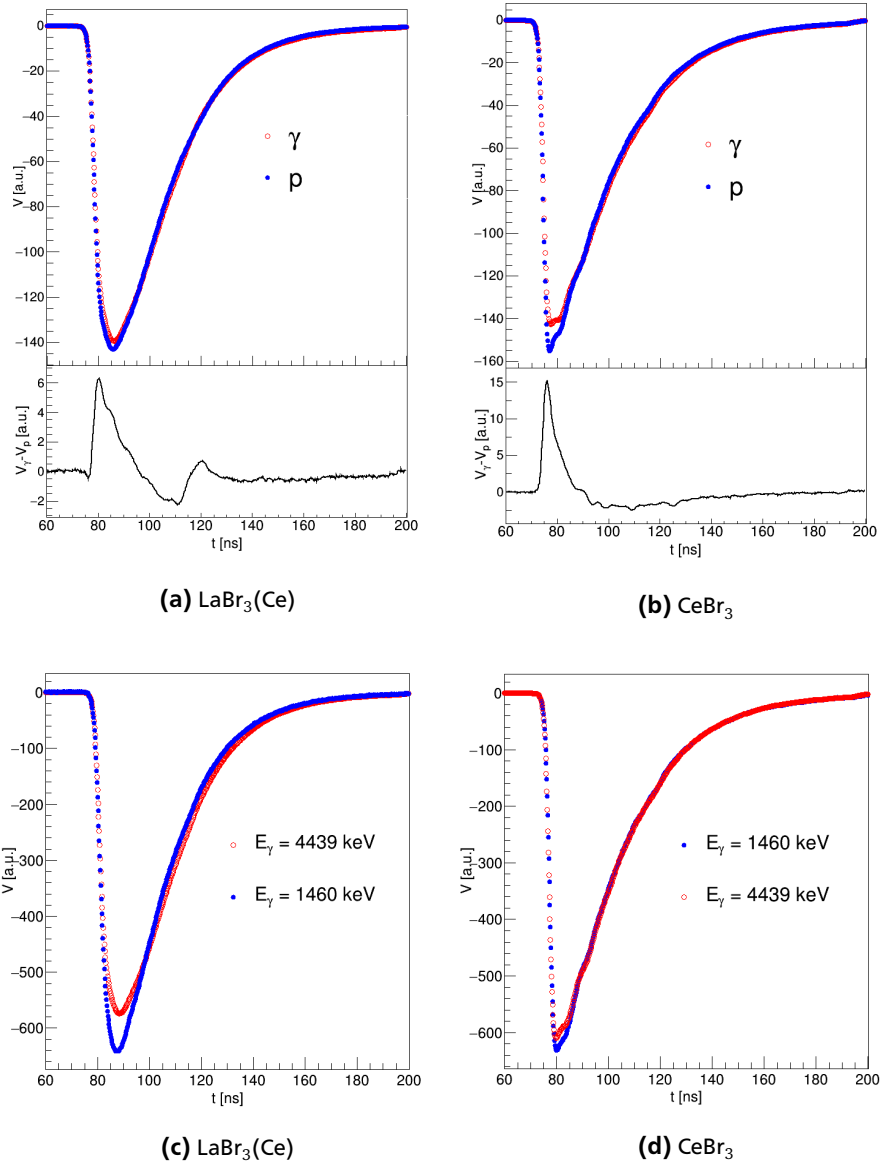

Figure A.8.: Pulse shape dependencies on particle species (A.8a and A.8b) and energy (A.8c and A.8d).

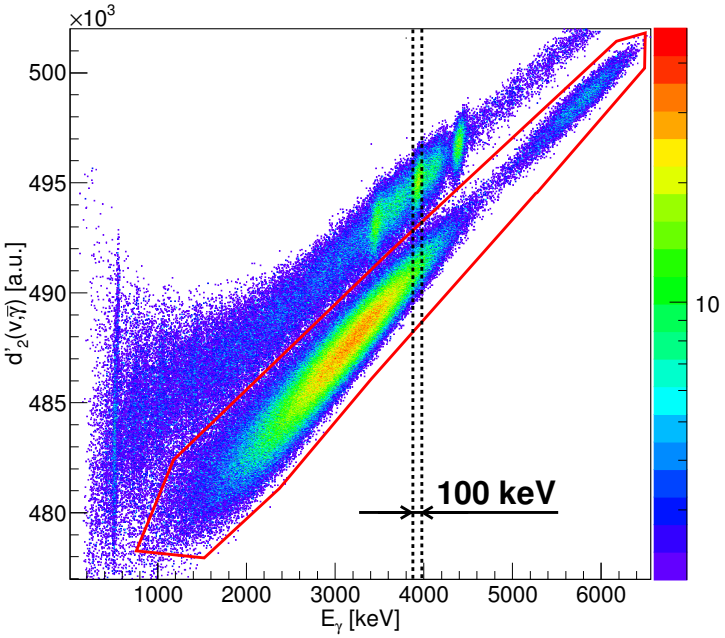

Figure A.9.: Separation between γ rays and protons achieved in $LaBr_3$(Ce)

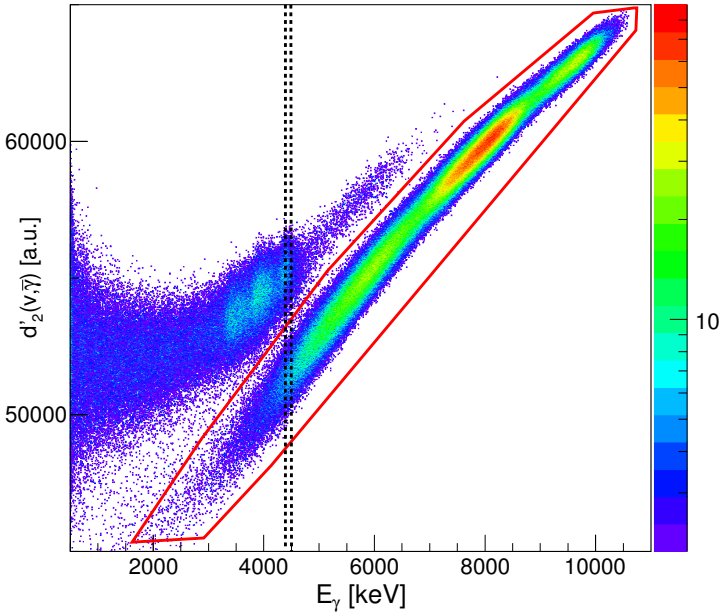

Figure A.10.: Separation between γ rays and protons achieved in $CeBr_3$

Method	$LaBr_3(Ce)$	$CeBr_3$
$d_2'(\boldsymbol{\nu},\overline{\boldsymbol{\gamma}})$	2.74	2.70
$d_2(\boldsymbol{\nu},\overline{\boldsymbol{\gamma}})$	2.25	1.74
A	1.87	2.39
$\frac{N_f}{N_s}$	2.50	2.19

Table A.3.: Summary of the methods figure-of-merit

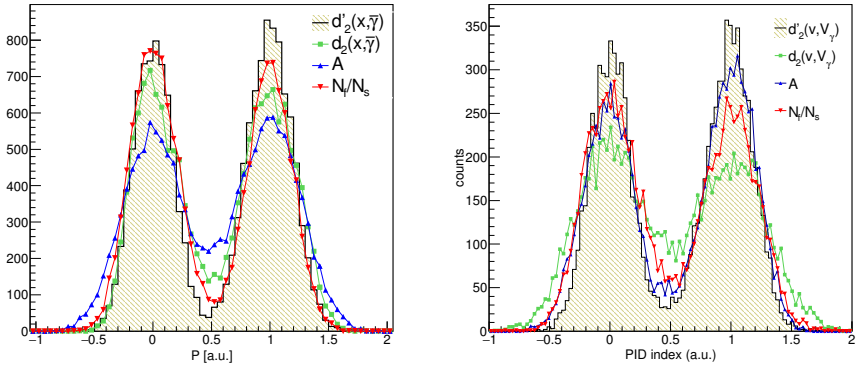

(a) **(b)**

Figure A.11.: Distribution of the discrimination parameter P for a set of events within a narrow energy interval of 100 keV around the single-escape peak

The values obtained are summarised in table A.3, and it can be stated that the best results are obtained for the weighted, Euclidean distance, whereas the amplitude method yields the worst ones.

A.5.2 α-γ discrimination

The presence of internal radioactivity (whose origin has been already discussed in section 4.1.3) in the $LaBr_3(Ce)$ and $CeBr_3$ is unavoidable, and can be therefore used for the calculation of the $\overline{\boldsymbol{\alpha}}$ trace. The selection of the proper traces to compute the average is subject to an initial discrimination of α-particle from γ-ray traces by means of $\{d_2'(\boldsymbol{\nu},\overline{\boldsymbol{\gamma}}), E\}$ in the data set containing high-energy γ-rays. Figures A.12a

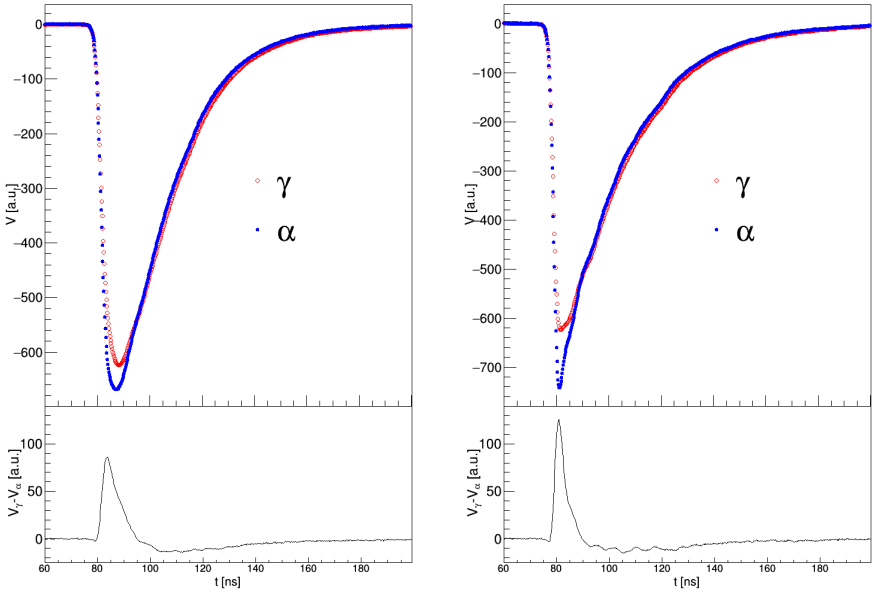

(a) $LaBr_3(Ce)$ **(b)** $CeBr_3$

Figure A.12.: Pulse shape dependency on particle species

and A.12b show the calculated $\overline{\alpha}$ traces in $LaBr_3(Ce)$ and $CeBr_3$, respectively, as well as the $\overline{\gamma}$ and their difference.

The application of the weighted, Euclidean distance to the aforementioned data set yields the discrimination depicted in figures A.13a and A.13b. The presence of α particles is clearly separable from that one from γ rays, and it allows to identify their contribution in the energy spectra drawn in figure A.6. This can be seen in figures A.14a and A.14b. In the spectrum measured with the $LaBr_3(Ce)$ scintillator, not only the α particles contribution can be observed, but also the peaks resulting from the two decay modes of ^{138}La.

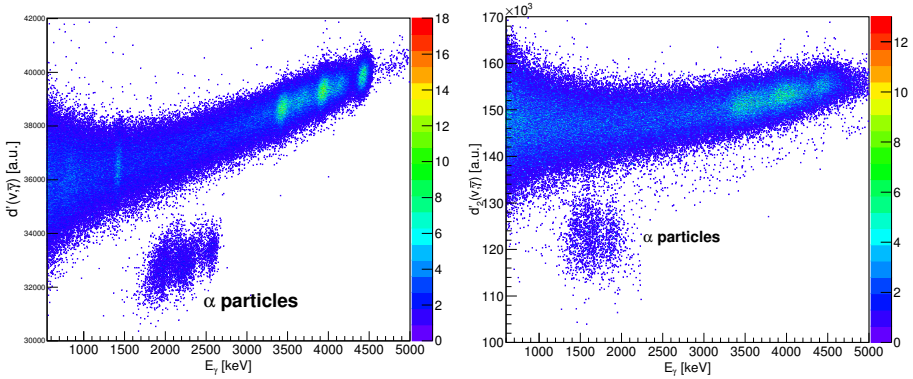

(a) $LaBr_3(Ce)$ **(b)** $CeBr_3$

Figure A.13.: Separation achieved for α and γ

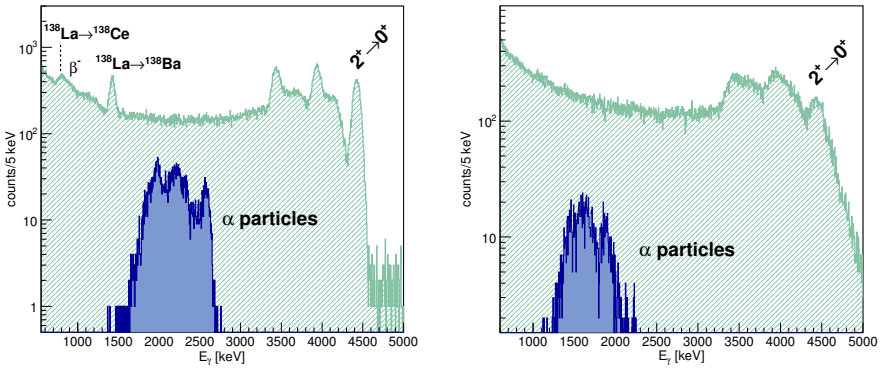

(a) $LaBr_3(Ce)$ **(b)** $CeBr_3$

Figure A.14.: Energy spectra

Acknowledgements

In the first place, I want to express my gratitude to Thorsten Kröll for having given me the opportunity to work on my doctoral thesis in his group. Already from the very first days I could perceive the gestures that would define him as supervisor: confidence, and critical but unconditional support for all my ideas and decisions. His warm reception was constantly endorsed by every person I met in the group, among which I must mention Sabine, Anna, Corinna, Ilja, Han-Bum, Mirko, Christian, Michael and Juan. Special thanks go to Alex and Tania, without whose patience, advice, and constant availability, this work would have never been possible.

The development of this thesis has been marked by my participation in two experiments. Firstly, the one performed at the Maier-Leibnitz Laboratory. I want to acknowledge the kind welcome and help that all members of Roman Gernhäuser's group at the Technical University of Munich gave to their guests from Darmstadt. Secondly, the one performed at Argonne National Laboratory. The stay in a deserted ANL during the Christmas break would have been very tough if Stefan Lalkovski, Shaofei Zhu, Matthias Rudigier, Eugenio Gamba or Alison Bruce wouldn't have been there, not only to share their knowledge, but also to explore every restaurant in the vicinity, to try to spot the famous white deers, or to celebrate New Year's Eve. A close collaboration between Matthias, Eugenio, Tania and me was born fruit of that experiment, which turned out to be crucial for the completion of this work. Few months later Simone Bottoni would join in. I am extremely grateful for our fruitful discussions, as well as for his hospitality during my short visit to the University of Milan. I must not forget the promptness with which Houda Naïdja, from the University of Strasbourg, and Tomás Rodríguez Frutos, from the Autonomous University of Madrid, performed the theoretical calculations that I would compare my results with, as well as their friendliness and patience when solving any of my questions.

I also have to thank the help I got from my friends and from my family, especially from my parents. They have been a very important, strong pillar in my life and, in particular, during my whole educational process that culminates in this thesis. This path would have been very different without their presence. And finally, of course, I want to thank Lourdes. She is the unbeatable life partner who, besides providing strong, firm support in all kind of manners during this period, reminds me day after day of which the truly valuable things in life are.

Bibliography

[Abb+03] M. Abbrescia et al., *Nucl. Instrum. Methods Phys. Res. A* **508**: 79 –82, 2003. DOI: 10.1016/S0168-9002(03)01281-6.

[Ale+14] M. S. Alekhin et al., *J. Lumin.* **145**: 518 –524, 2014. DOI: 10.1016/j.jlumin.2013.08.019.

[And+97] F. Andreozzi et al., *Phys. Rev. C* **56**: R16–R19, 1997. DOI: 10.1103/PhysRevC.56.R16.

[And14] J. T. Anderson, *MyRIAD Module Specification*, Argonne National Laboratory, 2014. URL: http://npg.dl.ac.uk/MIDAS/MIDASWebServices/VME/MyRIAD/ANL-15_07_Myriad_user_manual.pdf.

[And15] J. T. Anderson, *Digital Gammasphere Firmware User's Manual*, 2015. URL: https://wiki.anl.gov/wiki_heliosdaq/images/f/f2/ANL_Firmware_for_LBL_Digitizer_June_2015.pdf.

[Aum+11] T. Aumann et al., *The R^3B CALorimeter for In Flight detection of γ rays and high energy charged pArticles. Technical Report for the Design, Construction and Commissioning of the CALIFA Barrel*, R^3B Collaboration, 2011. URL: https://edms.cern.ch/file/1833500/1/TDR_R3B_CALIFA_BARREL_public.pdf.

[Aum+14] T. Aumann et al., *The R^3B CALorimeter for In Flight detection of γ rays and high energy charged pArticles. Technical Report for the Design, Construction and Commissioning of the CALIFA Endcap*, R^3B Collaboration, 2014. URL: https://edms.cern.ch/file/1833748/1/TDR_R3B_CALIFA_ENDCAP_public.pdf.

[Bay50] Z. Bay, *Phys. Rev.* **77**: 419–419, 1950. DOI: 10.1103/PhysRev.77.419.

[BC56] J. Burde and S. G. Cohen, *Phys. Rev.* **104**: 1093–1098, 1956. DOI: 10.1103/PhysRev.104.1093.

[BD07] G. Bizarri and P. Dorenbos, *Phys. Rev. B* **75**: 184302, 2007. DOI: 10.1103/PhysRevB.75.184302.

[Bel+16] S. J. Bell et al., *J. Phys. Conf. Ser.* **763**: 012010, 2016. URL: http://stacks.iop.org/1742-6596/763/i=1/a=012010.

[Ber07] C. A. Bertulani, *Nuclear Physics in a Nutshell*, Princeton University Press, Princeton, 2007.

[BHK55] Z. Bay, V. P. Henri, and H. Kanner, *Phys. Rev.* **100**: 1197–1208, 1955. DOI: 10.1103/PhysRev.100.1197.

[Bie18] C. Bieniek, "Lifetime measurement of the 4^+ state of ^{148}Ce", *In preparation*, MA thesis, Technische Universität Darmstadt, 2018.

[BMP51] Z. Bay, R. R. Meijer, and G. Papp, *Phys. Rev.* **82**: 754–755, 1951. DOI: 10.1103/PhysRev.82.754.2.

[BN96] P. A. Butler and W. Nazarewicz, *Rev. Mod. Phys.* **68**: 349–421, 1996. DOI: 10.1103/RevModPhys.68.349.

[Bot] S. Bottoni, *private communication*.

[Bria] *BrilLanCe^{TM} Scintillators Performance Summary*, Saint-Gobain Crystals, 2009.

[Brib] *Online Conversion Coefficient Calculator*, consulted in December, 2017. URL: http://bricc.anu.edu.au/.

[Bro+15a] F. Browne et al., "Half-life Measurements of 2_1^+ States in the Vicinity of ^{108}Zr and their Implications for Ground-state Deformations", *Proceedings of the Conference on Advances in Radioactive Isotope Science (ARIS2014)*, 2015. URL: https://journals.jps.jp/doi/abs/10.7566/JPSCP.6.030012.

[Bro+15b] F. Browne et al., *Phys. Lett. B* **750**: 448 –452, 2015. DOI: 10.1016/j.physletb.2015.09.043.

[Can16] Canberra, *Germanium Detectors*, 2016.

[Cau+05] E. Caurier et al., *Rev. Mod. Phys.* **77**: 427–488, 2 2005. DOI: 10.1103/RevModPhys.77.427.

[CN99] E. Caurier and F. Nowacki, *Acta Phys. Pol. B* **30**: 705, 1999. URL: http://www.actaphys.uj.edu.pl/fulltext?series=Reg&vol=30&page=705.

[Cre+09] F. Crespi et al., *Nucl. Instrum. Methods Phys. Res. A* **602**: 520 –524, 2009. DOI: 10.1016/j.nima.2009.01.101.

[Dro+08] W. Drozdowski et al., *IEEE Trans. Nucl. Sci.* **55**: 1391–1396, 2008.

[EM03] D. R. Entem and R. Machleidt, *Phys. Rev. C* **68**: 041001, 4 2003. DOI: 10.1103/PhysRevC.68.041001.

[Fra+15] L. M. Fraile et al., *Technical Report for the Design, Construction and Commissioning of FATIMA, the FAst TIMing Array*, HISPEC-NUSPEC FATIMA Collaboration, 2015. URL: https://edms.cern.ch/file/1865981/1/TDR_HISPEC_DESPEC_FATIMA_public.pdf.

[Fra17] L. M. Fraile, *J. Phys. G* **44**: 094004, 2017. URL: http://stacks.iop.org/0954-3899/44/i=9/a=094004.

[Gam] E. Gamba, *private communication*.

[GM49] M. Göppert-Mayer, *Phys. Rev.* **75**: 1969–1970, 12 1949. DOI: 10.1103/PhysRev.75.1969.

[GN+99] O. Guillot-Noël et al., *Journal of Luminescence* **85**: 21 –35, 1999. DOI: 10.1016/S0022-2313(99)00063-0.

[Gse] *Argonne National Laboratory Physics Division Online Homepage*, consulted in December, 2017. URL: http://www.phy.anl.gov/.

[Gsf] *GAMMASPHERE Online Booklet Homepage*, consulted in December, 2017. URL: http://nucalf.physics.fsu.edu/~riley/gamma/.

[Ham] *Photomultiplier Tubes. Basics and Applications*, consulted in October, 2017. URL: https://www.hamamatsu.com/resources/pdf/etd/PMT_handbook_v3aE.pdf.

[HJKO95] M. Hjorth-Jensen, T. T. Kuo, and E. Osnes, *Physics Reports* **261**: 125 –270, 1995. DOI: 10.1016/0370-1573(95)00012-6.

[HJS49] O. Haxel, J. H. D. Jensen, and H. E. Suess, *Phys. Rev.* **75**: 1766–1766, 1949. DOI: 10.1103/PhysRev.75.1766.2.

[Ili+16] S. Ilieva et al., *Phys. Rev. C* **94**: 034302, 2016. DOI: 10.1103/PhysRevC.94.034302.

[Jan] *JANIS 4*, consulted in April, 2018. URL: https://www.oecd-nea.org/janis/.

[Jay03] E. T. Jaynes, *Probability Theory. The Logic of Science*, Cambridge University Press, New York, 2003.

[JNT73] R. C. Jared, H. Nifenecker, and S. G. Thompson, "Measurement of Prompt Gamma-Ray Lifetimes of Fission Fragments of ^{252}Cf", *Physics and Chemistry of Fission. Proceedings of a Symposium (Rochester)*, vol. II, p. 211, 1973. URL: http://www.nndc.bnl.gov/nsr/nsrlink.jsp?1974JaYY,B.

[Kib+08] T. Kibédi et al., *Nucl. Instrum. Methods Phys. Res. A* **589**: 202 –229, 2008. DOI: 10.1016/j.nima.2008.02.051.

[Kie+15] J. Kiener et al., *Nucl. Instrum. Methods Phys. Res. A* **798**: 152 –161, 2015. DOI: 10.1016/j.nima.2015.07.022.

[Kle99] W. Klempt, *Nucl. Instrum. Methods Phys. Res. A* **433**: 542 –553, 1999. DOI: 10.1016/S0168-9002(99)00323-X.

[Kno89] G. F. Knoll, *Radiation Detection and Measurement*, John Wiley & Sons, New York, 1989.

[Lal] S. Lalkovski, *private communication*.

[Lec+06] P. Lecoq et al., *Inorganic Scintillator for Detector Systems*, Springer Verlag, Berlin, 2006.

[Lee90] I.-Y. Lee, *Nucl. Phys. A* **520**: c641 –c655, 1990. DOI: 10.1016/0375-9474(90)91181-P.

[Leo87] W. R. Leo, *Techniques for Nuclear and Particle Physics Experiments*, Springer Verlag, Berlin, 1987.

[Li08] K. Li, "Study of spontaneous fission of 252Cf: structure of neutron-rich nuclei, gamma-ray angular correlation and g-factor measurements", Dissertation, Vanderbilt University, 2008, URL: https://etd.library.vanderbilt.edu/available/etd-03312008-151010/unrestricted/KeLiThesisFinal.pdf.

[Lic+17] R Lică et al., *J. Phys. G* **44**: 054002, 2017. URL: http://stacks.iop.org/0954-3899/44/i=5/a=054002.

[Loe+01] E. V. D. van Loef et al., *Appl. Phys. Lett.* **79**: 1573–1575, 2001. DOI: 10.1063/1.1385342.

[Mas+13] P. J. R. Mason et al., *Phys. Rev. C* **88**: 044301, 2013. DOI: 10.1103/PhysRevC.88.044301.

[MGM89] H. Mach, R. Gill, and M. Moszyński, *Nucl. Instrum. Methods Phys. Res. A* **280**: 49 –72, 1989. DOI: 10.1016/0168-9002(89)91272-2.

[MM89] M. Moszyński and H. Mach, *Nucl. Instrum. Methods Phys. Res. A* **277**: 407 –417, 1989. DOI: 10.1016/0168-9002(89)90770-5.

[Naï+17] H. Naïdja et al., *Phys. Rev. C* **95**: 064303, 2017. DOI: 10.1103/PhysRevC.95.064303.

[Naïxt] H. Naïdja, *private communication*.

[Nil10] J. Nilsson, "Using the LaBr:Ce scintillation detector for mobile γ-spectrometry", MA thesis, University of Lund, 2010.

[Nil55] S. G. Nilsson, *Mat. Fys. Medd. Dan. Vid. Selsk.* **29**, 1955.

[Nnd] *National Nuclear Data Center*, consulted in August, 2018. URL: http://www.nndc.bnl.gov.

[NNS15] H Naïdja, F Nowacki, and K Sieja, *J. Phys. Conf. Ser.* **580**: 012030, 2015. URL: http://stacks.iop.org/1742-6596/580/i=1/a=012030.

[NSS79] P. J. Nolan and J. F. Sharpey-Schafer, *Rep. Prog. Phys.* **42**: 1, 1979.

[NT92] W. Nazarewicz and S. L. Tabor, *Phys. Rev. C* **45**: 2226–2237, 1992. DOI: 10.1103/PhysRevC.45.2226.

[Pau85] T. J. Paulus, *IEEE Trans. Nucl. Sci.* **32**: 1242–1249, 1985. DOI: 10.1109/TNS.1985.4337024.

[Paz17] V. Paziy, "Ultra fast timing study of exotic nuclei around ^{78}Ni: the β decay chain of ^{81}Zn", Dissertation, Universidad Complutense de Madrid, 2017, URL: https://eprints.ucm.es/41969/1/T38591.pdf.

[PG97] D. N. Poenaru and W. Greiner, *Experimental Techniques in Nuclear Physics*, de Gruyter, Berlin, 1997.

[Pmt] *Photomultiplier tube R9779 Data Sheet*, consulted in October, 2017.

[Qua+13] F. Quarati et al., *Nucl. Instrum. Methods Phys. Res. A* **729**: 596 –604, 2013. DOI: 10.1016/j.nima.2013.08.005.

[Rad] *RadWare*, consulted in August, 2018. URL: http://radware.phy.ornl.gov/main.html.

[Rhe] H.-B. Rhee, *private communication*.

[Rod16] T. R. Rodríguez, *Eur. Phys. J. A* **52**: 190, 2016. DOI: 10.1140/epja/i2016-16190-2.

[Rodxt] T. R. Rodríguez, *private communication*.

[RS80] P. Ring and P. Schuck, *The Nuclear Many-Body Problem*, Springer Verlag, New York, 1980.

[Rud] M. Rudigier, *private communication*.

[Rég+10] J.-M. Régis et al., *Nucl. Instrum. Methods Phys. Res. A* **622**: 83 –92, 2010. DOI: 10.1016/j.nima.2010.07.047.

[Rég+13] J.-M. Régis et al., *Nucl. Instrum. Methods Phys. Res. A* **726**: 191 –202, 2013. DOI: 10.1016/j.nima.2013.05.126.

[Rég+14] J.-M. Régis et al., *Phys. Rev. C* **90**: 067301, 2014. DOI: 10.1103/PhysRevC.90.067301.

[Rég+15] J.-M. Régis et al., *EPJ Web of Conferences* **93**: 01013, 2015. DOI: 10.1051/epjconf/20159301013.

[Rég11] J.-M. Régis, "Fast Timing with $LaBr_3$(Ce) Scintillators and the Mirror Symmetric Centroid Difference Method", Dissertation, Universität zu Köln, 2011, URL: https://kups.ub.uni-koeln.de/4290/1/jm-phd.pdf.

[Sai] *BrilLanCe380 Material Data Sheet*, consulted in August, 2018. URL: https://www.crystals.saint-gobain.com/sites/imdf.crystals.com/files/documents/brillance380-material-data-sheet_69765.pdf.

[Sci] *SCIONIX Holland B.V. Homepage*, consulted in August, 2018. URL: http://scionix.nl.

[Sim+14] G. S. Simpson et al., *Phys. Rev. Lett.* **113**: 132502, 2014. DOI: 10.1103/PhysRevLett.113.132502.

[Smi+99] A. Smith et al., *Phys. Lett. B* **453**: 206 –210, 1999. URL: http://www.sciencedirect.com/science/article/pii/S0370269399003329.

[SS17] N. Saed-Samii, *SOCOv2 users manual*, Universität zu Köln, 2017.

[TA+97] G. M. Ter-Akopian et al., *Phys. Rev. C* **55**: 1146–1161, 1997. DOI: 10.1103/PhysRevC.55.1146.

[Urb+04] W. Urban et al., *Eur. Phys. J. A* **22**: 241–252, 2004. DOI: 10.1140/epja/i2004-10037-5.

[V12] *V1290 Technical Information Manual*, CAEN SpA, 2010.

[V14] *V1495 Technical Information Manual*, CAEN SpA, 2015.

[V17a] *V1742/VX1742 User Manual UM4279*, CAEN SpA, 2017.

[V17b] *V1751/VX1751 User Manual UM3350*, CAEN SpA, 2017.

[Wal04] J. D. Walecka, *Theoretical Nuclear and Subnuclear Physics*, Imperial College Press, London, 2004.

[Wil+70] J. B. Wilhelmy et al., *Phys. Rev. Lett.* **25**: 1122–1125, 1970. DOI: 10.1103/PhysRevLett.25.1122.

[Wir+13] R. Wirth et al., *Nucl. Instrum. Methods Phys. Res. A* **717**: 77 –82, 2013. DOI: 10.1016/j.nima.2013.04.006.

[WS54] R. D. Woods and D. S. Saxon, *Phys. Rev.* **95**: 577–578, 2 1954. DOI: 10.1103/PhysRev.95.577.

[Zhu] S. Zhu, *private communication*.